Dissertation

Development and Characterization of MADPET4: A High Resolution Small Animal Positron Emission Tomography Insert for a 7 T Magnetic Resonance Imaging Scanner

Negar Omidvari

Fakultät für Physik
Technische Universität München

Fakultät für Physik
Technische Universität München

Development and Characterization of MADPET4: A High Resolution Small Animal Positron Emission Tomography Insert for a 7 T Magnetic Resonance Imaging Scanner

Negar Omidvari

Vollständiger Abdruck der von der Fakultät für Physik der Technischen Universität München zur Erlangung des akademischen Grades eines

Doktors der Naturwissenschaften (Dr. rer. nat.)

genehmigten Dissertation.

Vorsitzender:
Prof. Dr. Norbert Kaiser

Prüfende der Dissertation:
1. Prof. Dr. Stephan Paul
2. Prof. Dr. Sibylle Ziegler

Die Dissertation wurde am 28.03.2018 bei der Technischen Universität München eingereicht und durch die Fakultät für Physik am 06.09.2018 angenommen.

Negar Omidvari
ORCID: 0000-0002-7589-4745

To my parents and my sister

Abstract

Positron emission tomography (PET) is an established metabolic imaging technique in nuclear medicine, which can produce 3D images of specific biological processes in the body with a high sensitivity. This capability of PET, in addition to the excellent soft-tissue contrast offered by high-resolution magnetic resonance imaging (MRI) scanners, and the broad diversity of MRI acquisition techniques make PET/MRI a powerful hybrid-imaging tool. The main challenge in developing a PET insert for MRI is to minimize the deterioration of image quality of both modalities, particularly when simultaneous demanding acquisitions are performed, given the significant limitations in material choice and component size. The geometrical design of the system in addition to the characteristics of the individual PET detector modules, the read-out electronics, the data processing, and the image reconstruction algorithm contribute to the overall performance of the PET insert.

MADPET4 (Munich Avalanche Diode PET 4) is a small animal PET insert for a 7 T MRI scanner, which was developed and characterized in this project. The geometrical design of the insert is based on two offset layers of scintillation crystals, which are individually read out by silicon photomultipliers (SiPMs). Although SiPMs have already proven to be promising photo-detectors for PET, their performance is highly influenced by their micro-cell structure, production technology, and the physical properties of the crystal coupled to them. Therefore, as the first step in this project, five types of 1.2×1.2 mm^2 SiPMs were characterized with five types of $1.5 \times 1.5 \times 6$ mm^3 scintillation crystals, including two Ce:LYSO, two Ce:GAGG, and one Pr:LuAG. The SiPMs had micro-cell sizes of 25 μm, 50 μm (two models), 75 μm, and 100 μm. The 75 μm and 100 μm SiPMs and one of the 50 μm models were produced with optical trenches between the micro-cells. The 50 μm SiPMs coupled to Ce:LYSO crystals showed the best overall performance as PET detectors. The model with optical trenches showed the best timing performance, achieving 242 ps coincidence time resolution (CTR). The model with no optical trenches had higher photon detection efficiency, but also

higher optical crosstalk probability. Therefore, it showed a better energy resolution performance with slight degradation in timing, achieving a CTR of 308 ps.

The individual readout scheme of the two offset layers of crystals used in MADPET4 provided high resolution and high count rate capability. Furthermore, the novel detector arrangement used in the scanner, in which all crystals face the center of field of view transaxially, offered high number of scanner symmetries that were exploited in the image reconstruction. The PET insert was developed using the PETsys Electronics detector readout system and its performance was evaluated and compared to other preclinical PET scanners using the NEMA NU 4 measurements and a mouse-size hot-rod resolution phantom. Use of dual-layer crystals resulted in a uniform transaxial resolution up to 15 mm radial offset from the axial center and the 1.2 mm rods were fully recovered in the hot-rod phantom using an iterative image reconstruction algorithm. The one-to-one coupling of the detectors resulted in excellent recovery coefficients for the hot rods of the NEMA image quality phantom, obtaining 82% recovery coefficient for the 2 mm rod. Two *in vivo* simultaneous PET/MRI scans were performed with the insert on mouse heart and brain, which demonstrated the image quality capability of the insert in real imaging scenarios.

Finally, MR-compatibility of the PET insert was assessed by studying the interferences between the PET and the MRI system, with three radio-frequency (RF) coil configurations. Using individually read-out high-gain SiPMs allowed for transferring the SiPM charge to outside the MRI scanner with coaxial cables and reduced some of the interferences. The effects of PET on the static magnetic field, flip angle distribution, RF noise, and image quality of various MRI sequences were investigated. The effects of fast-switching gradient fields and RF pulses on PET count rate were studied, while the PET insert and the readout electronics were not shielded. Operating the insert inside a ^{1}H volume coil, used for RF transmission and reception, limited the MRI to T1-weighted imaging, due to coil detuning and RF attenuation, and resulted in significant PET count loss. Using a surface receive coil allowed all tested MR sequences to be used with the insert, with 45–59% signal-to-noise ratio (SNR) degradation, compared to without PET. With a ^{1}H/^{13}C volume coil inside the insert and shielded by a copper tube, the SNR degradation was limited to 23–30% with all tested sequences, with no discernible distortions. Use of truncated sinc shaped RF excitation pulses and gradient field switching had negligible effects on PET count rate in this configuration.

Zusammenfassung

Positronen-Emissions-Tomografie (PET) ist ein etabliertes metabolisches Bildgebungsverfahren der Nuklearmedizin, mit dem 3D-Bilder spezifischer biologischer Prozesse im Körper mit hoher Sensitivität erzeugt werden können. Diese Eigenschaften der PET, zusammen mit dem exzellenten Weichgewebe-Kontrast von hochauflösender Kernspintomografie (MRT) und der Vielfalt an MRT-Aufnahmetechniken, machen aus PET/MRT ein leistungsstarkes Instrument für Hybrid-Bildgebung. Die Hauptherausforderung der Entwicklung eines PET-Inserts für MRT liegt darin, die gegenseitigen negativen Einwirkungen beider Modalitäten auf die Bildqualität - insbesondere bei anspruchsvollen Messungen - zu verringern. Diese Problematik wird verschärft durch die erheblichen Begrenzung bezüglich Materialauswahl und Größe der Bauteile. Die resultierende Leistung des PET-Inserts wird durch die Systemgeometrie, die Eigenschaften der individuellen PET-Detektormodule, die Ausleseelektronik, die Datenverarbeitung und den Bildrekonstruktionsalgorithmus bestimmt.

MADPET4 (Munich Avalanche Diode PET 4) ist ein Kleintier PET-Insert für einen 7T MRT Scanner, das in diesem Projekt entworfen und charakterisiert wurde. Die Systemgeometrie beruht auf zwei versetzten Schichten von Szintillationskristallen, die einzeln mit Silicon-Photomultipliers (SiPMs) ausgelesen werden. Obwohl SiPMs als vielversprechende Photodetektoren für PET etabliert sind, ist deren Leistungsfähigkeit stark von der Mikrozell-Struktur, der Herstellungstechnologie und den physischen Eigenschaften des gekoppelten Kristalls beeinflusst. Demzufolge war der erste Schritt dieses Projekts die Charakterisierung von fünf unterschiedlichen 1.2×1.2 mm^2 SiPMs zusammen mit fünf unterschiedlichen $1.5 \times 1.5 \times 6$ mm^3 Szintillationskristallen: zwei Ce:LYSO, zwei Ce:GAGG und einen Pr:LuAG. Die Mikrozellen der SiPMs waren 25 μm, 50 μm (zwei Modelle), 75 μm, and 100 μm groß. Die 75 μm, 100 μm und einer der 50 μm SiPMs wurden mit optischen Gräben zwischen den Mikrozellen hergestellt. Die 50 μm SiPMs mit dem Ce:LYSO Kristall erzielten die beste Gesamtleistung als PET-Detektoren. Das Modell mit optischen Gräben zeigte mit 242 ps Koinzidenz-

Zeitauflösung (CTR) die beste Timing-Leistung. Das Modell ohne Gräben wies eine höhere Effizienz bei der Detektion der Photonen auf, aber auch eine höhere Wahrscheinlichkeit für optischen Crosstalk. Somit erreichte dieses Modell eine bessere Energieauflösung und ein leicht verschlechtertes Timing, mit einer CTR von 308 ps.

Das individuelle Ausleseschema der zwei versetzten Kristallschichten von MADPET4 ermöglichte sowohl eine hohe Auflösung als auch die Fähigkeit, eine hohe Zählrate zu erreichen. Außerdem erlaubte die neuartige Ausrichtung der Detektoren des Scanners, mit allen Kristallen zur Mitte des transaxialen Gesichtsfeldes orientiert, die Ausnutzung einer größeren Anzahl an Symmetrien in der Bildrekonstruktion. Das PET-Insert wurde mit dem Auslesesystem für Photodetektoren von PETsys Electronics entwickelt, dessen Leistung mit anderen präklinischen PET-Scannern anhand von NEMA NU 4-Messungen und einem Maus-großen, Hot-Rod-Auflösungsphantom evaluiert und verglichen wurde. Die Verwendung von zwei Kristallschichten ergab eine gleichmäßige transaxiale Auflösung bis 15 mm radialen Versatzes vom axialen Zentrum, und dank der Verwendung eines iterativen Bildrekonstruktionsalgorithmus wurde der 1.2 mm Stab des Hot-Rod-Phantomes vollkommen wiederhergestellt. Die eins-zu-eins Kopplung der Detektoren führte zu exzellenten Wiederherstellungskoeffizienten der Hot-Rods im NEMA Bildqualitätsphantom, mit 82% Wiederherstellungskoeffizient für den 2 mm Stab. Es wurden zwei *in vivo* simultane PET/MRT Messungen mit dem entwickelten Insert an Mausherzen und -gehirnen durchgeführt, um die Bildqualität des Systems in einem realen Bildgebungsszenario zu beweisen.

Die MR-Kompatibilität des PET-Inserts wurde durch die Analyse der Störungen zwischen den PET- und MR-Systemen mit drei Hochfrequenz (HF) Einstellungen der Spulen bewertet. Die Anwendung individuell ausgelesener, hochverstärkender SiPMs erlaubte zur Verringerung der Störungen, den Ladungstransfer mittels Koaxialkabeln außerhalb des MRT Scanners. Die Einwirkung des PET-Inserts auf das statische Magnetfeld, die MRT-Flip-Winkel Verteilung, das HF-Rauschen und die Bildqualität mehrerer MRT Sequenzen wurden untersucht. Der Einfluss von schnell-schaltenden Gradientenfeldern und HF-Impulsen auf die PET-Zählrate wurde gemessen, da weder das PET-Insert noch die Ausleseelektronik abgeschirmt sind. Wurde das Insert innerhalb einer ^{1}H Volumenspule betrieben, die für HF Übertragung und Empfang benutzt wird, ergab sich ein erheblicher Verlust in der PET-Zählrate und die MRT-Messung musste aufgrund von Verstimmung der Spule und HF-Dämpfung auf T1-gewichtete Bildgebung eingeschränkt werden. Die Anwendung einer Oberflächen-

Empfangsspule ermöglichte den Einsatz aller MR-Sequenzen mit dem PET-Insert, mit einem um 45–59% verschlechtereten Signal-Rausch-Verhältnis (SNR) verglichen mit dem Szenario ohne PET-Insert. Mit einer $^{1}H/^{13}C$ Volumenspule innerhalb des Inserts und einer Kupfer-Abschirmung konnte die SNR-Verschlechterung für alle studierten MR-Sequenzen auf 23–30% ohne erkennbare Verzerrungen eingegrenzt werden. In dieser Konfiguration zeigte die Verwendung von verkürzten sinusförmigen HF-Anregungspulsen und Gradientenfeldwechseln vernachlässigbare Auswirkungen auf die PET-Zählrate.

Acknowledgments

First and foremost, I am deeply grateful to my thesis supervisor, Prof. Sibylle Ziegler, for her mentorship, continuous guidance, and everlasting inspiration through this project. I highly value the time and effort you spent for regularly having our weekly meetings, specially during the time you had moved to LMU. I am thankful for all the detailed constructive feedbacks from you on all the papers and abstracts, specially when they were last minute. Thank you for always motivating me, trusting me and giving me freedom in exploring my ideas in different directions. I learned so much from you during this time and it was a true pleasure to work with you.

I am very thankful to my thesis advisor, Prof. Stephan Paul, at Physics Department E18, for his interest in this project, his support, and all the insightful technical discussions. Thank you for your positive attitude and providing several opportunities for me to collaborate with and learn from different people working at the Physics Department.

I would also like to thank Prof. Volkmar Schulz, for introducing me into this field in the first place. My internship and master thesis work at Philips Research group in Aachen, under your supervision made me certain about continuing my work as a researcher. Thank you for always supporting me and keeping interest in my work through my doctoral thesis. I always enjoyed discussing my work with you and was amazed how often these discussions led to creative ideas.

The work presented in this thesis was supported by an advanced European Research Council (ERC) grant from Prof. Markus Schwaiger, through the European Commission Seventh Framework Programme (FP7), project number 294582: Multimodal Molecular Imaging (MUMI). Working in this project under direction of Prof. Schwaiger was a true honor for me to learn from his broad scientific vision, professional expertise, and prominent leadership. I received outstanding encouragement from him during this project and I thank him for all the professional advices and opportunities he provided for my future carrier.

I gratefully acknowledge the work of several people working at Nuclear Medicine Department of Klinikum rechts der Isar, who assisted me in different ways. My special thanks go to Marie Bieth and Ian Somlai-Schweiger, for going beyond being officemates and colleagues and extending their help and support through true friendships. I would also like to thank Ian for his technical assistance during this project and his help with the German translation of the thesis abstract. Thank you Ian for offering help in the mechanical parts of the project, always with a smile on your face. I am very thankful to Geoffrey Topping, for spending long hours with me in the 7 T MRI lab and I acknowledge his significant contribution to the MR-compatibility study of the PET insert. Thank you Geoff for being so flexible and patient, especially when we needed to repeat the measurements. Thank you for explaining me the details of all the MRI measurements and being so precise in your work.

I am thankful to Ravi Sharma for sharing the results of his master thesis work and for his contribution to the detector characterization study. Furthermore, I would like to thank Borjana Bogdanovic, Karl Kunze, Alexandre Savio, Ane Etxebeste, Vito Gagliardi, Daniel Bonifacio, Giaime Rancan, Franz Schilling, and Jorge Cabello for the interesting scientific discussions and our good times together, particularly during the lunch breaks. Additional thanks to Jorge, for introducing me to PET image reconstruction and to Karl, for offering help whenever I needed assistance with German proofreading and official submission processes.

I would like to thank the radiation protection team, Jakob Allmann, Anne Thieme, and Simone Keber, who assisted me several times in finding the appropriate radioactive solid sources for my measurements. Many thanks also go to Michael Herz, working at the cyclotron site, who always provided the ^{18}F for my measurements, even when it was a short notice. I would like to thank Markus Mittelhäuser for animal handling performed for the PET performance evaluation of MADPET4. I would like to thank Rupert Trager for several occasions that I needed immediate assistance regarding hardware or software issues in one of my computers, and especially in one occasion that he recovered data on a problematic hard disk. I would also like to particularly thank my good friends, Elham Karimi and Zohreh Varasteh, whom I met at Klinikum rechts der Isar, for all the amazing time we spent together.

I would like to thank Florian Schneider, who worked on this project before me, for his guidance during my first year here and his support during the time he had moved to

KETEK. This was especially helpful, when he provided the opportunity for me to test their evaluation kit from PETsys Electronics at KETEK with our detectors. Many more thanks go to Thomas Ganka for agreeing to several rounds of measurements for the detector characterization study and guiding me through different measurement setups at KETEK. It was a truly nice experience to work with you and learn from you. I would also like to thank Dr. Florian Wiest from KETEK for providing the SiPMs and Prof. Kei Kamada from C&A Corporation for providing the crystals and their physical properties for the detector characterization study. Furthermore, I would like to thank Ricardo Bugalho from PETsys Electronics for his prompt responses, valuable support, and fruitful discussions. Many thanks also go to Simon Quittek and Marco Irkens from RAPID Biomedical GmbH for their support and technical assistance regarding the measurements performed with the $^{1}H/^{13}C$ RF volume coil.

I have greatly benefited from the time we spent on evaluating two other detector readout ASICs for our PET insert. This included the collaboration with a group of researchers at Physics Department E18. Most of all, I would like to express my gratitude to Igor Konorov, for his extremely helpful and interesting lectures and lab course on FPGA-based signal processing. I would also like to thank Dmytro Levit and Dominic Gaisbauer for the time they spent with me to practice FPGA programming and Martin Losekamm for sharing the results of their measurements on evaluation of a detector readout ASIC. Furthermore, I would like to thank Michael Traxler from GSI Helmholtzzentrum in Darmstadt, who sent us a test package of TRB3 and Padiwa3 boards and provided great support during my measurements with these boards.

My doctoral thesis provided a great opportunity for me to spend 7 weeks at the Molecular Imaging Instrumentation Laboratory (MIIL) at Stanford University. I would like to acknowledge TUM Graduate School for supporting this research stay. I am very thankful to Prof. Craig Levin from Stanford University for accepting me there. His advices and comments were very helpful for my PhD project. During my stay at MILL, I benefited from discussions with the members of this group. Particularly, the discussions with Shiva Abbaszadeh, Chen-Ming Chang, and Garry Chinn were very illuminating and I am thankful to them. Very special thanks also go to Amir Safaripour, whom I met during this trip, for all of his extraordinary support since then. Thank you Amir, not only for your scientific assistance in understanding the topics related to electromagnetic waves, but also for continuously bringing a smile to my face. You filled my life with hope and happiness and proved that 9600 km-distance is just a number.

I would like to express my deepest sense of gratitude to my parents, Maryam Marandian and Saeed Omidvari, and my sister Neda Omidvari, for their unlimited love and support. I have been extremely lucky to have you as a family. I have been feeling safe in taking every step through my life, because I knew that you will be standing behind me in case I slip or fall. Maman, so many special thanks for planning everything so carefully during our childhood and being so responsible about our education and extracurricular activities. Watching you working all these years as a successful engineer and manager in a masculine society and work environment, made me a strong woman who believes in her abilities. Baba, I cannot thank you enough for who you have been and what you have provided for me. Thank you for always being there for me when I was going through difficult moments. Thank you for always feeling proud of me. This made my heart warm and gave me confidence. My dearest Neda, you have been the best sister one could ever wish for and you have been my best friend all my life. Words are not powerful enough to express my love and gratitude to you. You have a big share in all my achievements through my life. Finally, I am forever in debt to my grandmother, Mahvash Hakhapour, for all she has done for me and my sister particularly through our childhood. Maafash, thank you for everything.

Contents

List of Figures

List of Tables

Acronyms

ADC	analog-to-digital converter.
APD	avalanche photodiode.
ASIC	application-specific integrated circuit.
BW	bandwidth.
CNR	contrast-to-noise ratio.
CSI	chemical shift imaging.
CT	computed tomography.
CTR	coincidence time resolution.
CZT	cadmium zinc telluride.
DAC	digital-to-analog converter.
DCR	dark count rate.
DOI	depth-of-interaction.
EMI	electromagnetic interference.
EPI	echo planar imaging.
FBP	filtered backprojection.
FF	fill factor.
FID	free induction decay.
FLASH	fast low angle shot.
FOV	field-of-view.
FPGA	field-programmable gate array.
FSE	fast spin echo.
FWHM	full width at half maximum.
FWTM	full width at tenth maximum.
GM-APD	Geiger-mode avalanche photodiode.
GRE	gradient echo.
HDMI	high-definition multimedia interface.
ICS	inter crystal scattering.
ID	inner diameter.
IDC	insulation-displacement contact.
LOR	line-of-response.

MADPET4	Munich Avalanche Diode PET 4.
MC	Monte-Carlo.
ML-EM	maximum-likelihood expectation-maximization.
MRI	magnetic resonance imaging.
MRS	magnetic resonance spectroscopy.
NEMA	National Electrical Manufacturers Association.
OD	outer diameter.
OS-EM	ordered-subsets expectation-maximization.
PCB	printed circuit board.
PDE	photon detection efficiency.
PEM	positron emission mammograph.
PET	positron emission tomography.
PMT	photomultiplier tube.
ppm	parts per million.
RARE	rapid acquisition with relaxation enhancement.
RC	recovery coefficient.
RF	radio frequency.
ROI	region-of-interest.
Rx	receive.
SD	standard deviation.
SE	spin echo.
SF	scatter fraction.
SiPM	silicon photomultiplier.
SMD	surface-mount device.
SNR	signal-to-noise ratio.
SOR	spill-over-ratio.
SPECT	single photon emission computed tomography.
SRM	system response matrix.
SSRB	single slice rebinning.
STIR	software for tomographic reconstruction.
TDC	time-to-digital converter.
TE	echo time.
TOF	time-of-flight.
ToT	time-over-threshold.
TR	repetition time.
Tx	transmit.
via	vertical interconnect access.

Chapter 1

Introduction

The principle of molecular imaging is use of labeled compounds for targeting specific proteins or genes, to directly visualize certain biological mechanisms involved in human health and disease (Cherry, 2004). Growing advances in identification of proteins and genes associated with certain diseases, the sequencing of human and mouse genomes, and the increasing variety of candidate molecules that can be used for labeling have made molecular imaging a hot and promising research topic (Cherry, 2004, Rowland and Cherry, 2008). Due to similarity of the mouse genome to human genome, many human diseases are closely modeled in mice by genetic manipulation (Rowland and Cherry, 2008, Vandamme, 2014). Therefore, advances in small animal molecular imaging, which enable successful targeting of proteins and genes *in vivo* in animal models, can be used for diagnosis, disease staging, treatment evaluation, and drug development for human diseases.

Positron emission tomography (PET) and single photon emission computed tomography (SPECT) are the two major *in vivo* molecular imaging modalities in nuclear medicine, in which the compound used for targeting is labeled with a positron-emitting or a gamma-ray emitting radionuclide. The particular advantage of using radio-labeled compounds in these two nuclear medical imaging modalities, compared to other molecular imaging techniques, is providing high sensitivity to detect low concentrations of the labeled compounds (Cherry, 2004, Cherry et al., 2012). This important advantage in addition to the availability and growing number of radio-labeled compounds for different biological processes, and the ability of these imaging modalities to provide quantitative images of the radionuclide distribution at high depths in the tissue have made PET and SPECT established molecular imaging techniques in a large number of applications. PET and SPECT have different strengths and limitations, which are mainly contributed with the detection principle and the type of radionuclide used for each of

the two modalities (Rahmim and Zaidi, 2008). Among these differences, the higher sensitivity of PET and the short half-life of many positron-emitting radionuclides allow for better dynamic studies and make small animal PET scanners specifically very interesting. Although considerable advances have been already achieved in small animal PET, there are still several areas of research with potential of dramatic improvements. This mainly includes development of new highly-specific targeted radio-labeled compounds, advances in data processing and 3D image reconstruction algorithms that can model the physical interactions and the system geometry, and developments in PET instrumentation, which is strongly correlated with radiation detector design.

Lack of anatomical information in PET images and the physical resolution limitations of PET, in addition to the motivation to have complementary information on a targeting subject from two different imaging modalities or to target more than one molecular target at the same time, have been the main driving forces for the recent developments of hybrid multi-modality imaging systems with PET scanners (Cherry, 2004, 2009, Judenhofer and Cherry, 2013). Although, combined PET/computed tomography (CT) scanners have already become widely used multi-modal systems in preclinical and clinical settings for many years with proven applications, combination of PET with magnetic resonance imaging (MRI) scanners has been also explored by several research groups and has led to a number of commercial systems. Small animal PET/MRI systems have become of special interest due to the ultra-high resolution of small animal MRI scanners, which offer excellent soft-tissue contrast with various established pulse sequences, providing effective tools for measuring anatomical and physiological changes in the body. Additionally, the high costs of MRI instrumentation has been a supplementary driving force to develop small animal PET scanners that can be inserted in already existing MRI systems. Compromises in the design of such PET inserts should minimize the deterioration of resolution, sensitivity, and image quality in both modalities, when the two systems are operated simultaneously.

1.1 Contributions

In this dissertation, a small animal PET insert is developed and characterized for a 7 T MRI scanner. The PET insert uses two offset layers of scintillation crystals, which are individually read out by high-gain silicon photomultipliers (SiPMs). The crystals and the SiPMs, which are the two key elements of photon detection in PET, were chosen during the design of the PET insert based on an experimental characterization

study on different scintillation crystal materials and SiPMs. In this study, five types of SiPMs with an active area size of 1.2×1.2 mm^2 were characterized. The SiPMs differed in the production technology and had micro-cell sizes of 25, 50, 75, and 100 μm. Performance of the SiPMs was evaluated in terms of their breakdown voltage, temperature sensitivity, dark count rate, and correlated noise probability. Subsequently, energy resolution and coincidence time resolution of the SiPMs were measured with five types of $1.5 \times 1.5 \times 6$ mm^3 crystals, including two Ce:LYSO, two Ce:GAGG, and one Pr:LuAG.

The PET insert was developed with a novel detector arrangement, in which the crystals are placed in a 3D-printed ring structure and all crystals in each ring face the center of field-of-view. This design offers high number of symmetries in the scanner, which were exploited in an iterative image reconstruction algorithm based on a Monte-Carlo system response matrix. Use of individually read-out high-gain SiPMs in this design enabled placement of active electronic components outside the MRI scanner, as the SiPM charge was transfered to outside the scanner by 1.5 m coaxial cables. By this approach, while PET ring thickness is minimized, RF interference from PET electronics on MRI are reduced. Furthermore, the design allows optimization of shielding enclosures for the insert and the readout electronics separately.

To study the advantages and limitations of such design, PET performance of the insert was evaluated and compared to other small animal PET scanners using the NEMA NU 4 standard measurements, followed by imaging a hot-rod spatial resolution phantom and two *in vivo* simultaneous PET/MRI scans on mouse heart and brain. The interferences between the PET insert and a 7 T MRI system were studied with three RF coil configurations, while the insert and its electronics were not shielded. First, with a ^{1}H large volume coil enclosing the insert, used for RF transmission and reception, second, with the large volume coil used only for RF transmission and a flexible surface coil for RF reception, and third, with a ^{1}H/^{13}C small volume coil shielded by a copper tube inside the PET insert.

1.2 Outline

This dissertation is organized in three main parts. The first part, compromised of chapter 2, provides a review of the fundamentals required for comprehension of this work. This includes the basic principles of PET and MRI, the individual components of the two systems, and the important parameters affecting the performance of a small

animal PET insert. The second part, compromised of chapter 3, 4, and 5, presents the contributions of this dissertations during the different phases of design, development, and characterization of a small animal PET insert for a 7 T MRI scanner. The characterization study performed on different scintillation crystal materials and SiPM technologies is presented in chapter 3. The development of the PET insert is described in chapter 4 and includes the individual hardware and software components of the system. Furthermore, the PET performance of the insert is evaluated and compared to state of the art preclinical PET scanners in this chapter. Finally, MR-compatibility of the PET insert is studied in chapter 5 with three RF coil configurations. Each of the three chapters provide a literature review on previous developments, motivations, and challenges corresponding to the topics covered in the chapter. The third and the final part of the dissertation, in chapter 6, provides concluding remarks and discusses the future prospectives for the project.

Chapter 2

Fundamentals

2.1 Positron emission tomography

Radiation has been used for medical applications since the discoveries of radioactivity, radium, and x-rays in 1890s (Cherry et al., 2012). Several later developments in physics, biochemistry, and image reconstruction methods led to use of artificially produced radionuclides for labeling molecules, known as radio-tracers, for medical imaging. This concept was used with positron-emitting radionuclides in positron emission tomography (PET), and the first successful PET scanner was built in 1973 by the research group led by Michael Phelps and Edward Hoffman of Washington University (Nutt, 2002, Phelps et al., 1975).

2.1.1 The basic principles

Physics in PET incorporates the fundamentals of two classes of high-energy radiation, particulate radiation and electromagnetic radiation, and is explained in great details in the textbook by Bailey et al. (2009). These high-energy radiations are classified as ionizing radiations, as they have sufficient energy to remove electrons from atoms, and are the sources of radiation dose to the patients during a PET scan. Particulate ionizing radiation involves emission of particles, such as alpha (α), beta (β^-), and positron (β^+), during the radioactive decay of structurally unstable isotopes. Electromagnetic radiation, as proposed by Einstein, could be viewed as a wave-like radiation of photons, with the energy characterized by the radiation wavelength. In the context of ionizing radiation, this includes x-rays and gamma (γ) rays. Among the two mentioned classes of ionizing radiation, positron emission and gamma rays are the ones used in PET.

Positron emission during the radioactive decay of a proton-rich atom is the starting point for PET physics. During this process, a proton from the atom nucleus is converted to a neutron and the positive charge is carried by emission of a positron, which

is the antimatter conjugate of electron. After the emission, positron starts to lose its kinetic energy through ionization events with its surrounding matter and deflects from its original pathway. The distance that the positron takes to reach rest is referred to as positron range. The positron at rest combines with an electron in rest from the surrounding matter. This could result in either formation of a metastable non-nuclear hydrogen-like element called positronium or direct annihilation of both particles with electromagnetic radiation in form of γ-rays. In water or human tissue, direct annihilation happens in about one-third of cases (Bailey et al., 2009). The electromagnetic radiation from annihilation, in most probable form, is back-to-back simultaneous emission of two 511 keV photons. This released energy is a result of conversion of the mass of positron and electron to energy. Non-zero momentum during annihilation results in emission of some photon pairs not strictly at 180° from each other, causing an uncertainty of 0.5° full width at half maximum (FWHM) from 180°, which is referred to as photon non-collinearity (Bailey et al., 2009, Cherry et al., 2012). A simplified illustration of the positron emission process and the following positron-electron annihilation is depicted in figure 2.1.

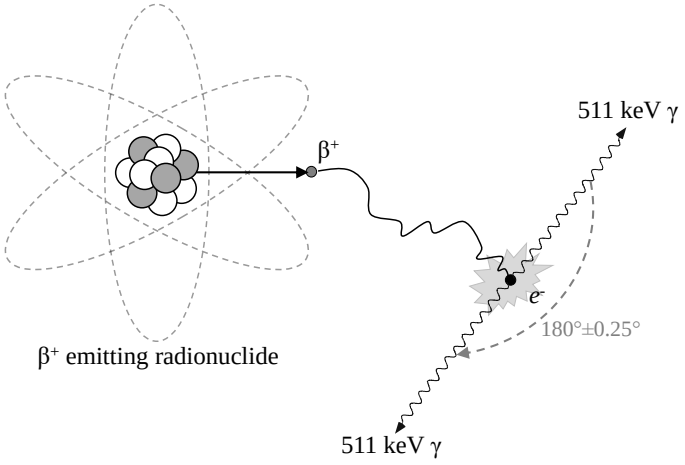

Figure 2.1: The process of positron emission from a radionuclide and positron-electron annihilation resulting in back-to-back emission of two 511 keV photons. The depicted positron range and photon non-collinearity are the two physical resolution limiting factors in PET.

The two back-to-back emitted 511 keV photons are detected by a ring of PET detectors for each decay process occurring in the compound labeled with a positron-emitting radionuclide. This is the basis for locating a metabolic process and its rate of occurrence in PET. However, since the detection principle in PET is based on the

annihilation photons, positron range and the photon non-collinearity are two physical limitations on localization of the radio-nuclides used in PET. The resolution blurring due to photon non-collinearity depends on the PET ring diameter (Sánchez-Crespo and Larsson, 2006), and by assuming a Gaussian distribution, it can be estimated by a factor of 0.0022 of the diameter (Phelps, 2004). Positron range varies for different radionuclides, depending on the energy spectrum of the positron and also its traveling medium (Levin and Hoffman, 1999). Simulations of positron range have shown that in case of ^{18}F, which is the most commonly used radionuclide in PET, positron range in water shows a non-Gaussian distribution with 0.1 mm FWHM, while with ^{15}O in water the FWHM is 0.5 mm (Levin and Hoffman, 1999). This resolution blurring could be more of a concern in high resolution preclinical PET scanners. However, hardware-based and software-based approaches exist to reduce this effect, one of which is use of strong magnetic fields as employed in preclinical MRI scanners (Phelps, 2004, Rahmim and Zaidi, 2008).

When two gamma rays are detected by two opposing detectors near-simultaneously, the event is referred to a coincidence. The two main characteristics of annihilation photons is their simultaneous emission and equal 511 keV energy. Therefore, their arrival time to the detectors and the detected energy play the most important roles in confirming that a coincidence event was due to an annihilation. Coincidence detection allows to localize the annihilation point along a line between the two detectors. However, since the exact interaction point in the detectors cannot be determined, the line in reality becomes a 3D volume connecting the two detectors. This line or volume is referred to as a line-of-response (LOR) and several LORs from different detector pairs are used to generate a PET image.

2.1.2 Radio-tracers

Positron-emitting radionuclides used in PET are generally attached as labels to compounds of biomedical interest and are injected into the patient. The radiolabeled compound is commonly referred to as a radio-tracer or simply a tracer. The biological properties of the radio-tracer is affected by the labeling strategy. Small compounds are usually labeled either by directly substituting a stable atom in the molecule with a radioactive atom of the same element or creating analogs of the original compound (Cherry et al., 2012).

By direct substitution, the radio-tracer has exactly the same biologic properties as the unlabeled compound and undergoes the same distribution and metabolism. ^{11}C, ^{13}N, and ^{15}O are examples of positron-emitting radioactive isotopes of elements that are widely found in nature and can be directly substituted. Analogs, on the other hand, allow replacing part of the original compound with radioactive isotopes of other elements that are less commonly found in nature, but have beneficial biological properties (Cherry et al., 2012). An example of such radioactive isotopes is ^{18}F, which is used for labeling several compounds for PET. The most widely used positron-emitting radio-tracer is the glucose analog, fluorodeoxyglucose (^{18}F-FDG), which is used for measuring metabolic rates of glucose in cancer, neurological disorders, and myocardial diseases. In this radio-tracer, the hydroxyl (OH) group on the second carbon of the glucose molecule is replaced with ^{18}F. Although different behavior of analogs compared to the original compound has to be carefully studied to provide precise quantitative results, the changes in biological properties could be beneficial by changing the rates of uptake, clearance, or metabolism (Cherry et al., 2012).

There are several important parameters, which have to be considered in use of radio-tracers. Specific activity of a radio-tracer is defined by the ratio of radioisotope activity to total mass of the element present (Cherry et al., 2012). This determines the total mass of the administered compound and subsequently affects the radiation dose to the patient. Furthermore, the administered mass levels of the radio-tracer must not be toxic. Physical half-life of the radionuclide is another important factor and is defined by the time at which the activity is reduced to half of its initial value during the exponential radioactivity decay. The half-life of radionuclides used for labeling in clinical applications should preferably be within the range of minutes to hours, to reduce the radiation dose to the patients on one hand, while still having sufficient time for preparation of the radio-tracer and its injection to the body on the other hand (Cherry et al., 2012). While ^{18}F has a half-life of 110 min, short half-life of ^{15}O (122 s) has been a limiting factor for use of this radionuclide only in simple compounds such as $H_2{}^{15}O$.

2.1.3 Radiation detectors in PET

Beside the physical limitations on spatial resolution in PET, the radiation detectors primarily determine the spatial resolution. Furthermore, the detection efficiency of these elements affects the image data statistics and subsequently the image quality.

Inorganic scintillation crystals with activators are the most commonly used gamma-ray detectors in PET. These crystals are usually made of a dense crystalline scintillator material, in which energy deposition of annihilation photons results in emission of low-energy photons in the wavelength range of visible light. These low-energy photons are subsequently detected by a photo-detector and converted into electrical charge (Phelps, 2004). An excellent detailed review of various scintillation detectors and photo-detectors can be found in the textbook by Knoll (2010).

Electromagnetic radiation interacts in different ways with its surrounding matter, which primarily depends on the radiation energy. This includes photoelectric effect, pair production, Compton scattering, coherent or Rayleigh scattering, triplet production, and photo-nuclear reactions (Bailey et al., 2009). Among these interactions, the photoelectric effect and Compton scattering are the two most relevant mechanisms to the radiation energies in PET and are particularly involved in detection of annihilation photons in scintillation crystals. The important role of these two interactions is in transferring the energy of the annihilation photons to the scintillator material.

In the photoelectric effect, a high-energy photon interacts with an orbital electron (usually from the inner shell) of an atom (Bailey et al., 2009). If the energy of the incident photon is higher than the binding energy of the orbital electron, the photon transfers all of its energy to the electron by ejecting the orbital electron from the atom. In Compton scattering, the photon loses only a fraction of its energy to eject a loosely bound electron and deflects from its original path through an angle proportional to the lost energy (Bailey et al., 2009). The change of direction and energy loss are especially important as they introduce errors in identification of original annihilation point.

2.1.3.1 Inorganic scintillation crystals

The electrons in the crystal lattice of the materials used in inorganic scintillation crystals have discrete bands of energy (Knoll, 2010). The electrons in the so-called valence band are bound at the crystal lattice sites, but by absorption of energy, they can elevate to the conduction band, where they would have enough energy to freely move throughout the crystal (Knoll, 2010). As high-energy annihilation photons enter the scintillator material, they lose their energy by photoelectric effect or Compton scattering with the electrons in the valance band of the crystal. Elevation of these electrons to the conduction band leaves a hole in the valance band. To bring back the atom to the ground state, the electrons need to return to the lower energy bands

by releasing scintillation photons. Since the typical gap widths in scintillators are too high to result in scintillation photons in the visible wavelength range, small amounts of an impurity are added that are referred to as activators. This impurity doping creates special activator sites in the lattice, which are ionized by the drift of the hole in the valence band. In this case, the free electron in the conductance band can drop to the activator site and de-excite quickly with lower energy gaps, leading to release of visible photons. Decay time of these excited states determines the time characteristics of the scintillation light (Knoll, 2010). Some examples of these activator additions to scintillation crystals used in PET are thallium, cerium, and praseodymium ions.

The function of scintillation crystals in measuring the energy of an incoming annihilation photon is to absorb the energy from the photon and generate optical photons, in a quantity proportional to the absorbed energy and in a wavelength range that can be detected efficiently by the photo-detectors. Furthermore, they should provide precise information about the arrival time of the incident photon. There are several important properties for scintillation crystals to meet these requirements (Bailey et al., 2009, Knoll, 2010, Khalil, 2011). The main characteristics are: high stopping power for 511 keV photons, high probability for photoelectric effect, high scintillation efficiency in converting the radiation energy to scintillation photons, high light output to provide sufficient scintillation light for the photodetectors, and short decay time to improve the timing of coincidence detection. This makes crystals with high density and high effective atomic number particularly interesting for PET, as they can provide a high stopping power. Furthermore, the photoelectric effect probability for 511 keV photons is higher for high atomic numbers (Khalil, 2011).

Beside the characteristics of the scintillator material itself, the scintillation light transport inside the crystal and to the photo-detector also affect the detected signal. This includes the effects from crystal size, surface treatment, and the optical coupling between the crystal and the photo-detector. Furthermore, since the scintillation photons are emitted in the crystal in all directions, the scintillator is usually covered or coated with a reflecting material on all sides except the side that is coupled to the photo-detector.

2.1.3.2 Silicon photomultipliers

Conversion of the scintillation photons to electrical charge was conventionally performed by photomultiplier tubes (PMTs) in PET scanners. However, developments in

semiconductor-based photodiodes, more specifically silicon photomultipliers (SiPMs), have proved them as suitable substitutions to PMTs. The principles of charge generation in different semiconductor-based photodiodes are described in details in the textbook by Sze and Ng (2006).

The charge generation function in SiPMs can be explained by the physical properties of junction between different types of semiconductors. In p-type semiconductors, the semiconductor material is doped with impurities, in which a vacancy (acceptor site) is created in the outer shell of the impurity after covalent band formations with the semiconductor atoms. Whereas, in n-type semiconductors, one electron (donor site) is left in the valance band of the impurity atom. Bringing p-type and n-type semiconductors together in good thermodynamic junctions, results in diffusion of electrons due to the charge gradient between two materials. As the acceptor sites are filled and donor sites are ionized during the diffusion, a negative space charge on the p-side and a positive space charge on n-side are built, which act as an electrical field against the charge gradient in the junction, resulting in a steady state charge distribution. Part of the junction region, in which filled acceptor sites and ionized donor sites are immobilized, has a charge imbalance and is called the depletion region.

Absorption of the energy from the incoming scintillation photons creates electron-hole pairs in the depletion region. These created electrons and holes are the only mobile charge carriers that can move freely through this region. When a voltage is applied to a p-n junction, the size of the depletion region changes depending on the direction and strength of the applied bias voltage. When the applied bias voltage is in reverse direction, the thickness of the depletion region increases and the electron-hole pairs created by the scintillation photons move in the direction of the applied voltage. The resulting current is the summation the diffusion current and the drift current from the electron-hole pairs, which are in opposite directions.

If the applied reverse bias voltage is increased, the electrons created by scintillation photons start to accelerate and collide with bond electrons, resulting in an avalanche multiplication of free electrons. In this case, the number of created carriers is linearly proportional to the number of absorbed scintillation photons. However, further increase of the applied reverse bias voltage makes the electrical field strong enough, in which the charge carriers get sufficient kinetic energy to produce additional electron-hole pairs through ionizing processes and create a self-sustaining avalanche. In this

mode, the device goes through a breakdown and the number of created charge carriers is the same, regardless of the number of absorbed photons. The photodiodes operated above breakdown voltage are called a Geiger-mode avalanche photodiodes (GM-APDs).

In SiPMs, each micro-cell is a GM-APD that gets activated by one photon, giving rise to a defined current controlled by a quenching resistor. These micro-cells are connected in parallel, so that the total current at the output is proportional to the number of activated cells. However, since the number of cells per SiPM pixel is limited, when the number of incoming photons increase, the SiPM response becomes non-linear. Since temperature increase could also create electron-hole pairs in semiconductors, the current due to these thermally generated electron-hole pairs is the main source of noise in SiPMs and is referred to as the dark current.

2.1.4 Detector signal readout

PET detectors generate pulses of electrical charge in response to the energy deposition in the detector. These pulses are analyzed in different ways by the readout electronics to provide the energy and timing of the detected photons. The readout systems generally have three basic components: preamplifiers, amplifiers, and the digitizer (Cherry et al., 2012). Since the pulse signals from PET detectors usually have relatively small amplitudes, preamplifiers are used to amplify the signals at an early stage. Furthermore, preamplifiers match the impedance levels between the detectors and the electronics and shape the detector signal pulse for optimal signal processing in the next level. This shaped pulse is further amplified in the next level by the amplifiers and its slow decaying pulse is reshaped into a narrow one to optimize the performance at high count rates and improve the electronic signal-to-noise ratio (SNR) (Cherry et al., 2012). The analogue pulse from the amplifier has to be converted into a digital signal in the digitizer, to provide the energy and time information about each detected event.

There are several methods for extracting the time information from the pulse signal (Cherry et al., 2012). These methods are generally based on applying a threshold level on the leading edge of the signal in a discriminator. Since the timing of the output pulse based on a constant threshold depends on the amplitude of the input pulse, more advanced discrimination techniques such as zero-crossover, peak detection, and

constant fraction are used for fast-timing (Cherry et al., 2012). Subsequently, the output from the discriminator is digitalized by time-to-digital converters (TDCs).

The pulse height or charge integration are conventionally used for energy measurement. Analog-to-digital converters (ADCs) have been one of the most widely used components for this task, which provide good linearity and precision in energy measurement. Another method for deriving the energy information based on charge measurement is the time-over-threshold (ToT) method. This method is based on the idea of using a comparator with a preset threshold to generate a pulse at the output with a width equal to the time, during which the input signal exceeds the threshold (Kipnis et al., 1997). Alternatively, two different threshold levels can be used for the discriminators of ToT (Rolo et al., 2013) or the threshold can be change dynamically based on feedbacks from the output (Shimazoe et al., 2009). Compared to pulse height measurement with ADCs, the ToT method offers simpler circuitry, higher integrity, and lower power dissipation (Shimazoe et al., 2009). However, the main limitation of this method is the nonlinearity of the ToT signal as a function of energy, which usually degrades the energy resolution and distorts the energy spectrum.

2.1.5 Coincidence detection

As the annihilation photons are detected by PET detectors and the generated signal is read out by the electronics, coincidence detection is performed by the coincidence logic unit of the PET scanner based on three main parameters: the arrival time of the two detected photons, their energy, and the location of two detectors. Although material, dimensions, and design of the individual detector modules play important roles in precision of these three parameters, the scanner geometry, the readout electronics, and the coincidence detection algorithm also affect the final result.

If two photons are detected within a predefined coincidence time window and the subsequent LOR formed between the two detectors corresponds to a meaningful LOR within the field-of-view (FOV) of the scanner and the detected energy of both photons are within a predefined energy window, the coincidence is valid and is referred to as a prompt event. Several effects result in errors in coincidence detection in PET. These effects mainly include limited resolution of the detectors and the readout electronics in timing and energy, finite dimensions of detectors and scanner, limited stopping power of the scintillation crystals, and attenuation and Compton scattering of gamma rays in the subject and scanner parts. Therefore, the prompt events are generally classified

into three groups (Bailey et al., 2009). These three classes include true, scattered, and random coincidences, which are shown in figure 2.2.

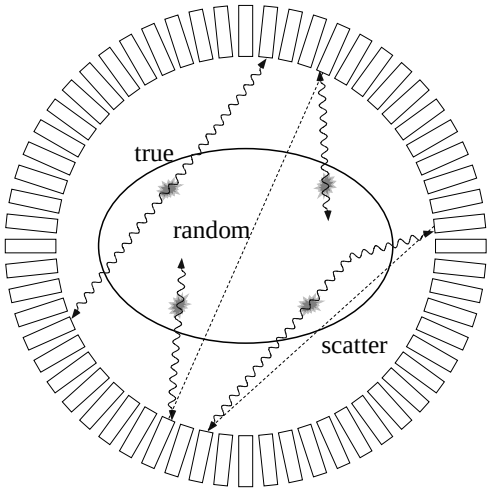

Figure 2.2: Three different classes of coincidences in PET. Scattered and random coincidences could lead to errors in the identification of LORs, which are shown by dashed lines.

If both photons detected within a coincidence window are originated from a single annihilation event and have not interacted significantly with their surrounding matter, the prompt event is called a true coincidence. The second class of prompt events is called scattered coincidences, which happens when one or both of the detected photons from a single positron annihilation have undergone a Compton scattering. Although Compton scattered photons have lost part of their energy and can be discriminated by energy thresholding, the limited energy resolution of PET detectors results in detection of part of these events as prompt coincidences. This leads to decreased contrast and inaccurate quantification in the reconstructed PET image (Bailey et al., 2009). Finally, if the two detected photons are from two different annihilations occurring approximately at the same time, the event is called a random coincidence and is spatially uncorrelated with the distribution of tracer (Bailey et al., 2009). The rate of random coincidences between two detectors is linearly proportional to the single event rates of the two detectors and length of the coincidence time window.

The sensitivity of a PET scanner is one of the major determinants of the final image quality. The system sensitivity is defined for a specific imaging phantom as the number of counts detected per unit of activity. Although, the energy threshold and the coincidence time window used for coincidence detection alter the system sensitivity,

there are several factors in the scanner design that have substantial impact on it. This mainly includes the detection efficiency of individual detectors at 511 keV, the solid angle coverage of the detectors with respect to the source location, and the detector packing fraction.

Compton scattering in scintillation crystals also affects the image quality. When an annihilation photon goes through two or more interactions in scintillation crystals (at least one Compton scattering and one photo-electric effect) and these interactions are measured in at least two different scintillation crystals, the event is called an inter crystal scattering (ICS) event. As the size of scintillation crystals decrease and their packing fraction increase, the number of ICS events increases. If low energy thresholds are used in the coincidence logic, ICS events can result in three or more detected photons in the coincidence time window, which are all originating from the same annihilation event. These events are usually discarded during the coincidence sorting and are not used during the reconstruction. Using higher energy thresholds in the coincidence logic unit will also lead to discarding one of the interactions, which is not necessarily the later interaction, resulting in detection of a scattered coincidence with a misidentified LOR.

Beside the physical limitations on spatial resolution, the geometry of the scanner and the PET detector design significantly contribute to the quality and resolution of the final image. Scintillation crystals can be used in two general forms of pixellated discrete or continuous monolithic detectors. In a pair of discrete crystals, the width of the individual detector elements and the distance of the source from the detectors primarily define the spatial resolution (Cherry et al., 2012). In continuous crystals, the intrinsic spatial resolution of the detector is determined by the statistics of scintillation photons. Furthermore, similar to discrete crystals, the spatial resolution degrades as the location of the source gets closer to one detector or another. However, the change in the spatial resolution as a function of the source location is different for discrete detectors and continuous detectors (Cherry et al., 2012).

Recovery coefficient (RC), measured for spherical objects as a function of object diameter, is an indicative of the spatial resolution performance in a PET scanner. RC is calculated as the ratio of the measured activity concentration by the actual activity concentration and is lower in smaller objects due to an effect known as the partial

volume effect (Phelps, 2004). This effect is particularly important in qualitative and quantitative characterization of small lesions or structures.

The thickness of the scintillation crystals leads to another resolution-degrading geometric effect, called the parallax error. This effect is shown for a ring geometry of pixellated crystals, in figure 2.3. The parallax error is due to the fact that annihilation photons can interact at any depth in the scintillator (Phelps, 2004). As a substantial thickness of scintillator material is required to provide efficient stopping power for annihilation photons, the amount of broadening effect due to parallax error is increased by increasing the crystal thickness and is worsened as the source is moved towards the edges of the FOV. This error can become especially important in preclinical PET scanners. Estimating the depth-of-interaction (DOI) in PET detectors could partially correct for this error.

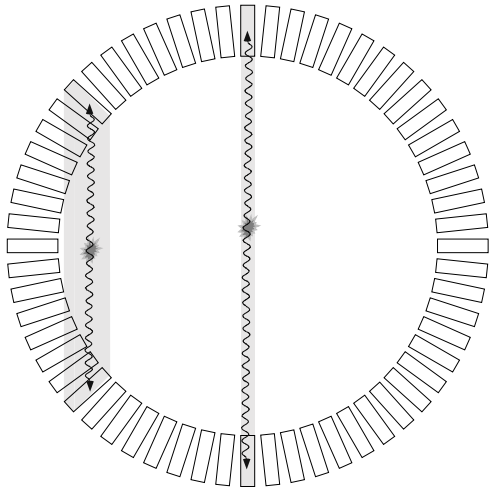

Figure 2.3: Resolution degradation towards the edges of the scanner FOV, due to parallax error.

2.1.6 Scanner design

Detector design and arrangement are the two initial steps in development of a PET scanner, which primarily define the ultimate performance potentials of the system. Today, all commercial PET scanners and most of the clinical and small animal PET systems designed by research groups use a full-ring cylindrical geometry, composed of inorganic scintillation crystal blocks.

In clinical systems, improving the time resolution of detectors has been an active area of research to provide time-of-flight (TOF) information for image reconstruction. In-

cluding TOF information improves the SNR ratio of the images, as the difference in the arrival times of the photons is directly correlated with the location of the annihilation event. Research in this domain mainly involves the developments in SiPM technology and the studies on improving the timing properties of inorganic scintillators. At detector level, coincidence time resolutions (CTRs) below 100 ps (FWHM) have been reported by several groups using SiPMs. Examples of such studies are use of new inorganic scintillation materials for PET (Schaart et al., 2010) and investigating the effects from the doping materials and their concentration on timing (Nemallapudi et al., 2015, Cates and Levin, 2016, Gundacker et al., 2016). Beside the developments with inorganic scintillators, some recent approaches have exploited the excellent timing properties of Cerenkov photons (Somlai-Schweiger and Ziegler, 2015, Kwon et al., 2016, Brunner and Schaart, 2017) or used organic plastic scintillators (Moskal et al., 2016, Kuramoto et al., 2017) with SiPMs for TOF-PET application.

Higher spatial resolution requirements for some organs, especially for brain and breast imaging, compared to the resolution provided by clinical whole-body scanners has resulted in development of organ-dedicated systems. Many of these systems have used unconventional detector arrangement geometries to achieve high resolution and sensitivity, while maintaining reasonable development costs and system complexity. Examples of these unconventional approaches include use of high resolution detectors in coincidence with conventional PET scanners (Qi et al., 2011, Mathews et al., 2013, Brzeziński et al., 2014, Wang et al., 2015b), use of dual flat panels of high resolution detectors for breast imaging (Hsu et al., 2016), axial alignment of long scintillating crystals combined with orthogonal wavelength shifting plastic strips in AX-PET scanner (Beltrame et al., 2011), and employing a helmet-PET geometry for brain imaging (Tashima and Yamaya, 2016). Similarly for high resolution preclinical systems, using solid-state cadmium zinc telluride (CZT) semiconductor photon detectors instead of scintillation crystals (Abbaszadeh et al., 2016) or flat-panels of BGO scintillation crystals coupled to position-sensitive PMTs (Gu et al., 2013) are investigated in four-sided box geometries.

In high-resolution scanners, which use long scintillators in circular geometries to achieve high sensitivity, the parallax error is especially an issue. Various detector designs and readout schemes have been proposed for DOI estimation to partially correct for this error. Many of the conventional designs were based on two widely used methods. The first method, known as phoswich design, uses two layers of scintillator

materials to provide a two-level depth information and the second method is based on dual-side readout of scintillator crystals (Phelps, 2004). Beside these two conventional methods, some examples of the most recent approaches used with pixellated crystals include use of pulse shape discrimination methods (Wiener et al., 2013, Chang et al., 2017) and binary position-sensitive networks (Bieniosek et al., 2016) in phoswich designs, placing reflectors at the crystal-end for light sharing between a crystal array (Pizzichemi et al., 2016), phosphor coating of scintillators (Berg et al., 2016), dual-side readout by multiplexed SiPM arrays (Kolb et al., 2014), 2-layer offset (Thompson et al., 2012) and 4-layer offset (Nishikido et al., 2015) crystal blocks, and 6-side SiPM readout of a block of cubic scintillation crystal elements (Inadama et al., 2016). In addition to all these methods, one-to-one coupling of scintillation crystals to photodetectors can be incorporated also in dual layer designs to include DOI information and offers the best count-rate performance. Furthermore, since there is no light-sharing between the individual detectors, ICS events can be properly studied in the scanner developed with this approach, in order to include these events in the image reconstruction to increase the sensitivity (Rafecas et al., 2003). However, the main limitation in such a system is the increased costs and complexity, due to the increased number of readout channels.

2.1.7 Image reconstruction

Image quality in PET is determined based on two primary factors, spatial resolution and photon count density (Qi and Leahy, 2006). Detector resolution defines the maximum limit on image resolution and photon count density determines the minimum noise in the final reconstructed image. The ultimate goal in PET image reconstruction is to quantitatively compute the true tracer distribution from the acquired data. Furthermore, the reconstruction algorithm should provide an optimal trade-off between spatial resolution and noise propagation, by accurately modeling the noise processes in photon detection data. PET image reconstruction approaches can be divided in two main classes of analytical and iterative methods.

Analytical reconstruction techniques are based on line-integral models, in which the number of coincident photon pair counts measured by a pair of detectors is proportional to the integral of the tracer density along the line connecting the two detectors. 2D filtered backprojection (FBP) algorithms are examples of analytical methods that have been widely used in nuclear medicine. The basic principle of 2D FBP recon-

struction relies on generating a 2D cross-sectional image of activity distribution from a slice within the object, using sinograms (Cherry et al., 2012). Sinograms are a set of projection data at different angles represented in a 2D matrix, where each projection (or a row of the sinogram) is a set of line-integrals from different detector pairs at a given angle. Although analytic 3D PET reconstruction techniques exist, rebinning algorithms, such as single slice rebinning, can also be used to rebin the 3D data into stacks of 2D sinograms and reconstruct them using 2D FBP reconstruction (Qi and Leahy, 2006).

Iterative reconstruction algorithms tend to require more computational power. However, they use probabilistic models, in which the photon detection process and statistical noise can be modeled more accurately (Qi and Leahy, 2006). In these approaches, unknown activity distribution is calculated by a set of equations from the measured projection data through a projection matrix, also known as the system response matrix (SRM). The elements of the SRM matrix provide the probabilities for an emission in each image voxel being detected by individual detector pairs. The SRM matrix can be directly measured through a set of high-statistic experiments, but also can be modeled through analytic, geometric, Monte Carlo, or combinations of these approaches.

Iterative reconstruction methods have generally two basic components, the cost function and the optimization algorithm (Cherry et al., 2012). The cost function includes the data modeling to provide an estimated image and compares the measured projection data to forward projections through the estimated image. Subsequently, a numerical algorithm is used for optimization, to maximize or minimize the cost function, and the estimated image is updated through back projection. These components are chosen in a way that the algorithm can converge to an estimated image that is close to the true image as rapidly and accurately as possible (Cherry et al., 2012). The computational cost of iterative algorithms are usually dominated by their forward- and backprojection procedures performed at each iteration (Qi and Leahy, 2006).

Noise in nuclear medical imaging is modeled by random Poisson distribution due to the nature of radioactive decay. Maximum-likelihood expectation-maximization (ML-EM) algorithms are successful examples of iterative reconstruction methods, in which statistical considerations based on Poisson models are included in the algorithm. Although these algorithms converge very slowly, the offer guaranteed non-negativity, convergence, and count preservation at each iteration (Qi and Leahy, 2006). Several

methods have been developed to speed up these algorithms, among which the ordered-subsets expectation-maximization (OS-EM) method (Hudson and Larkin, 1994) has become one of the most widely used algorithms in nuclear imaging. The method divides the projection data into a number of disjoint non-orthogonal subsets and applies the EM algorithm sequentially to each of these subsets in each iteration.

2.2 Magnetic resonance imaging

Discovery of the spin nature of the proton and several works on quantum mechanics of the proton spin interaction with a magnetic field led to measurement of the precessional signal of the spins around a magnetic field by Bloch and Purcell in 1946 (Brown et al., 2014). Their experimental work and theoretical explanations on this topic resulted in sharing a Nobel prize in physics in 1952 and this finding has been the basic principle of magnetic resonance imaging (MRI). The principles of MRI physics, instrumentation, and applications are provided in the textbooks by Brown et al. (2014) and Dale et al. (2015). An overview of the most relevant MRI fundamentals are provided here for understanding the MR-compatibility aspects of a PET insert. Beside the controller computers and data acquisition systems, there are three major components in MRI systems, which will be discussed here. These components are a magnet, a radio frequency (RF) system, and a gradient system.

2.2.1 The basic principles

One of the quantum properties of the nucleus is the intrinsic spin angular momentum, also known as spin, which depends on the atomic number and atomic weight of the nucleus. The nucleus spin is quantized to a limited discrete values in the nature, ranging in three groups of zero, integral, and half-integral values (Dale et al., 2015). The nuclei with non-zero spins can be viewed as rotating about an axis with a constant rate, producing a magnetic moment oriented parallel to the axis of rotation (Dale et al., 2015). This magnetic moment can be viewed as a vector, $\vec{\mu}$, with a definite orientation and magnitude, as shown in figure 2.4a, and will be referred to as the spin vector. The most frequently used nucleus in MRI is the ^{1}H nucleus, consisting of a single proton, which is abundant in the body within the water and fat molecules in most tissues. The ^{1}H nucleus with one proton has a spin of 1/2 and thus interacts with external magnetic fields. MRI measurements are based on inducing changes to the orientation

of a collection of nuclear spins in a tissue by application of an assortment of external magnetic fields and measuring these changes with a radio frequency coil.

The interaction of the nuclear spin with an external static magnetic field, $\vec{B_0}$, produces a torque, which results in precession of the spin vectors, with axis of precession parallel to $\vec{B_0}$ (Brown et al., 2014). The precession angular frequency of the spin vector is referred to as the Larmor frequency, ω_0, and is given by the Larmor equation:

$$\omega_0 = \gamma B_0 \tag{2.1}$$

where γ is the gyromagnetic ratio constant for the given nucleus. This is illustrated in figure 2.4b with a rotating frame of reference, in which the z axis is parallel to $\vec{B_0}$. During the proton precession, the z component of the spin vector has a constant magnitude and direction.

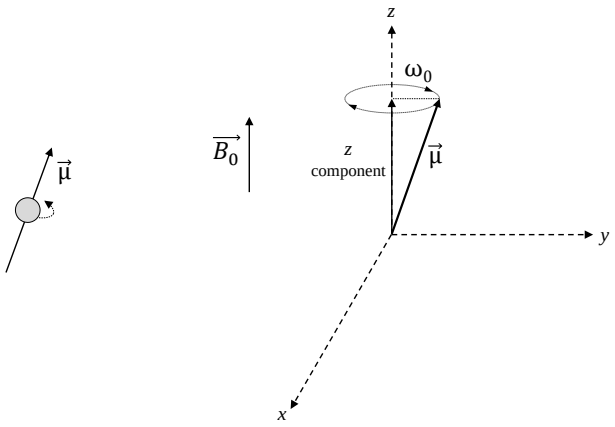

Figure 2.4: (a) The spin vector representing the magnetic moment, $\vec{\mu}$, of a proton and (b) its Larmor precession with angular frequency of ω_0 in presence of an external magnetic field $\vec{B_0}$ oriented at z direction.

In absence of any external magnetic field, in a volume of tissue, the proton spin vectors are randomly oriented in all directions, resulting in a vector sum of zero. In presence of an external static magnetic field, Zeeman effect between the proton and the external magnetic field results in splitting of nuclear energy levels, so that the z component of the proton spin vectors is quantized to only two possible values: parallel (spin-up) and anti-parallel (spin-down) to the field. The spins in the spin-up orientation are of lower energy. Therefore, in a collection of protons at body temperature, there will be

a very small excess of protons in spin-up state. Consequently, the vector sum of spin vectors in the tissue volume will be a positive vector parallel to $\vec{B_0}$ that only has a z component. This vector sum is called net magnetization $\vec{M_0}$ and does not vary with time (Dale et al., 2015).

Manipulation of net magnetization by application of external magnetic fields to the tissue is the source of MRI signal. For most materials, the magnitude and direction of the net magnetization $\vec{M_0}$ is proportional to the field strength and the magnetic susceptibility of the tissue. In a static magnetic field, where $\vec{M_0}$ is aligned with the field direction with no transverse component, the configuration of spins is at lowest energy level. Therefore, if this configuration is changed due to absorption of energy during the MRI scan, the protons will naturally try to return to this equilibrium configuration (Dale et al., 2015).

The static magnetic field $\vec{B_0}$ in the MRI system is provided by a magnet. MR magnets are available in a variety of field strengths. Most clinical MRI systems use 1.5 T or 3 T magnets and small animal MRI systems often use 3 T or 7 T magnets. However, other lower and higher field strengths in the range of 0.3 T to 10 T are also used for specific applications. The homogeneity or uniformity of the main magnetic field is an important parameter of the MRI scanner and is usually expressed within the imaging FOV in parts per million (ppm) scale, relative to the main field strength.

2.2.2 Radio frequency system

In presence of the $\vec{B_0}$ field, the energy difference (ΔE) between the two proton spin energy levels is:

$$\Delta E = h\omega_0 = h\gamma B_0 \tag{2.2}$$

where h is the Planck's constant, 6.626×10^{-34} Js. This energy difference is exactly proportional to the Larmor frequency ω_0 at the B_0 field strength. The protons in each of these two energy levels can go to the other energy level, only when energy at this frequency is applied to them. Upon application of the energy, since there are more spins at lower-energy state, there will be a net quantized absorption of energy exciting a number of protons from lower-energy state to the upper-energy state (Dale et al., 2015). This quantized energy absorption is referred to as resonance absorption and the associated frequency is called the resonant frequency.

The net magnetization of protons in a tissue can be rotated away from its alignment along the $\vec{B_0}$ by application of a RF magnetic field for a short time, referred to as a RF pulse (Brown et al., 2014). The RF pulses are sent from a transmitter coil and apply the energy for resonance absorption. They are typically transmitted with a narrow bandwidth (BW), with a central frequency matching to the resonant frequency ω_0 and an orientation perpendicular to $\vec{B_0}$. This can be treated as an additional effective magnetic field, referred to as $\vec{B_1}$, which is oriented perpendicular to $\vec{B_0}$. The orientation difference allows for energy transfer to the protons and absorption of the energy at resonant frequency results in rotation of $\vec{M_0}$, with an initial rotation direction perpendicular to both $\vec{B_0}$ and $\vec{B_1}$. The amount of resulting rotation is referred to as the pulse flip angle and depends on the amount of energy absorbed by the proton. This effect is shown in figure 2.5 for a 90° RF excitation pulse, resulting in a 90° flip angle.

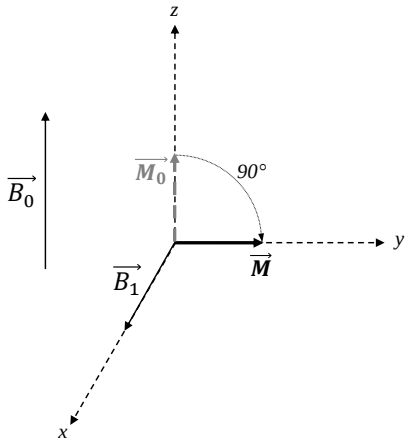

Figure 2.5: The effect of energy absorption from applying a 90° RF excitation pulse on the net magnetization.

When RF transmission is ended, the protons try to realign and return to the equilibrium orientation. During this process, the net magnetization vector $\vec{M}$ starts to precess about $\vec{B_0}$ at Larmor frequency. If a receiver coil composed of a loop of wires is placed perpendicular to the transverse plane, the process induces a voltage in the wires. This induced voltage, which is the following response to an RF pulse, is known as the free induction decay (FID) (Dale et al., 2015). The process in which the protons release their absorbed energy to return to the equilibrium state is called relaxation and results in decay of the FID signal in time, which can be characterized by three components of the FID signal: peak amplitude, frequency, and phase.

In a collection of spins in a specific tissue, two relaxation times can be measured, which indicate the constant rate of changes in the relaxation process over time. These two relaxation times, known as $T1$ and $T2$, are used as primary mechanisms for image contrast in MRI. As the net magnetization vector $\vec{M}$ is precessing to return to equilibrium state, the changes can be tracked separately in its z component, M_z, and its transverse component, $\vec{M_{xy}}$.

During relaxation, M_z follows an exponential growth to restore M_0. The time constant for this process is the $T1$ relaxation time, at which M_z returns to 63% of its original value (Dale et al., 2015). The changes of the transverse component $\vec{M_{xy}}$ are more complicated and are sources of the FID signal. At the end of the RF pulse, when the protons have absorbed the energy and the net magnetization vector has fully rotated, there is a phase coherence in the precession of protons in microscopic level. Subsequently, intermolecular and intramolecular interactions between adjacent spins start to cause transient fluctuations in the magnetic field. This results in fluctuations in the precessional frequency of protons and a gradual irreversible loss of phase coherence. As time elapses, the transverse coherence starts to gradually disappear and the transverse component $\vec{M_{xy}}$ decreases toward 0. $T2$ relaxation time is the time that the transverse magnetization reaches 37% of its initial value after the RF pulse, when the phase incoherence is solely due to the described effects. However, there are other factors that also cause fluctuations in the local magnetic field and contribute to loss of coherence. These factors include the magnetic field inhomogeneity from the main magnet and sample-induced effects, such as distortions due to differences in magnetic susceptibility of adjacent tissues. Therefore, the total transverse relaxation time, referred to as $T2^*$, also includes these effects and is the time constant for the exponential decay of FID signal's envelope.

The sources of dephasing that contribute to $T2^*$ relaxation are static during time and can be reversed by application of a 180° RF pulse, also known as a refocusing pulse, to have a signal with true $T2$ relaxation. This is done by application of an initial 90° excitation pulse, followed by a time delay t for dephasing through $T2^*$ relaxation, and subsequent application of a 180° pulse that would reverse the precession phase of protons relative to the resonant frequency. Another time delay of t after the 180° pulse will result in elimination of the contributions to $T2^*$ relaxation. This process of regaining parts of the transverse phase coherence induces a signal in the receiver coil,

known as the spin echo, in which the phase coherence and signal amplitude loss are only due to $T2$ relaxation (Dale et al., 2015).

RF coils can be produced in a variety of sizes and shapes. They can be designed dedicated for RF transmission or reception, or the same coil can have both functions. The RF transmitter should produce an effective $\vec{B_1}$ field perpendicular to $\vec{B_0}$, in which the protons within a defined volume experience the same amount of RF energy (Dale et al., 2015). RF waveforms of transmitter coil are adjusted by software to achieve the desired output. Although RF transmitters can be operated both at continuous wave mode and pulsed mode, most MRI measurements are based on pulsed mode operation, in which RF energy is broadcast for brief periods of time.

RF pulses are defined based on their center frequency, duration, phase, amplitude, modulation, and pulse shape. Pulse duration or pulse length defines the time that the waveform is broadcast and is inversely proportional to the transmit bandwidth. To produce a specific flip angle, the protons must absorb a certain amount of energy. This RF energy depends on the pulse amplitude integral and pulse duration. RF pulse shape refers to the time-domain shape of the function, modeling the transmitted waveform, and can be categorized in two classes of frequency selective and non-selective pulses (Dale et al., 2015). Non-selective pulse, also known as rectangular, block, or hard pulses, have a constant amplitude and short duration in time and a broad range of frequencies. Frequency selective pulses, also known as soft pulses, can have different shapes in time domain, including sinc, Gaussian, or hyperbolic secant. They are usually truncated in time compared to their theoretical mathematical function, but still have longer durations allowing for narrower frequency bandwidths.

In order to avoid electromagnetic interference (EMI) between the RF system of an MRI scanner and other systems operating simultaneously in its close proximity, EMI shielding enclosures are used. The principle of EMI shielding is that impingement of an electromagnetic wave with a conductive shield results in a current flow in the shield. The current density decreases as the depth in the shield is increased due to absorption and reflection of the electromagnetic wave (Lee et al., 2018). The residual current density on the opposite side of the shield defines the electromagnetic wave appearing after the shield. To simplify the EMI-shielding problem, the skin depth of a shield is defined as the depth at which the current density has reached e^{-1} of the current density at the surface. As a result, in a simple conductive shield layer, the electromagnetic

wave appearing on the opposite surface can be estimated by the exponential decay of the current as a function of shield thickness. However, estimating the EMI-shielding effectiveness becomes more complex is several cases such as when discontinuities appear in the shield. The frequency, the power, and the ratio of the electric and magnetic components of the electromagnetic wave, the distance of the EMI source from the shielding material, and the design and material of the shielding enclosure and its gaskets play important roles in the amount of electromagnetic wave appearing after the shield. In addition to these factors, conductivity, permeability, connectivity in current paths to preserve the continuity of current flow, and the thickness of the shield primarily define the absorption and reflection of the electromagnetic waves.

2.2.3 Gradient system

Gradients are linear perturbations superimposed on the main magnetic field $\vec{B_0}$, which typically produce total field variations of less than 1% (Dale et al., 2015). Three physical gradients are used in MRI, each of them for linear variations in one of the x, y, and z directions. Each of these gradients are generated by changing the electrical current in separate loops of copper wires in a gradient coil, connected to an amplifier (Dale et al., 2015). All gradients are centered at the center point of the magnet, known as the isocenter. These linear field variations in three orthogonal directions could produce a 3D linear encoding of the magnetic field as a function of location, due to which each proton would resonate at a unique frequency depending on its exact location. Gradient amplitude is usually expressed in millitesla per meter ($\mathrm{mT.m^{-1}}$).

MR images are formed based on frequency and phase maps of proton spins in selected slices. During an MRI scan, three functional gradients are required for three tasks of slice selection, readout or frequency encoding, and phase encoding. All of these functional gradients must be perpendicular to each other and the physical gradients of x, y, and z are assigned to one or more of the three functional gradients through the operating software for each specific imaging task. The direction of the gradient defines the normal vector for the planes, in which the component of the field in the gradient direction is held constant.

The initial step in an MRI scan is the slice selection for RF excitation. This is performed by defining the slice selection gradient, G_{SS}, as the first functional gradient and the adjusting the parameters of the RF excitation pulse. This is shown for two examples in figure 2.6, where axial slices have been selected by defining the direction

of G_{SS} in z direction. The gradient amplitudes are shown by the slope of the two lines passing through the isocenter of the scanner. During the slice selection, the gradient direction defines the slice orientation. The location of the slice is determined by the gradient amplitude and the central frequency of the RF pulse. Furthermore, the slice thickness is determined by the BW of the RF pulse and the amplitude of the slice-selective gradient. Typically, in pulse sequences, the excitation BW is fixed and amplitude of G_{SS} is changed for modifying the slice thickness, resulting in large G_{SS} amplitudes for thin slices (Dale et al., 2015).

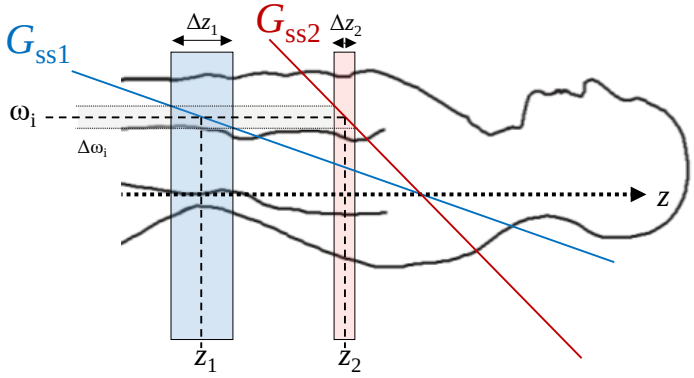

Figure 2.6: The slice selection process shown for two example axial slices, located at z_1 and z_2, when slice selection gradients are applied in z direction. Two gradient amplitudes are shown with the slope of the two lines passing through the scanner isocenter. The locations of the slices are selected by the G_{SS} amplitude and central frequency of the excitation pulse. The slice thickness in determined by the G_{SS} amplitude and excitation bandwidth.

After slice selection and excitation, the net magnetizations within the slice will precess at the same frequency. To encode the precession frequencies based on the position of the spin in the slice, a gradient is applied during echo formation, which is referred to as the readout or frequency encoding gradient, G_{RO}. Therefore, the echo signal measured by the RF receiver coil will contain superimposed frequencies, which are mapped to corresponding positions in the slice. The amplitude of G_{RO} is determined based on the FOV defined for the image and the receiver BW.

The third functional gradient is the phase encoding gradient, G_{PE}, which corresponds to the second direction in a 2D MR image. When G_{PE} in turned on, the precession frequency of the spins changes corresponding to their position along the applied phase encoding direction. By turning the G_{PE} off, the proton spins return to their previous

precessional frequency with an induced phase change, depending on the magnitude and duration of G_{PE}. Phase encoding is performed in a number of phase encoding steps, in which G_{PE} amplitude is changed.

Since the gradient fields are responses of the current flow in the gradient coil, they require a finite time to achieve their final maximum value when they are applied in form of gradient pulses. This time defines the rate of change in the gradient field and is referred to as the gradient slew rate. Another parameter measured for gradient pulses is the gradient duty cycle, which defines the percent of time that the gradient amplifier can sustain its response, when the gradient system is run at maximum power.

One of the complications of gradient pulses is generation of eddy currents in conductive materials, such as RF shields, due to time-varying magnetic fields. Eddy currents produce a magnetic field opposing the direction of change by the gradient in the magnetic field. This introduces distortions in the magnetic field, which change with time as the eddy currents decay with applied gradient pulses. The magnitude of the eddy current depends on the resistivity, size, and structure of the conductive material, as well as the field strength and gradient slew rate.

2.2.4 Pulse sequences

There are a variety of measurements techniques for obtaining images with different contrasts in MRI. These measurement techniques are known as pulse sequences. Pulse sequences are typically defined by a kernel, which is the fundamental unit of the sequence (Dale et al., 2015). The pulse sequences that were used in this dissertation for MR-compatibility assessment of the PET insert are briefly described in this section based on the hardware activity in their kernel. This includes spin echo (SE), gradient echo (GRE), and echo planar imaging (EPI) sequences. Repetition time (TR) in these pulse sequences is defined as the time between successive excitation pulses and the echo time (TE) is the time between the middle of the excitation pulse and the center of the generated echo signal.

SE sequences are one of the most widely used sequences in MRI, which can produce $T2$-weighted images. The kernel of these sequences typically consist of a 90° excitation pulse, followed by one or more 180° refocusing pulses generating the echo signals. A variation of SE sequence is the fast spin echo (FSE), also called rapid acquisition with relaxation enhancement (RARE) (Hennig et al., 1986). This sequence uses multiple

refocusing pulses and each echo signal has a different TE and is separately phase-encoded with a different G_{PE}. This schemes makes the data collection more efficient as different echos can be used as different lines in a single image. RARE sequence can be used for obtaining ultra-high resolution $T2$-weighted images with reduced scan time.

GRE sequences are also frequently used in MRI for different contrasts such as $T1$-weighted or $T2^*$-weighted images. No 180° refocusing pulses are used in these techniques and the echo signal is generated by application of gradients. After application of an RF excitation pulse, as dephasing is taking place due to $T2^*$ relaxation, a G_{RO} pulse with the same duration and magnitude is applied, with a polarity opposite to the G_{RO} pulse used during signal detection. This gradient with reversed polarity can rephase the spins and generate an echo signal. This gradient pulse is referred to as gradient reversal pulse and the echo signal generated by this techniques is called gradient echo. GRE sequences generally have shorter TR compared to SE sequences. Furthermore, GRE sequences usually use flip angles lower than 90°, which makes the total RF power used in these sequences generally lower than SE sequences. The FLASH (fast low angle shot) sequence was the first sequence developed based on this technique (Haase et al., 1986) and is still one of the most frequently used sequences.

EPI sequences, as first proposed by Mansfield (1977), are another class of pulse sequences used in MRI, which can be performed with very short acquisition times, but have a limited spatial resolution. The readout gradient G_{RO} is rapidly switched in EPI to produce series of gradient echos in each TR. In modern EPI techniques, each of these echos produced by switching gradients are separately phase encoded and used in the image reconstruction. Use of gradient echos in EPI, makes this sequence very sensitive to $T2^*$ effects (Dale et al., 2015). Therefore, magnetic susceptibility differences at tissue borders or inhomogeneities in the main magnetic field result in image distortions in EPI. There are different variations of this sequence to obtain different contrasts, such as FID-EPI and SE-EPI. FID-EPI uses a single RF excitation pulse, while SE-EPI has a pair of 90° and 180° pulses.

2.2.5 Magnetic resonance spectroscopy

Not all protons in the hydrogen atoms of different molecules have the same resonant frequency, when placed in a magnet producing $\vec{B_0}$ magnetic field. Different molecular environment of protons in different molecules results in local magnetic field varia-

tions. These local magnetic field variations are proportional to the main magnetic field strength B_0 and are the source of different resonant frequencies for protons in fat and water tissue in the body. These frequency differences are known as chemical shifts and are the basis for MR spectroscopy (MRS). MRS techniques allow examination of individual molecules and can be used to study the biochemistry of diseases (Dale et al., 2015).

Chemical shift values are expressed in ppm scale relative to the reference Larmor frequency of the main magnetic field, which makes them independent of frequency. However, MRS studies are more common with high-field magnets, since the individual signals and their absolute frequencies are higher at higher field strengths (Dale et al., 2015). ^{1}H spectroscopic studies can be performed with standard transmit/receive RF coils used for MRI. However, MRS studies of other nuclei, such as ^{13}C, require special coils designed for the resonance frequency of the specific nucleus.

Since small chemical shift values are the source of magnetic field variations and basis of MRS signal, these techniques are very sensitive to main magnetic field inhomogeneities. MRS signal readout is normally performed in absence of gradients and spatial encoding of the MRS signal is performed by alternative localization methods. Furthermore, MRS studies are usually limited to a small number of voxels, with voxel sizes usually larger than what used in MRI. There are two general classes of localization techniques in MRS: single voxel spectroscopy (SVS) and multiple voxel techniques. This classification is based on the number of separate voxels used for obtaining the frequency spectra during each measurement (Dale et al., 2015).

SVS techniques are usually based on using three RF pulses, each of them applied using a different physical gradient. The resulting echo is produced by protons located at the intersection of these three pulses and is read out to produce the frequency spectrum for the desired voxel in the tissue. In multiple voxel techniques, multiple spectra are obtained during one measurement. The most common method of these techniques is chemical shift imaging (CSI), also known as spectroscopic MRI. CSI techniques use RF pulses with phase encoding gradients applied in all spatial directions for spatial localization (Dale et al., 2015). They can measure the localized spectra from several volumes of tissue simultaneously and can be used to generate maps of metabolic concentrations.

Chapter 3

Characterization of silicon photomultipliers and scintillation crystals as detector modules for PET

This chapter has been published as "Omidvari N, Sharma R, Ganka T, Schneider F, Paul S & Ziegler S 2017 'Characterization of 1.2×1.2 mm^2 silicon photomultipliers with Ce:LYSO, Ce:GAGG, and Pr:LuAG scintillation crystals as detector modules for positron emission tomography' Journal of Instrumentation 12(04), P04012."[1]

3.1 Introduction

The continuing demand for better image quality, shorter scan time, and lower radiation dose to the patient has resulted in ongoing research in the field of positron emission tomography (PET). The performance of a PET scanner is directly affected by many design factors, including the geometry of the scanner, the detector modules, read-out electronics, data acquisition and processing, and image reconstruction algorithm. At the detector level, the scintillation crystal and the photo-detector are the two main components playing key roles, which are configured either by use of small pixellated scintillator elements or large monolithic crystals. In both approaches, the main goals are high spatial resolution over the entire field of view (FOV), high sensitivity, high count-rate performance, and good energy resolution and time resolution.

Silicon photomultipliers (SiPMs) have already been proven to be excellent photo-detector candidates for PET applications. They offer compactness, high photon detection efficiency, high internal gain, low operating voltage and power consumption,

[1] N. Omidvari conducted the research, authored the manuscript, performed the data analysis, and carried out the detector module characterization measurements. Current-voltage characteristic measurements were performed with assistance of T. Ganka. Measurements of breakdown voltage temperature dependency, dark count rate, and correlated noise probability were performed by R. Sharma and F. Schneider.

insensitivity to magnetic fields, and good time resolution (Renker and Lorenz, 2009, Renker, 2009, Ferri et al., 2014, 2016, van Dam et al., 2010). However, there is still an ongoing demand on SiPMs which are particularly improved in terms of dark count rate (DCR), optical cross talk, after pulsing, nonlinearity effect due to saturation of the SiPM cells, temperature sensitivity, and production technologies allowing for small micro-cells with high fill factors. Requirements for scintillator materials on the other hand are high light output, high density and effective atomic number, fast scintillation rise and decay time, good energy resolution, low non-proportionality, peak emission wavelength matching the spectral sensitivity of the photo-detector, low cost, non hygroscopic, ruggedness, and no intrinsic radiation (Kamada et al., 2008, Swiderski et al., 2009, Yeom et al., 2013, Kimble et al., 2002, ter Weele et al., 2015, Pepin et al., 2007, Blahuta et al., 2013). In addition to the choice of material, there are other factors which influence the performance of the detector module. This includes the geometry and surface treatment of the crystal, the reflector type, optical coupling of the photo-detector to the crystal, and the performance of the photo-detector at the desired bias voltage and threshold (Stewart et al., 2016, Auffray et al., 2013, Gundacker et al., 2012, 2016, Liu et al., 2016, Grodzicka et al., 2014). However, not all of these parameters are independent from each other and the performance of the detector module is not completely predictable from the characteristics of its individual components.

Among currently available scintillator materials, cerium doped lutetium silicates based scintillation crystals like Lu_2SiO_5 (LSO) and $Lu_{(2-x)}Y_xSiO_5$ (LYSO) have become the most commonly used scintillators in PET detector design studies since the early 2000s, as they offer a good trade off among the aforementioned factors (Pepin et al., 2007, Yeom et al., 2013, Blahuta et al., 2013, ter Weele et al., 2015, Iwanowska et al., 2013). The first growth of LYSO crystals was started in 1997 to reduce the growth temperature and the material cost of LSO, by replacing some of the lutetium by yttrium atoms (Kimble et al., 2002). Different compositions of the LYSO crystal varying in the concentration ratio of lutetium were characterized and compared to LSO (Kimble et al., 2002, Pepin et al., 2004, 2007). Furthermore, many research groups have reported on potential improvements, that can be obtained by co-doping of these crystals with calcium and magnesium cations (Blahuta et al., 2013, van Dam et al., 2013, Nemallapudi et al., 2015, ter Weele et al., 2015, Gundacker et al., 2012). Cerium doped LYSO crystals coupled to SiPMs have been widely incorporated into PET systems recently and promising results have been reported (Schug et al., 2015, Mackewn et al.,

2015, González et al., 2016, Goertzen et al., 2016, Yamamoto et al., 2016, Ko et al., 2016a, Marcinkowski et al., 2016). However, it is important to note that the intrinsic radiation from ^{176}Lu results in gamma ray emissions at 88, 202, and 307 keV, which contribute to a significant radiation background as the number of crystals increase in the PET scanner.

In 2012, cerium doped $Gd_3(Al_{(1-x)}Ga_x)_5O_{12}$ (GAGG) single crystals, grown by the Czochralski (Cz) method, were introduced and the first results were obtained by substituting part of the aluminum site with gallium with a concentration factor of 3.0 (x=3/5) (Kamada et al., 2012). Later it was shown that light yield, energy resolution, and decay time of Ce:GAGG depend on the aluminum-gallium ratio (Kamada et al., 2014, Kurosawa et al., 2014). Coupling Ce:GAGG crystals with gallium concentration factors of 2, 2.4, 2.7, and 3.0 to avalanche photo diodes (APDs) from Hamamatsu showed that the maximum light yield was obtained with a gallium concentration factor of 2.7, energy resolution improved with decreasing the gallium concentration, and shorter decay time was achieved with increasing the gallium concentration (Kamada et al., 2014). Additionally, since Ga_2O_3 is more expensive than Al_2O_3, maximum substitution of gallium with aluminum reduces the cost, while keeping the effective atomic number and stopping power similar (Kurosawa et al., 2014). Promising scintillation properties of these relatively new crystals such as very high light yield, good intrinsic energy resolution, high density and stopping power, being non hygroscopic, and having no self radiation, makes them attractive candidates for applications in PET, SPECT, and gamma spectroscopy (Kamada et al., 2012, Yeom et al., 2013). Furthermore, gadolinium oxide and gallium oxide which are the main components of GAGG crystals are less expensive compared to lutetium oxide used in crystals such as LSO and LYSO (Yeom et al., 2013). However, due to the paramagnetic characteristics of gadolinium, Ce:GAGG is not suitable for use in magnetic resonance imaging (MRI) compatible PET inserts (Stewart et al., 2016).

Praseodymium (Pr^{3+}) doped lutetium aluminum garnet crystals, $Lu_3Al_5O_{12}$ (LuAG), have also become of interest during the past years due to their high density, fast scintillation decay time, good intrinsic energy resolution, and low light yield non-proportionality (Drozdowski et al., 2008, Kamada et al., 2008, Swiderski et al., 2009, Stewart et al., 2016). Compared to Ce:$LaBr_3$ crystals, Pr:LuAG offers a shorter decay time, higher density, and does not require hermetic encapsulation, but its peak emission wavelength around 320 nm does not match the absorption spectra of most

photomultiplier tubes (PMTs) and SiPMs (Stewart et al., 2016). Pr:LuAG single crystals can be grown by the Czochralski method (Kamada et al., 2008), and due to their extremely fast decay time they can be good candidates to be used for Positron Emission Mammograph (PEM) and Time-of-Flight (TOF) PET (Kamada et al., 2008, Stewart et al., 2016). One of the main limitations of Pr:LuAG is its light output, which is relatively low compared to Ce:GAGG or Ce:LYSO, but it is still three times higher than BGO crystals (Kamada et al., 2008). Furthermore, due to the presence of ^{176}Lu, a relatively high intrinsic count rate of 210 Bq cm^{-3} has been observed with this crystal (Drozdowski et al., 2008). Cerium doped LuAG crystals have also been investigated by many groups (Swiderski et al., 2009, Kamada et al., 2012, Auffray et al., 2013). It was shown that the intrinsic energy resolution of the crystal is improved by changing the dopant from cerium to praseodymium, making the energy resolution of Pr:LuAG superior amongst dense scintillators with large effective atomic numbers (Swiderski et al., 2009). On the other hand, although Ce:LuAG does not have an unfavorable emission wavelength in ultra-violet region like Pr:LuAG, it has a decay time three times longer that Pr:LuAG (Auffray et al., 2013).

Performance of different SiPMs coupled to LYSO, GAGG, and LuAG scintillators has been investigated by many groups during the past years (Iwanowska et al., 2013, Schaart et al., 2009, Gundacker et al., 2016, Ferri et al., 2014, 2016, Piemonte et al., 2013, Schneider et al., 2014, Stewart et al., 2016, Yeom et al., 2013, Auffray et al., 2013, Gundacker et al., 2012). In this work, SiPMs with an active area size of 1.2×1.2 mm^2 and different micro-cell sizes have been characterized for the first time, which are particularly of interest for high resolution small animal PET scanners. Furthermore, the performance of the SiPMs has been specifically evaluated with five scintillator crystals regarding their application in PET.

3.2 Materials and methods

3.2.1 Detector modules

Five types of SiPMs from the KETEK PM11 series, with an active area size of 1.2 × 1.2 mm^2 and a peak photon detection efficiency (PDE) around 430 nm were characterized in this study. The SiPMs were produced in 2014 with two production technologies and they differed in the micro-cell size, varying from 25 μm to 100 μm. Three of the SiPM models were produced with optical trench isolation technology to minimize the crosstalk between the micro-cells, while the other two were produced by

the standard technology with no trench. The active area of the SiPMs and the wire bonds were covered by a 300 μm protection layer of epoxy and they all had a surface-mount device (SMD) package size of $2.45 \times 1.95 \times 1.8$ mm^3. From each SiPM model two samples were available and tested. The SiPM models and their corresponding micro-cell pitch size, fill factor (FF), and the production technology are listed in table 3.1. The micro-cell size in SiPMs is an important design parameter which directly affects the gain, dynamic range, recovery time, correlated noise probability, and PDE of the detector (Piemonte et al., 2013). Each micro-cell in an SiPM consists of the active area of the Geiger-mode avalanche photo diode surrounded by a quenching resistor and the wiring for routing the bias voltage to the micro-cells. As the micro-cell pitch decreases, it becomes more difficult to keep the fill factor high due to the restrictions in the size of these passive components (Ferri et al., 2014, Piemonte et al., 2013).

Table 3.1: Micro-cell geometry, production technology, and peak PDE of the five characterized SiPMs, provided by KETEK GmbH.

SiPM Model	PM1125NT	PM1150NT	PM1150T	PM1175T	PM11100T
Cell Pitch (μm)	25	50	50	75	100
Number of Cells	2304	576	576	256	144
Fill Factor (%)	48	70	63	72	80
Production Technology	Standard	Standard	Trench	Trench	Trench
Peak PDE (%)*	30	42	38	45	51

*At 430 nm, measured at 5.0 V over-voltage.

In order to assess the energy and time resolution of SiPMs as detector modules for PET, the SiPMs were coupled to five different scintillation crystals. Two Ce:LYSO crystals from two producers, two Ce:GAGG crystals with different gallium concentrations, and one Pr:LuAG crystal were used for comparison. From each crystal type two samples were available and tested. The physical properties of the five crystals, provided by their producers, are listed in table 3.2. All crystals had a geometry of $1.5 \times 1.5 \times 6$ mm^3, polished on all sides, and were wrapped in several layers of white PTFE reflector tape. Although longer crystals are usually used in PET detector designs, the 6 mm length was used to minimize the effect of light propagation in the crystal on its timing performance (Ferri et al., 2014). Furthermore, this length of crystals can be employed in dual layer or phoswich design configurations of PET detectors.

Table 3.2: The physical properties of the five scintillation crystals used, taken from the datasheets provided by their producers.

Crystal Reference Name	H_LYSO	LYSO	GAGG_3.0	GAGG_2.4	LuAG
Producer	Hilger*	C&A**	C&A	C&A	C&A
Crystal Composition	Ce:LYSO	Ce:LYSO	Ce:GAGG (Ga 3.0)	Ce:GAGG (Ga 2.4)	Pr:LuAG
Decay Time (ns)	40	40	97 (80%) 353 (20%)	138 (71 %) 649 (29 %)	22 (60%) 419 (40%)
Density (g/cm^3)	7.1	7.2	6.7	6.6	6.7
Light Yield ($Photons/MeV$)	32000	30000	55000	46000	18000
Peak Wavelength (nm)	420	420	520	510	310

*Hilger Crystals, Unit R1 Westwood Estate, Margate, Kent, CT9 4JL, England.
**C&A Corporation, 6-6-40,Aza-Aoba, Aramaki, Aoba-ku, Sendai, 980-8579.

3.2.2 Photodetector characterization

3.2.2.1 Current-voltage characteristic measurements

Silicon photomultipliers are avalanche photodiodes which are operated in Geiger mode. Each Geiger mode micro-cell of the SiPM is passively quenched by a resistor placed in series. The elementary structure of the SiPMs can be modeled as an electrical circuit (Cova et al., 1996, Corsi et al., 2007, Seifert et al., 2009). The main components of this model are the quenching resistor R_q, the parasitic stray capacitance C_q in parallel to R_q, the photodiode capacitance C_d, and the parasitic capacitance C_g which is due to the routing of the bias voltage to the micro-cells. After an avalanche in a micro-cell, the voltage of the photodiode drops down to the breakdown voltage and then it recovers to the nominal operating voltage with a time constant (Vacheret et al., 2011). This time constant is referred to as micro-cell recovery time τ_r and can be calculated from $R_q \cdot (C_q + C_d)$ (Cova et al., 1996, Corsi et al., 2006). To measure the SiPM recovery time, SiPMs were saturated using a Hamamatsu PLP-10-040 pico-second light pulser connected to a C10196 controller. The measurements were performed at five different bias voltages and repeated five times at each bias voltage. The mean recovery time was then calculated from exponential fitting on the long tail of the SiPM signals (Schneider et al., 2014).

The value R_q of the quenching resistor can be obtained from the current-voltage (I-V) characteristic curves of the SiPMs biased in the forward direction, in the region where the quenching resistor becomes dominant and the current changes linearly with the bias voltage (Piemonte et al., 2007). Assuming that R_q is the same for all micro-cells and the total number of micro-cells N_{cells} is known for all devices, it is possible to

extract the R_q from the slope of the linear region, which is approximately equal to R_q/N_{cells} (Piemonte et al., 2007, Corsi et al., 2007). This measurement was performed for all the SiPMs and the total micro-cell capacitance $C_{cell} = C_d + C_q$ was calculated from the recovery time and the quenching resistance consequently to be used for energy nonlinearity correction.

Additionally, the breakdown voltage and the operating range of the SiPMs were extracted from the reverse I-V curve. The breakdown voltage was defined by the bias voltage at which the second derivative of the logarithmic I-V curve reaches its maximum and the operating range was defined by the constant region between two local maxima of the first derivative of the logarithmic I-V curve (Schneider et al., 2014).

I-V measurement sweeps were performed with a Keithley 4200-SCS semiconductor characterization system controlled by a LabVIEW program. The measurements were carried out in dark condition for all the SiPMs in a temperature controlled light tight Faraday cage at 22°C. The I-V characteristic curves were obtained by biasing the SiPMs in forward and reverse mode and measuring the dark current as a function of the bias voltage. The voltage was driven from 10 V to 40 V in steps of 0.1 V in reverse mode, and from 0 V to 4 V in steps of 0.05 V in forward mode. The hold time for each current measurement was 0.1 s.

3.2.2.2 Breakdown voltage temperature dependency

Another method to measure the breakdown voltage of SiPMs is measuring the relative gain. Relative gain can be calculated from the distance between two consecutive peaks in the single photo-electron spectrum at a certain bias voltage (Schneider et al., 2014). Since the relative gain is proportional to over-voltage, the breakdown voltage can be calculated by linear extrapolation to a relative gain of zero (Schneider et al., 2014, Auffray et al., 2015).

To calculate the breakdown temperature dependency of the SiPMs, the single photo-electron spectra were obtained by using a blue emitting LED in a temperature controlled dark box at temperatures of 22°C and -2°C. The SiPMs were connected to a Photonique preamplifier with a gain of 30 and the amplified signal was processed by NIM electronics. The SiPM bias voltages were supplied and monitored by a Keithley 6487 picoammeter/voltage source. The single photo-electron spectra were obtained at different bias voltages for each SiPM by using an integrating analog-to-digital converter (ADC) controlled by a LabVIEW program.

3.2.2.3 Dark count rate

When a photo-electron is generated by the thermal excitation or the tunneling effect, it triggers an avalanche breakdown. This event is referred to as a dark count (Auffray et al., 2015). Dark count rate of the SiPMs can be measured by obtaining the single photo-electron spectra in absence of light (Eckert et al., 2010, Auffray et al., 2015). Single photo-electron spectra can be obtained with light pulses or in dark conditions. The spectrum is a charge histogram containing several peaks, where each peak corresponds to the charge resulting from a certain number of cells being fired (Eckert et al., 2010). The peaks are consequently called by the number of fired cells or photoelectrons (pe) and have a Poisson distribution. Although the spectrum contains also the events resulting from after-pulsing and optical crosstalk, the first peak which is referred to as the pedestal peak is unaffected by these two phenomena, as the events in this peak had a charge less than a single cell charge. Therefore, the number of counts in the pedestal peak can be used for dark count rate calculation.

Single photo-electron spectra of all SiPMs were obtained in dark conditions at room temperature and the temperature was monitored during the measurements. The SiPMs were connected to a Photonique preamplifier with a relative gain of 30 and the amplified signal was processed by NIM electronics. A Keithley 6487 picoammeter/voltage source was used for bias voltage supply and dark current measurement. The single photo-electron spectra were obtained at different bias voltages for each SiPM by using an integrating analog-to-digital converter (ADC) controlled by a LabVIEW program. Randomly triggered 100 ns long gates served as integration window for the ADC. Dark count rate at room temperature T_m was then defined by:

$$DCR(T_m) = \frac{n_{pe}}{\Delta t_{gate} \times A_{SiPM}} \tag{3.1}$$

where A_{SiPM} is the active area size of the SiPM and n_{pe} is the average number of Poisson distributed dark count events detected in the gating interval Δt_{gate}. The number of dark counts was calculated from the Poisson probability density function for the events in the pedestal peak, shown in equation 3.2, where $P(0, n_{pe})$ is the probability of detecting zero photons by a Poisson distribution with a mean value of n_{pe} (Eckert et al., 2010).

$$P(0, n_{pe}) = \exp^{-n_{pe}} \tag{3.2}$$

This probability can be calculated from the ratio of the number of events in the pedestal peak, N_{ped}, to the total number of events, N_{total}. Subsequently the DCR can be calculated using:

$$\exp^{-n_{pe}} = \frac{N_{ped}}{N_{total}} \Rightarrow n_{pe} = -\ln \frac{N_{ped}}{N_{total}} \tag{3.3}$$

Since thermally generated free carriers are reduced by a factor 2 by every 8 degree drop in the temperature (Renker and Lorenz, 2009), DCR was estimated at temperature $T = 20°C$, based on the calculated DCR value at measurement temperature T_m as shown in equation 3.4.

$$DCR(T) = DCR(T_m) \cdot 0.5^{\frac{T_m - T}{8}} \tag{3.4}$$

3.2.2.4 Correlated noise probability

Using the same measurement setup described for the DCR calculation, single photoelectron spectra were obtained for all SiPMs using a triggering threshold of 0.5 pe at -2°C in dark conditions. Gate lengths of 60 ns to 100 ns were used for different SiPMs. Since the probability of having two dark counts in these gate lengths for KETEK SiPMs is below 1% at this temperature, the events with a charge corresponding to more than 1 cell firing are mainly due to correlated noise, including optical crosstalk and afterpulsing (Auffray et al., 2015). Correlated noise can contribute largely to limiting the maximum operating voltage of the SiPMs and consequently the achievable PDE (Ferri et al., 2016). Therefore, the probability for correlated noise was estimated from the ratio of the counts with a charge higher than 1.5 pe to the total number of counts in the spectrum (Auffray et al., 2015).

3.2.3 Detector module characterization

To evaluate the performance of the scintillation crystals and SiPMs as detector modules for PET, the crystals were coupled to SiPMs using Dow Corning 1-2577 conformal coating with a refractive index of 1.40. Each detector module was then placed on a circuit board in a light tight box, where the SiPM output signal was split into two branches. The first branch was directly connected to a LeCroy WaveRunner 610Zi digital oscilloscope, terminated with 50 Ω, for energy resolution measurements. The second branch was amplified with a relative gain of ∼10 by a Photonique AMP-0611

preamplifier and was then routed to the oscilloscope for coincidence timing measurements. The bias voltage of the SiPMs was supplied by an iseg EHS-F-005X high precision power supply, through the circuit board. Measurement of the timestamps, signal integration, and histogram plotting were done digitally on the oscilloscope and the generated histograms were analyzed subsequently offline. The SiPM signal was sampled on the oscilloscope with a sampling rate of 10 GS s^{-1}. All measurements were performed at room temperature.

3.2.3.1 Energy resolution

Energy resolution measurements were performed using a ^{22}Na point source with an activity of 3.3 MBq at different bias voltages for all detector modules. Since there is a limited number of cells which can fire in an SiPM, two or more photons reaching a cell can produce exactly the same signal as one photon (Renker, 2009). This results in a saturation effect in the SiPM response, especially with high light intensities, which has to be corrected when the energy resolution is being calculated. This is usually done by using different radioactive gamma emitter sources and fitting an exponential function on the measured positions of different emission peaks in the energy spectra. However, this can be very time consuming, since all the measurements must be repeated at each bias voltage with different radioactive sources. A simpler estimation for correcting the energy resolution is performed by estimating the number of generated photons based on the measurement of two emission peaks in the energy spectra. This can be done either by using the two energy peaks from ^{22}Na or using a second gamma emitter source like ^{137}Cs with an emission peak at 662 keV. However, there are limitations for each method which lead to errors in the correction. Due to the saturation effect, the second energy peak from ^{22}Na, located at 1274.5 keV is not clearly visible for many of the detectors under study. Correcting the energy spectra using the 511 keV peak from ^{22}Na and the 662 keV peak from ^{137}Cs on the other hand results in an overcorrection of the energy spectra, where 1274.5 keV peak from ^{22}Na is clearly mispositioned at higher energies. Due to the proximity of the two peaks, this correction method is less precise to be used over large energy ranges. Corrected energy resolution values obtained by this method were up to 10% worse than the results obtained by using the two peaks from ^{22}Na. Therefore, all measurements were repeated for all the detector modules using a ^{137}Cs point source with 2 MBq activity to be able to confirm the validity of the comparison results using both methods. To avoid the effect of optical coupling

on changing the number of photons reaching the sensor, the measurements with both point sources were performed successively for the same SiPM and crystal.

The energy resolution correction was performed with the assumption of the number of photons in a scintillation pulse, $N_{photons}$, being proportional to the deposited energy in the crystal. The number of fired cells in the SiPM, N_{fired}, can be written as shown in equation 3.5, as a function of the number of photons in the pulse (Renker, 2009):

$$N_{fired} = N_{total} \cdot (1 - \exp(-N_{photons} \cdot PDE/N_{total})) \tag{3.5}$$

where PDE is the photon detection efficiency of the SiPM and N_{total} is the total number of cells which could fire. The latter could become significantly higher than the total number of cells in the SiPM, when the cell recovery time is close to the decay time of the scintillator. The energy spectrum on the oscilloscope is obtained by integrating the signal in time Δt, which can be written as:

$$A = \int_{\Delta t} U \cdot dt = \int_{\Delta t} R_T \cdot I \cdot dt = R_T \cdot \int_{\Delta t} I \cdot dt = R_T \cdot Q = R_T \cdot N_{fired} \cdot Q_{cell} \tag{3.6}$$

where A $(V.s)$ is the measured integrated value corresponding to the deposited energy, R_T is the 50Ω terminal resistance, and Q_{cell} is the single cell charge which can be calculated from equation 3.7 based on cell capacitance C_{cell} and over-voltage U_{OV} (Seifert et al., 2009).

$$Q_{cell} \approx C_{cell} \cdot U_{OV} = (C_d + C_q) \cdot U_{OV} \tag{3.7}$$

Consequently, equation 3.5 can be used to calculate the number of photons as following:

$$N_{photons} = \frac{-N_{total}}{PDE} \cdot (\ln(1 - A/(R_T \cdot Q_{cell} \cdot N_{total}))) \tag{3.8}$$

If A_1 and A_2 are the two measured emission peak positions in the energy spectra for gamma ray energies of E_1 and E_2 respectively, equation 3.8 can be used for saturation correction as following:

$$\frac{N_{photons(1)}}{N_{photons(2)}} = \frac{\ln(1 - A_1/(R_T \cdot Q_{cell} \cdot N_{total}))}{\ln(1 - A_2/(R_T \cdot Q_{cell} \cdot N_{total}))} = \frac{E_1[keV]}{E_2[keV]} \tag{3.9}$$

from which N_{total} can be calculated and the energy spectrum can be corrected by calculating the number of photons for each measurement point A, based on equation 3.8 as following:

$$A_{corr} = \frac{511}{N_{photon(511)}} \cdot N_{photons} \tag{3.10}$$

Since the PDE has a linear effect on the energy resolution correction, a PDE of 1 was assumed in the correction process for all the SiPMs.

After applying the correction, the energy spectra were analyzed in MATLAB and a Gaussian fitting was applied on the 511 keV photo-peak together with a Compton background correction. The background correction was performed by calculating a linear fit between the two local minima of the photo-peak and subtracting it from the photo-peak spectrum.

3.2.3.2 Coincidence time resolution

Coincidence measurements were performed at room temperature for at least six different over-voltages for each SiPM, covering the complete operating range of each detector. Time resolution in scintillation detectors is a function of the trigger threshold level and the optimum time resolution is generally not achieved by the first photo-electron trigger (Seifert et al., 2012). Therefore, for comparison of different detector modules, the coincidence timing measurements were performed with different triggering thresholds, starting from the baseline, in steps of 5 mV to find the best achievable CTR for each detector module. The coincidence time histograms were acquired with the oscilloscope and saved for offline analysis. The trigger level for each channel was adjusted individually according to its energy spectrum to discard the Compton scattered events in the coincidence timing measurements. Fityk open-source curve-fitting software was used later for Gaussian fitting on the histograms and coincidence time resolution was defined as FWHM of the Gaussian fit. The intrinsic time resolution of the measurement setup was measured with one PM1150NT device coupled to Ce:LYSO and splitting the signal in two (Gundacker et al., 2016). A CTR of ∼30 ps was obtained at the lowest applied threshold of 5 mV and it was reduced to ∼8 ps at higher thresholds. Therefore, the CTR values were not corrected for the intrinsic time resolution of the setup individually, as the effects were negligible.

3.3 Results and discussion

3.3.1 Photodetector characterization

Reverse I-V characteristic curves and their first derivatives are shown for PM11 series of SiPMs in figure 3.1a and 3.1b, respectively. The breakdown voltage and the operating range of SiPMs calculated from the reverse I-V curves are summarized in table 3.3. All SiPMs produced with the trench technology had a breakdown voltage around 25.0 V, while the SiPMs of the standard technology had slightly higher breakdown voltages around 27.7 V. These values were consistent with the breakdown voltages at the same temperature obtained from the relative gain calculation method. All SiPMs showed a stable performance with changes of temperature, resulting in a breakdown voltage temperature coefficient below 22 mV K^{-1} as shown in table 3.3. PM1125NT SiPMs offered the largest operating range of about 12 V and the operating range of the SiPMs was limited by increasing the cell size. Between the two SiPMs with 50 μm cell pitch, PM1150T with the trench technology had a larger operating range (9.1 V) compared to PM1150NT (6.1 V).

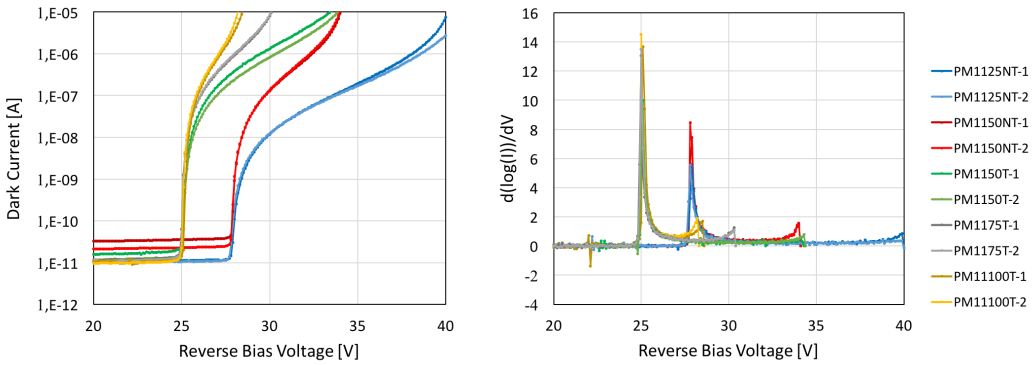

(a) **(b)**

Figure 3.1: (a) Reverse I-V characteristic curves and (b) the first derivate of the logarithmic I-V curve of the PM11 series of SiPMs. Two samples from each SiPM model are marked with corresponding suffixes.

Figure 3.2a shows the forward I-V characteristic curves of the SiPMs in a logarithmic scale, from which the value of the quenching resistor R_q was calculated for each SiPM circuit model and listed in table 3.3, along with the mean recovery time and cell capacitance. The smallest quenching resistor value among all devices was observed for the PM1150NT SiPMs, with ∼519 kΩ. Comparing the fill factor of the SiPMs listed in table 3.1 and the quenching resistor values in table 3.3 showed no correlation

Table 3.3: SiPM characteristics obtained from I-V curves and relative gain measurements at room temperature of 22°C. Two of the SiPMs were not available for the measurements of breakdown voltage temperature coefficient (V_{BD} Temp. Coeff.). The values of the quenching resistor (R_q), cell capacitance (C_d+C_q), and cell recovery time (τ_r) are shown for all SiPMs. The digits after "PM11" in the SiPM model represent the micro-cell size of the SiPMs in μm.

SiPM Model	Breakdown Voltage (V)	Operating Range (V)	V_{BD} Temp. Coeff. (mV K^{-1})	R_q ($k\Omega$)	$C_d + C_q$ (fF)	τ_r (ns)
PM1125NT-1	27.7	27.9 – 39.9	21.2	717.8	21.7	37.9
PM1125NT-2	27.7	27.8 – 39.9	20.1	711.1	21.7	37.1
PM1150NT-1	27.7	27.9 – 34.0	14.9	518.9	272.8	129.5
PM1150NT-2	27.7	27.8 – 34.0	-	533.3	258.8	132.2
PM1150T-1	24.9	25.1 – 34.2	16.0	800.0	238.9	203.9
PM1150T-2	24.9	25.1 – 34.3	-	685.7	233.9	180.7
PM1175T-1	24.9	25.0 – 30.3	11.0	914.3	702.4	564.4
PM1175T-2	24.9	25.0 – 30.3	14.0	825.8	592.2	523.1
PM11100T-1	25.0	25.1 – 28.5	13.9	576.0	1136.0	686.7
PM11100T-2	24.9	25.0 – 28.2	14.5	553.8	1212.1	657.8

between the micro-cell passive area of the SiPMs with the quenching resistors value. Furthermore, in a previous study on 3×3 mm^2 KETEK SiPMs produced with the trench technology, values in the range of 500 kΩ to 540 kΩ were obtained for devices with 50 – 70 μm cell pitches (Schneider et al., 2014).

The cell capacitance on the other hand linearly increased with micro-cell active area size. This can be explained by the increase in effective area of the P-N-junction for smaller micro-cells, which have a smaller fill factor. However, comparing the results obtained for PM1150NT and PM1150T devices shows a slightly higher cell capacitance for the device with the trench technology even though it has a lower fill factor.

Among all devices PM1125NT showed the shortest recovery time of ∼37 ns and the recovery time increased with the increase of the cell size. Comparing PM1150NT SiPMs to PM1150T, the SiPMs using the trench technology had a ∼40% longer recovery time. This results in a crucial difference in pulse amplitude and number of fired cells in the SiPM, as the number of photons increase and subsequently it influences the degree of saturation.

Figure 3.3a shows the DCR of the SiPMs, calculated for temperature of 20°C, at different bias voltages. Higher DCR was observed for the devices with larger micro-cells. All SiPMs had a DCR below 1.3 MHz mm^{-2} throughout their full operating range. Operating the devices at lower over-voltages could decrease the DCR to below 200 kHz mm^{-2} for all devices. DCR increased faster with over-voltage increase for

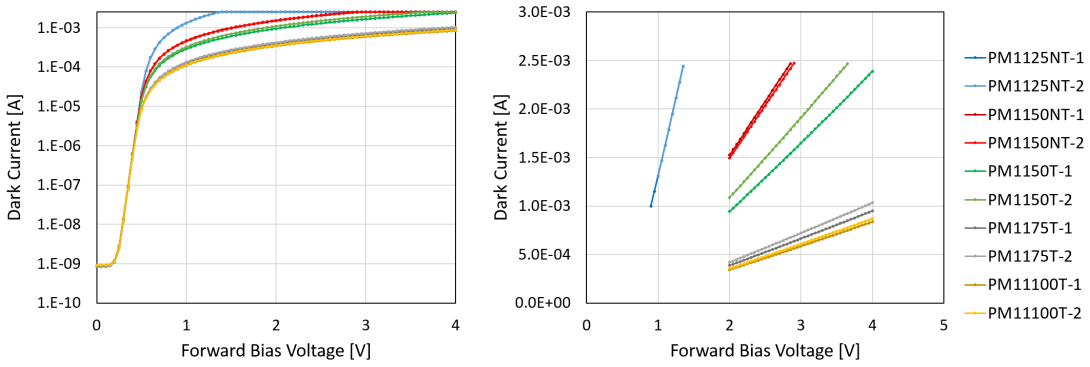

(a) **(b)**

Figure 3.2: (a) Forward I-V characteristic curves and (b) the linear fit on the region where the quenching resistor becomes dominant for the PM11 series SiPMs. Two samples from each SiPM model are marked with corresponding suffixes.

SiPMs with larger micro-cells. This is in accordance with figure 3.1b and table 3.3, where the second strong increase of the differential I-V curve limits the operating range of these devices to lower over-voltages.

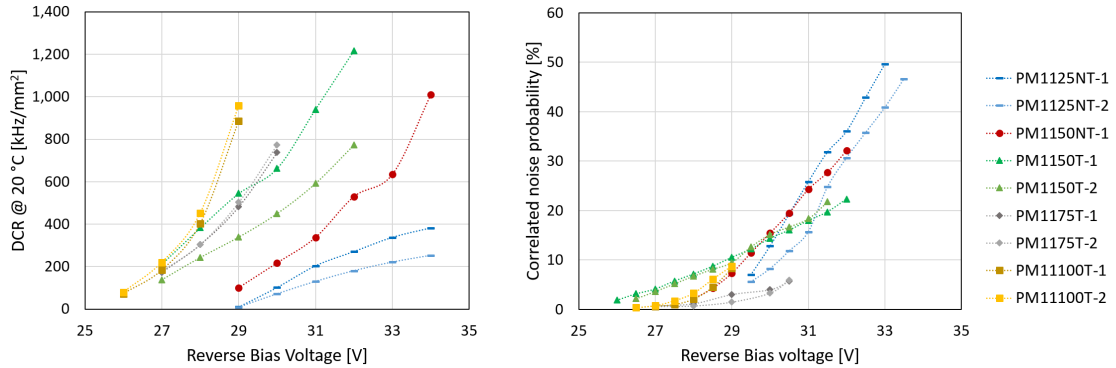

(a) **(b)**

Figure 3.3: (a) Dark count rate of PM11 series SiPMs at 20°C and (b) correlated noise probability of PM11 series SiPMs measured at -2°C for the PM11 series SiPMs. One sample from PM1150NT series was not available for testing.

Correlated noise probability of PM11 series SiPMs measured at -2°C is shown in figure 3.3b. The SiPMs produced with the trench technology show lower correlated noise probabilities with slower increase rate with over-voltage compared to the non-trench devices. This is mainly due to lower cross talk resulting from the trenches between the micro-cells. The remaining cross-talk is expected to be mainly a result of the optical

photons which are reflected from the front silicon-epoxy or epoxy-air interfaces to the neighboring micro-cells and triggering them.

3.3.2 Detector module characterization

3.3.2.1 Energy resolution

Average and standard deviation of energy resolution measured over the complete operating range of each detector module are shown in table 3.4. Furthermore, the best energy resolution values achieved with each combination of scintillation crystals and SiPMs are shown in table 3.5, before and after saturation correction. The depicted results were corrected for nonlinear saturation effect using the two energy peaks from ^{22}Na. A comparison of the energy resolution results before and after the saturation correction shows the level of saturation for different detector modules.

Table 3.4: Average and standard deviation of energy resolution FWHM [%] at 511 keV measured for each combination of scintillation crystals and SiPMs measured over the complete range of their operating over-voltage range, after nonlinearity saturation correction performed using the two energy peaks from ^{22}Na. The digits after "PM11" in the SiPM model represent the micro-cell size of the SiPMs in μm.

Average and standard deviation of energy resolution (%)

Detector Module	H_LYSO	LYSO	GAGG_3.0	GAGG_2.4	LuAG
PM1125NT-1	16.5±0.5	15.8±0.7	13.6±0.3	12.8±0.7	23.3±2.7
PM1125NT-2	16.9±0.9	15.9±0.6	14.6±0.5	13.6±0.5	21.9±2.1
PM1150NT-1	16.2±2.5	15.2±0.7	12.6±0.7	13.3±1.2	19.4±0.9
PM1150NT-2	16.1±2.2	15.4±1.6	12.7±0.8	12.5±0.8	19.3±0.9
PM1150T-1	17.6±2.1	18.7±1.9	12.7±1.5	13.1±1.9	20.0±0.9
PM1150T-2	19.0±2.7	18.6±1.7	13.1±1.2	12.8±1.4	19.3±0.6
PM1175T-1	17.8±3.2	13.3±2.5	8.4±0.5	12.1±2.0	16.2±1.4
PM1175T-2	12.5±1.3	15.2±2.5	10.0±1.4	13.5±0.8	17.4±1.0
PM11100T-1	15.4±3.4	15.8±3.3	9.8±0.9	11.8±1.6	16.2±1.6
PM11100T-2	16.3±3.6	14.5±2.1	12.4±3.2	13.2±0.9	16.0±1.8

Correcting the energy spectra using the 511 keV peak from ^{22}Na and the 662 keV peak from ^{137}Cs was not possible for 75 μm and 100 μm devices, since the SiPMs were highly saturated and the error in positioning the two energy peaks was larger than the distance of the two peaks in the two energy spectra. With 25 μm devices, the corrected energy resolution results were very close for the two methods. With 50 μm devices on the other hand, the energy spectra were highly elongated and over-corrected. Therefore, in order to compare the different detector modules fairly, the energy spectra

Table 3.5: The best energy resolution FWHM (%) at 511 keV achieved for each combination of scintillation crystals and SiPMs measured over the complete range of their operating over-voltage range. The results are corrected for nonlinear saturation effect using the two energy peaks from ^{22}Na. The values before applying the correction are shown in parentheses. The digits after "PM11" in the SiPM model represent the micro-cell size of the SiPMs in μm.

The best energy resolution values (%) **corrected** | (before correction)

Detector Module	H_LYSO	LYSO	GAGG_3.0	GAGG_2.4	LuAG
PM1125NT-1	**15.7** | (13.5)	**14.4** | (12.4)	**13.1** | (10.4)	**11.9** | (9.7)	**20.0** | (19.5)
PM1125NT-2	**16.2** | (13.0)	**15.1** | (12.1)	**14.1** | (12.1)	**12.7** | (12.0)	**18.7** | (17.6)
PM1150NT-1	**13.7** | (6.1)	**14.5** | (6.8)	**12.0** | (7.3)	**11.5** | (7.6)	**18.4** | (12.0)
PM1150NT-2	**14.0** | (5.7)	**13.4** | (6.2)	**11.9** | (7.4)	**11.5** | (7.7)	**17.2** | (14.6)
PM1150T-1	**14.5** | (8.7)	**16.1** | (7.9)	**10.4** | (5.6)	**10.9** | (7.0)	**18.5** | (15.5)
PM1150T-2	**16.9** | (9.7)	**15.3** | (7.3)	**11.9** | (6.9)	**11.0** | (7.1)	**18.5** | (15.6)
PM1175T-1	**14.6** | (10.5)	**10.5** | (7.1)	**7.7** | (5.6)	**10.6** | (8.0)	**14.0** | (11.1)
PM1175T-2	**11.0** | (4.3)	**11.8** | (7.9)	**7.5** | (6.5)	**11.5** | (7.7)	**16.2** | (11.8)
PM11100T-1	**11.1** | (7.6)	**13.0** | (8.7)	**8.6** | (5.5)	**9.9** | (6.8)	**15.1** | (10.9)
PM11100T-2	**12.5** | (7.3)	**12.3** | (8.5)	**9.3** | (6.2)	**12.2** | (7.7)	**14.5** | (11.4)

from the first sample of each SiPM model with different crystals are additionally shown in figure 3.4 for the best achieved corrected values given in table 3.5.

The obtained results can be explained by equation 3.5 and the specification of the SiPMs and the scintillators given in tables 3.1 and 3.2. The SiPM response to a light pulse with a certain number of photons is defined by the number of fired micro-cells. Three main parameters affect the number of fired micro-cells and therefore the energy resolution of the detectors: the number of generated photons which depends on the characteristics of the scintillation crystals, the number of micro-cells in the SiPM, and the PDE of the SiPMs as a function of the wavelength. As the number of SiPM micro-cells coupled to the scintillator and the number of photons increase, the probability of having two or more photons reaching the micro-cell and resulting in a saturation effect increases. On the other hand, PDE of the SiPMs is strongly affected by the fill factor of the micro-cells. Therefore, the two effects resulting from the micro-cell size work contrarily. This can be observed by comparing the energy resolutions obtained with the 25 μm devices to the 50 μm devices. Although the saturation effect for the 25 μm devices is very small and the 1274.5 keV peak is clearly observed in their energy spectra, due to the lower PDE of these devices the energy resolution is slightly worse than the 50 μm devices when the saturation correction is applied.

Among the studied scintillators, Pr:LuAG had considerably lower light yield than the other crystals. Additionally, PDE of the SiPMs is significantly reduced (to below

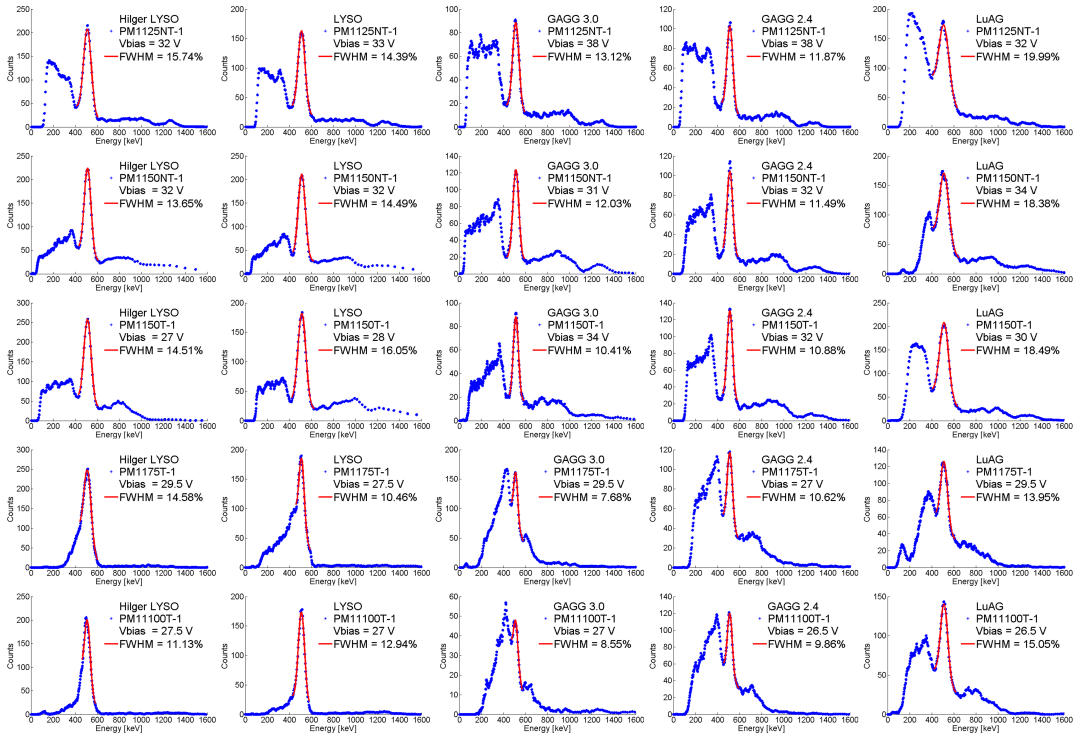

Figure 3.4: Energy spectra of ^{22}Na for the best achieved energy resolution FWHM (%) at 511 keV. Spectra are shown for the first sample of each combination of scintillation crystals and SiPMs, after correcting for nonlinear saturation effect by using the two energy peaks from ^{22}Na.

∼30% of the peak PDE) for the 310 nm wavelength of the photons generated with this crystal. These two effects resulted in a lower number of photons reaching the SiPMs and consequently less saturation nonlinearity effect in the SiPMs. Although Pr:LuAG offers a good intrinsic energy resolution (Drozdowski et al., 2008), the low PDE of the SiPMs at this wavelength resulted in a deterioration of the energy resolution compared to the other investigated crystals. The energy resolutions are in agreement with reported results for larger Pr:LuAG crystals coupled to 3×3 mm^2 SensL SiPMs (Stewart et al., 2016).

The two Ce:GAGG crystals showed the best energy resolution, as expected. The Ce:GAGG crystal with higher concentration of gallium had a higher light yield, but also a slightly higher spectral peak wavelength resulting in a lower PDE for the SiPMs. Additionally, the intrinsic energy resolution of the crystal with lower gallium concentration was better (Kamada et al., 2014). Therefore, the energy resolution of the detector modules were not significantly different between these two crystals.

The two Ce:LYSO crystals from the two different producers showed very similar energy resolution performance with the tested SiPMs and the best results were achieved with the 50 μm devices. The 75 μm and 100 μm were highly saturated due to the high light yield of the crystal and low number of micro-cells and therefore are not suitable for use with Ce:LYSO crystal. The 50 μm devices were also saturated, but the 511 keV photo-peak was clearly distinguishable and energy spectra show that the energy resolution values are slightly over-corrected, but still comparable or even better than the 25 μm devices.

3.3.2.2 Coincidence time resolution

Average and standard deviation of coincidence time resolution (ps) is shown in table 3.6 for each detector module, measured over the complete range of its operating over-voltage range and using the optimal triggering threshold at each bias voltage. Additionally, the best coincidence time resolution achieved with each combination of scintillation crystals and SiPMs is shown in table 3.7. The results were not corrected for the intrinsic coincidence time resolution of the measurement setup. The corresponding time histograms for the best results are shown in figure 3.5.

Table 3.6: Average and standard deviation of coincidence time resolution (ps) measured with each detector module over the complete range of its operating over-voltage range and using the optimal triggering threshold at each bias voltage. The digits after "PM11" in the SiPM model represent the micro-cell size of the SiPMs in μm.

Average and standard deviation of coincidence time resolution (ps)

Detector Module	H_LYSO	LYSO	GAGG_3.0	GAGG_2.4	LuAG
PM1125NT	492±22	451±30	1075±135	3265±418	990±87
PM1150NT	368±59	394±64	944±217	4371±1188	826±79
PM1150T	283±40	316±38	942±118	4408±1786	752±60
PM1175T	301±18	394±26	893±160	-	606±54
PM11100T	456±21	408±56	891±78	-	747±163

It has already been shown that the coincidence time resolution is strongly correlated to the light yield of the crystal, scintillation rise time, and decay time (Auffray et al., 2013). Pr:LuAG has an extremely fast decay component of 22 ns. However, the relatively low light yield and the spectral mismatch of this crystal has resulted in low photon statistics and consequently worse CTR compared to Ce:LYSO. The two characterized Ce:LYSO crystals showed very similar performance in terms of CTR for all the SiPMs and the existing differences are expected to be mainly within the errors of the measurement setup.

Table 3.7: The best coincidence time resolution (ps) achieved with each combination of scintillation crystals and SiPMs, measured over the complete range of their operating over-voltage range and using different triggering thresholds. The digits after "PM11" in the SiPM model represent the micro-cell size of the SiPMs in μm.

The best coincidence time resolution (ps)

Detector Module	H_LYSO	LYSO	GAGG_3.0	GAGG_2.4	LuAG
PM1125NT	459	417	866	2724	888
PM1150NT	308	323	739	2823	739
PM1150T	242	262	817	2879	679
PM1175T	270	369	720	-	527
PM11100T	416	356	807	-	571

The timing performance was very different between the two Ce:GAGG crystals with different gallium concentrations. The crystal with a gallium concentration factor of 3.0 was shown to have higher light yield and faster decay time compared to gallium concentration factor of 2.4 (Kamada et al., 2014). This can be clearly observed in the CTR results, where a strong deterioration is observed for the crystal with lower concentration of gallium. For the combination of this crystal with the 75 μm and 100 μm devices, the time histograms were not showing a Gaussian distribution and the fit results were affected. Therefore, the best values are not included for these two detectors in table 3.7. This could be explained by the limited operating voltage of these devices and their relatively higher dark count rate at high bias voltages as shown in figure 3.3a.

The best timing performance was observed with the 50 μm and 75 μm devices. The low fill factor of the 25 μm has limited the PDE of this device, resulting in a degradation in timing performance. The performance of the 100 μm device on the other hand was limited mainly due to the dark count rate and consequently its limited operating range. Among the three 50 μm and 75 μm devices coupled to Ce:LYSO, PM1150T offered the most stable good timing performance, below 400 ps CTR, over a wide range of operating voltages from 27 V–34 V.

3.4 Conclusion

Among the investigated 1.2×1.2 mm^2 SiPMs, the 25 μm device showed very interesting properties despite its low fill factor and consequently low PDE. It offered the widest operating range of about 12 V and a short recovery time of ∼37 ns. Furthermore, as a result of the large number of micro-cells in its active area, it showed the smallest nonlinear saturation effect among the tested devices. The energy resolution and co-

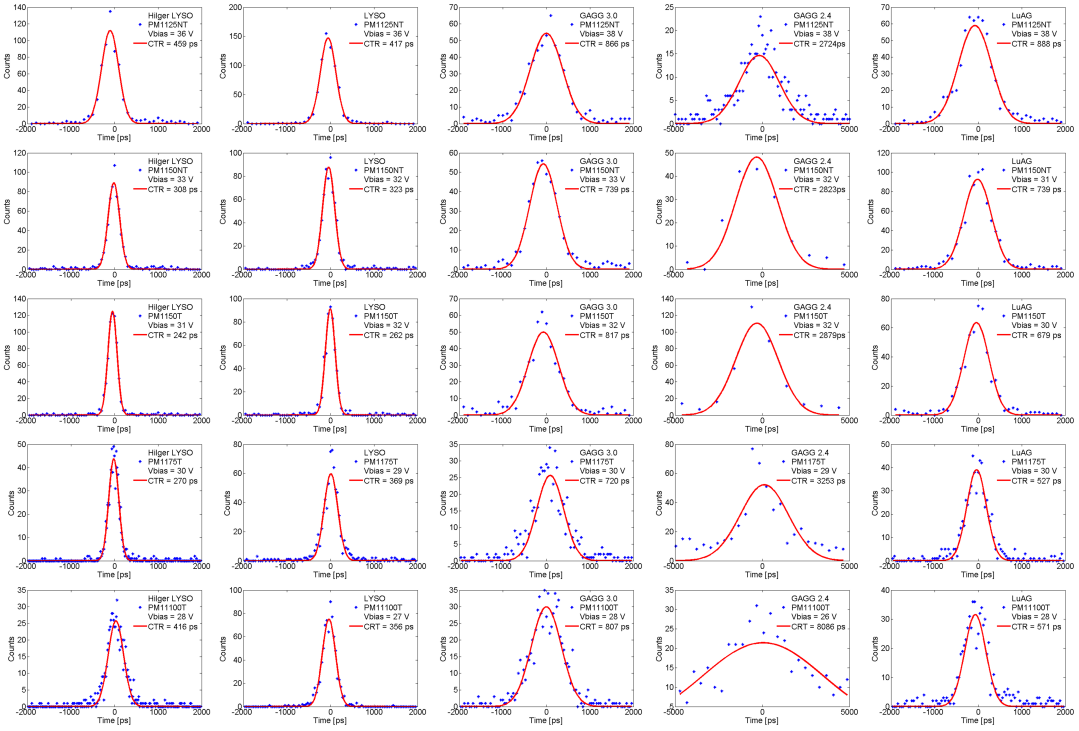

Figure 3.5: Time-difference histograms for the best achieved coincidence time resolution values shown for each combination of scintillation crystals and SiPMs.

incidence time resolution were degraded compared to 50 μm devices due to the low PDE, but still yielding acceptable values for many applications. The lowest DCR and DCR increase slope with changes of over-voltage were achieved with this model, resulting in a DCR below 400 kHz mm^{-2} at 20°C and 22% over-voltage. However, since there are no optical trenches between the micro-cells in the production technology, the correlated noise probability was higher than the other devices, when operated at high over-voltages. The combination of this device with Ce:LYSO crystals and operating around 12% over-voltage resulted in an energy resolution below 17% and a CTR of 500 ps.

The two 50 μm SiPM models showed the best overall performance as PET detector modules, especially when coupled to Ce:LYSO crystals. The best CTR was 242 ps, which was obtained by using the PM1150T devices. A degradation of ∼50 ps was observed with PM1150NT devices, which could be explained by the higher optical crosstalk probability due to the absence of optical trenches. On the other hand, the PM1150NT SiPMs showed better DCR and energy resolution performance, which could be the result of having slightly higher fill factor and PDE. This makes them

better candidates for preclinical PET scanners, where timing performance is not of great importance.

The 75 μm and 100 μm were highly saturated when coupled to the investigated crystals, due to the limited number of cells available in the SiPM active area. Even with Pr:LuAG which has a relatively low light output at a low wavelength of 310 nm, the 1274.5 keV emission peak from ^{22}Na was not clearly visible. Therefore, these devices were found also not suitable for PET applications.

It should be noted that the non-linearity saturation correction method which was applied on the energy spectra provides only an estimation for the energy resolution. There are errors associated with this method resulting from the calculation of the cell capacitance, Gaussian fitting on the energy spectra, and the exponential function estimating the number of photons. However, the differences observed between the performance of different detectors studied in this work are in many cases large enough to make a conclusion based on the estimated results.

Among the tested crystals, Pr:LuAG was found to be not suitable for application with the studied SiPMs, as the other crystals were better candidates for both energy resolution and CTR. This was mainly due the spectral mismatch of this crystal with the investigated SiPMs. The Ce:GAGG crystal with gallium concentration of 2.4 was also found to be not suitable for PET, mainly due to high coincidence time resolution and not showing significant advantage over the other tested Ce:GAGG crystal. Despite the better intrinsic energy resolution of this crystal compared to the Ce:GAGG crystal with gallium concentration of 3.0, the detector energy resolutions were very similar for the two crystals mainly due to their light yield difference. The Ce:GAGG crystal with gallium concentration of 3.0 showed better energy resolution performance compare to Ce:LYSO crystals as expected. However, the improvement in energy resolution was relatively small, especially in case of PM1125NT and PM1150NT devices. The CTR degradation on the contrary was about a factor of 2, compared to Ce:LYSO. Use of GAGG crystals for preclinical PET scanners is worth of study due to their lower price, good energy resolution, and no background activity. Further simulation studies are needed to compare the image quality performance of a PET scanner with improved energy resolution, but degraded CTR when using these crystals.

Chapter 4

PET performance evaluation of MADPET4: a small animal PET insert for a 7 T MRI scanner

This chapter has been published as "Omidvari N, Cabello J, Topping G, Schneider F, Paul S, Schwaiger M & Ziegler S 2017 'PET performance evaluation of MADPET4: a small animal PET insert for a 7 T MRI scanner' Physics in Medicine & Biology 62(22) 8671–8692"[1]

4.1 Introduction

Preclinical positron emission tomography (PET) scanners are widely used for small animal studies for drug development, treatment evaluation, and characterization of human disease models, mainly in the fields of oncology, neurology, and cardiology (Wang et al., 2015a). Mice and rats are used as experimental models in a large variety of applications due to their relatively high genetic similarities to humans, fast breeding cycle, low costs in housing and maintenance, and the availability of well-developed methodologies and expertise for their genetic manipulation (Cherry and Gambhir, 2001). Dedicated small-animal PET scanners that can provide dynamic images with resolution approaching 1 mm are particularly beneficial in modeling many neurological disorders such as Parkinson's disease, Alzheimer's disease, Huntington's disease, stroke, epilepsy, and traumatic brain injury (Virdee et al., 2012).

[1] N. Omidvari conducted the research, authored the manuscript, and performed the Monte-Carlo simulations, data analysis, and the measurements with the PET insert. The PET insert was developed and characterized with the PETsys Electronics readout system by N. Omidvari. The geometrical design of the scanner was studied in a previous work by F. Schneider, by means of Monte-Carlo simulations. He also designed the SiPM PCBs and the 3D-printed structure for holding the crystals and contributed to the design of the 3D-printed light-tight cover and assembly of the detector modules. FBP image reconstruction tasks were performed on the data by J. Cabello. The iterative image reconstruction and the coincidence sorting algorithms were developed based on primary source codes of J. Cabello. They were modified and optimized later by N. Omidvari. Normalization correction, timing calibration, energy calibration, and decay correction were added to the codes by N. Omidvari. MRI scans were performed by G. Topping.

Well-characterized PET radiotracers and the capability of PET in providing dynamic data, together with excellent soft-tissue contrast of magnetic resonance imaging (MRI) and the broad diversity of its acquisition techniques, which can provide contrast sensitive anatomical and functional images, make PET/MRI a powerful hybrid imaging tool. PET/MRI scanners can be built and operated in a consecutive or a simultaneous configuration. In contrast to PET/CT systems, a PET/MRI system can offer an overlaid imaging field-of-view (FOV) for both modalities, where PET and MRI data can be acquired at the same time. The two modalities can offer highly complementary information, as has been shown for a number of applications (Judenhofer and Cherry, 2013, Wehrl et al., 2013). Although many of these studies can be performed with consecutive PET/MRI systems, the simultaneous acquisition offers a valuable gain in accuracy of the co-registration of the two images, especially in studies where MR images are acquired with oblique angle axes or the subject's motion is not negligible (Judenhofer and Cherry, 2013). Furthermore, simultaneous PET/MR functional imaging can be especially beneficial in studies where physiological state of the subject can not be easily reproduced (Judenhofer and Cherry, 2013).

Several preclinical PET scanners have been developed in the past 20 years by different research groups, and some have been made commercially available. Many of these scanners, particularly in the past 10 years, have been PET inserts which were designed for simultaneous use in an MRI system (Judenhofer et al., 2008, Yamamoto et al., 2009, Wu et al., 2009, Mackewn et al., 2010, Yamamoto et al., 2010,b, Kang et al., 2011, Maramraju et al., 2011, Yamamoto et al., 2012, Yoon et al., 2012, Wehrl et al., 2013, España et al., 2014, Mackewn et al., 2015, Schug et al., 2016, Ko et al., 2016a, Goertzen et al., 2016). Since there is a wide range of scanner designs and geometries, comparing the performance of different PET scanners requires a measurement procedure which is replicable and independent of the scanner design. The NEMA NU 4 measurements protocol was published in 2008 by National Electrical Manufacturers Association (NEMA) as a standardized methodology for performance evaluation of small animal PET scanners (NEMA, 2008). The performance of many preclinical PET scanners have been evaluated using the NEMA NU 4 protocol (Kim et al., 2007, Lage et al., 2009, Bergeron et al., 2014, Prasad et al., 2010, Cañadas et al., 2011, Szanda et al., 2011, Wong et al., 2012, Goertzen et al., 2012, Nagy et al., 2013, Gu et al., 2013, Spinks et al., 2014, Wang et al., 2015a, Ko et al., 2016a, Sato et al., 2016). However, most of these scanners are standalone PET, PET/CT, or PET/SPECT/CT scanners.

Among the NEMA NU 4 characterized systems, there has been one commercial consecutive PET/MR system (Nagy et al., 2013) and one PET insert for 7T MRI (Ko et al., 2016a).

The main challenge in design of a PET insert for MRI is to not compromise the image quality of both modalities, given the significant limitations in material choice and component size. The geometrical design of the system in addition to the characteristics of the individual PET detector modules, the read-out electronics, the data processing, and the image reconstruction algorithm contribute to the overall performance of the PET insert. In this work, a small animal PET insert design with a novel detector arrangement is introduced, which uses dual layer individual crystal read-out in combination with silicon photomultiplier (SiPM) technology. The PET performance of the insert was evaluated and compared to other small animal PET scanners using the NEMA NU 4 standard measurements, followed by imaging a hot-rod spatial resolution phantom and two *in vivo* simultaneous PET/MRI scans.

4.2 Materials and methods

4.2.1 Description of the PET insert

MADPET4 (Munich Avalanche Diode PET 4) is a small animal PET insert designed to be operated inside a 7-Tesla Agilent-Bruker Biospec 70/30 MRI scanner. The insert has an inner diameter of 88.0 mm, an outer diameter of 149.7 mm, and an axial field-of-view (FOV) of 19.7 mm. It has 2640 individually read out cerium-doped lutetium-yttrium orthosilicate (Ce:LYSO) scintillation crystals (Hilger Crystals, UK), arranged in a dual layer configuration to mitigate parallax effects. The crystals have a 1.5×1.5 mm^2 cross section area and lengths of 6 mm and 14 mm in the inner and outer layers, respectively. They are placed in eight axial rings with a 2.6 mm pitch, made by 3D printing of a low density plastic (PA-2200, ρ=0.93 g cm^{-3}). This 3D printed structure is white in color and provides optical isolation between neighboring crystals. The geometry of the 3D printed structure and the dimensions of the walls between the crystals are shown in figure 4.1a. Due to the printing precision limitations of the 3D printer and the small distance between the outer layer crystals, the outer layer crystals were not completely covered by the structure.

The crystals are arranged in 66 modules, with 40 detectors per module. Each module consists of 8 rings of 3 outer crystals and 2 inner crystals, which are positioned with

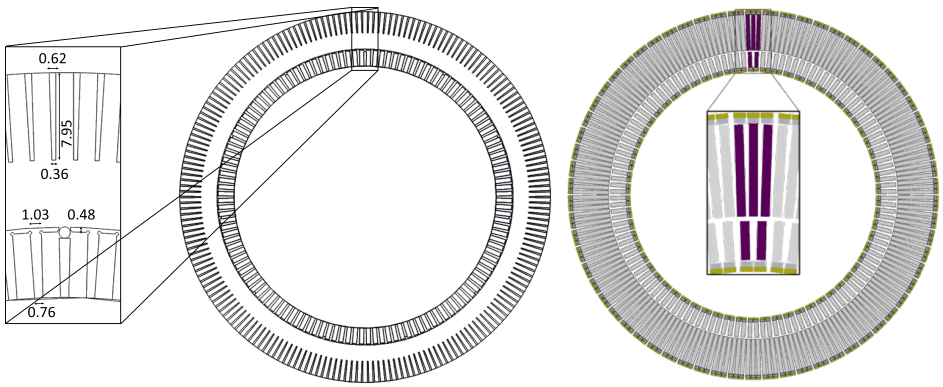

Figure 4.1: The sketches of (a) the 3D printed plastic structure holding the crystals and (b) the symmetric arrangement of the crystals and SiPMs in one ring of MADPET4. Zoomed-in views of the wall dimensions (in mm) and one module of MADPET4 marked in purple color are also shown.

a rotational offset of half the crystal pitch to cover the gaps between the outer layer crystals for a higher photon detection probability. The crystals in each ring are placed equidistantly to their neighbors, all transaxially facing the center of the FOV as shown in figure 4.1b, which makes the system highly symmetric. The inner and outer crystals are read out individually by one-to-one coupling to PM1150NT SiPMs (KETEK GmbH, Germany).

The SiPMs have an active area of 1.2×1.2 mm^2 and 50 μm micro-cells with a fill factor of 70%. A 300 μm layer of epoxy on the micro-cells protects the active area and the wire bonds. A thin layer of optical grease (GE G-688) was applied on the epoxy layer of the SiPMs for optical coupling to the crystals. The SiPMs had an surface-mount device (SMD) package size of $2.45 \times 1.95 \times 1.8$ mm^3 and were mounted on a 6-layer printed circuit board (PCB) with a thickness of 1.25 mm. The PCBs were placed along the axial direction, covering the 8 rings. The SiPM PCBs for read-out of inner and outer layer crystals from one MADPET4 module are shown in figure 4.2. All SiPMs on each PCB (16 for inner, 24 for outer PCB) share a common bias voltage and their signals are routed individually to a 0.4 mm-pitch insulation-displacement contact (IDC) connector (USLS Series, KEL Corporation, Japan) for connection to 1.5 m long ultra-fine (42 AWG) micro coaxial cables (Yeonhab, Japan). These cables transport the SiPM charges to the readout electronics placed outside the MRI scanner and bring the single bias voltage to each PCB. Due to the high internal gain of the SiPMs, no pre-amplifiers and no high frequency electronic components were used inside

the insert. It was therefore possible to omit radio frequency (RF) shielding material from the PET insert, maximizing its transparency to RF transmission and reception with an MRI volume coil surrounding the insert, and minimizing the potential for eddy current generation from, and interference with, the changing MR gradient fields.

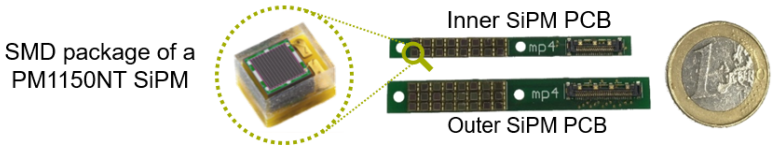

Figure 4.2: The PM1150NT SiPMs mounted on PCBs for read-out of one MADPET4 module of inner and outer layer crystals.

The performance of the SiPMs coupled to the 6 mm Ce:LYSO crystals was evaluated as PET detector modules and compared to other KETEK SiPMs and crystals of the same size in a previous work (Omidvari et al., 2017b). The best energy resolution (FWHM) for 511 keV was 13.7%, which was achieved at a bias voltage of 32 V, and the best coincidence time resolution (FWHM) was 308 ps obtained at a bias voltage of 33 V. All measurements were performed at a room temperature of ∼22°C, with a LeCroy WaveRunner 610Zi digital oscilloscope. Furthermore, the breakdown voltage temperature coefficient of the SiPMs was measured to be 15 mV K^{-1}, which eliminated the need for an SiPM cooling system for the PET insert.

Finally, a 1 mm thick black cylinder, 3D-printed using the same plastic material used for the crystals holding structure, was used for light-tightness, protecting the detector modules, and guiding the 1.5 m cables. The components of the insert which are placed inside the MRI scanner are shown in figure 4.3.

4.2.2 Readout electronics and data acquisition

SiPM signals are read out and digitized by a SiPM data acquisition system (PETsys Electronics, Portugal) composed of three different boards: FEB/A (0808), FEB/D (v2), and DAQ (v2). Each FEB/A board is equipped with two TOFPET1 application-specific integrated circuits (ASICs) and reads up to 128 SiPM channels. The ASIC has two separately configurable thresholds for each channel. A low threshold is used for timing and a high threshold for event validation and energy measurement. The energy information is derived from the SiPM signal charge via the time-over-threshold (ToT) method.

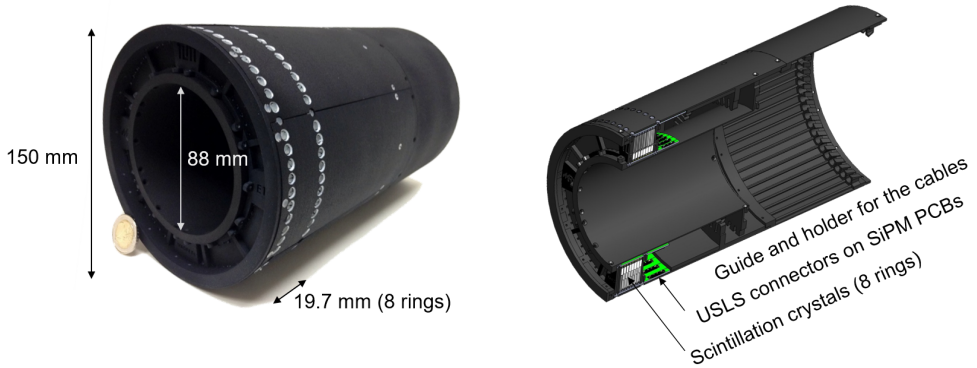

(a) (b)

Figure 4.3: (a) The dimensions of the assembled MADPET4 in its 3D-printed structure and (b) the arrangement of its components.

The 1.5 m coaxial cables from every three MADPET4 modules (40 detectors per module) are connected to an adapter board with a 0.40 mm pitch connector (SS4 Series, Samtec, USA), which connects to one FEB/A board. The complete system is read out by 22 FEB/A boards, which are stacked in 3 groups and placed next to the MRI scanner with 20 cm distance from the entrance of the MRI bore. Every eight FEB/A boards are connected to one FEB/D board, using 3 m long 0.50 mm pitch coaxial flexible cables (HQCD Series, Samtec, USA). This allows for placement of the FEB/D boards at the corner of the MRI room, where the fringe field is below 5 Gauss. Each FEB/D board is equipped with a Kintex 7 field-programmable gate array (FPGA) to collect the data from FEB/A boards and transfer them to the DAQ board. Furthermore, there are DC-DC converters on the FEB/D, which provide the power to the ASICs and bias voltage for the SiPMs. The digital data frames are transmitted from each FEB/D board through a 2 m micro high-definition multimedia interface (HDMI) electrical serial link to a fan-out box placed in the MRI control room. The fan-out box is connected to the DAQ board with a 1 m long CXP copper cable (Molex, USA) and a 2 m long HDMI cable, which powers the fan-out box and brings in the CLOCK, SYNC and GATE LVDS signals. The DAQ board is directly plugged through a PCIe bus to the data acquisition computer running on Linux CentOS 7.

For the current performance evaluation of the scanner, all SiPMs were biased at 31.5 V to be compatible with the charge limitations of the TOFPET1 ASIC. The low threshold of the ToT ASIC was set to 54 digital-to-analog converter (DAC) units for timing and the second threshold was set to 15 DAC units for event validation, which was the

highest available threshold for the ASIC. However, due to the high gain of SiPMs this threshold was still very low and resulted in a large noise peak at the low end of the energy spectra. Therefore, a minimum ToT length was defined in the FPGA for writing the data to disk in order to decrease the data file size and avoiding problems in writing high data rates.

4.2.3 Data processing and coincidence sorting

The limited number of cells in the SiPM active area leads to a saturation effect in SiPMs, which makes the SiPM response, especially with high light intensities, nonlinear with the incoming photon's energy (Renker, 2009). Furthermore, the ToT charge calculation methods which use a constant threshold have a nonlinear behavior, which is affected by the SiPM signal shape. These nonlinearities have to be corrected before coincidence sorting in order to avoid non-uniformities in the reconstructed image due to different energy threshold settings on different detector channels. Therefore, the SiPM response for different gamma energies of 140 keV, 356 keV, 511 keV, and 662 keV, was measured using ^{99m}Tc, ^{133}Ba, ^{22}Na, and ^{137}Cs emission sources, respectively. An exponential calibration curve was obtained for each channel by fitting and it was used for nonlinearity correction of the channel's energy spectra.

Another important calibration step which strongly affects the image quality is the timing alignment of the detectors. System coincidence time resolution of a PET scanner is defined by the full-width at half-maximum (FWHM) of the Gaussian peak in the time difference histogram of all detector pairs in the system. Subsequently, the width of the coincidence time window is set to at least twice the coincidence time resolution (CTR) of the system to maximize the true coincidence rate. However, the random count rate of the system increases linearly with the width of the coincidence time window. Slight variations in cable lengths and detectors' response lead to different propagation delays for the channels. This results in having a different peak shift in the time difference histogram for each line-of-response (LOR) and thus peak broadening of the system time difference histogram and a degraded overall system coincidence time resolution. The individual channel delays of MADPET4 were estimated by an iterative analytical algorithm, in which the time delays are formulated in a matrix-based equation calculated from an acquired data set of the scanner (Mann et al., 2009). Since the structure of the matrix that defines the LORs is well defined, its Moore-Penrose pseudo-inverse matrix can be calculated on the fly by a set of equations with no significant comput-

ing effort (Mann et al., 2009). For MADPET4, the detector channels were divided logically into two opposing segments (each containing 1320 detectors) and only coincidences between the two segments were accepted. The mean value of the time difference histogram was calculated for each fan-sum of LORs, in which one detector was in the first scanner segment and all opposing detectors were in the second segment (Lenox et al., 2001, Mann et al., 2009). The channel delays were estimated in each iteration from multiplication of the Moore-Penrose pseudo-inverse matrix of the fan-sum LOR generator matrix by the vector of mean fan-sum LOR time differences (Mann et al., 2009). The data from a ^{22}Na point source placed at the center of FOV of the scanner was used for the channel delay calculation to minimize the photon traveling time difference between the detector pairs. The channel delays calculated after 50 iterations were used for timing alignment. By applying the estimated channel delays, the system CTR was reduced from 5.5 ns to 1.1 ns.

Single events were stored as list-mode raw data in binary format and were converted to ROOT format offline. The energy calibration, timing alignment, and coincidence sorting were subsequently performed on the ROOT data using C++ programs. The coincidence detection was performed with the single window method, using a 3 ns coincidence time window and with two energy thresholds of 250 keV and 350 keV. Additionally, a geometrical condition was applied on the events to discard the geometrically non-meaningful coincidences with a LOR shorter than 40 mm. Notably, applying this geometrical condition did not reduce the transaxial FOV. Coincidences were stored in line-of-response sinogram format (Rafecas et al., 2004) to avoid any data compression, and preserve the spatial resolution and depth-of-interaction (DOI) information from the input data.

4.2.4 Image reconstruction and system response matrix

For image reconstruction, an order-subsets expectation-maximization (OS-EM) (Lange and Carson, 1984) image reconstruction algorithm was implemented, using Monte-Carlo (MC) simulation based system response matrix (SRM). MC methods provide high detection probability accuracy compared to analytical methods, at the cost of high computation time. Additionally, using MC methods requires an offline calculation of the SRM, otherwise the computation burden during reconstruction is too high. An additional complication of using an offline SRM is that since the SRM contains as many elements as the number of image space elements $\times$ detector pairs ($>10^{13}$ elements for

MADPET4), the file size becomes too large (>38 TB) to be allocated in dynamic memory.

To reduce the simulation time and the required file size for storing the SRM, the cylindrical symmetries of the scanner were exploited. Cylindrical symmetries have been employed in a number of studies using analytical SRMs (Qi et al., 1998, Ansorge, 2007, Scheins et al., 2011) and MC-based SRMs (Herraiz et al., 2006, Zhang et al., 2010, Cabello and Rafecas, 2012) in clinical and pre-clinical systems. The high granularity of the insert allowed using 132 transaxial symmetries, and two axial symmetries. The simulated uniform source used in the MC simulations had a wedge shape, covering one crystal from the inner layer and one and a half crystals from the outer layer. Polar voxels were used to accommodate the image space elements in the cylindrical symmetries (Mora and Rafecas, 2006, Ansorge, 2007, Cabello and Rafecas, 2012). A condition was defined for calculation of each polar voxel's sides to keep a ratio of ∼1 between the chord length and the transaxial length of the voxel. In the center of the scanner this condition could not be satisfied, and could potentially produce image artifacts (Cabello et al., 2010). To avoid such problems, an alternative cylindrical voxelization was implemented in the center of the FOV. Figure 4.4 shows the employed polar voxelization overlaid on the crystal geometry of the insert.

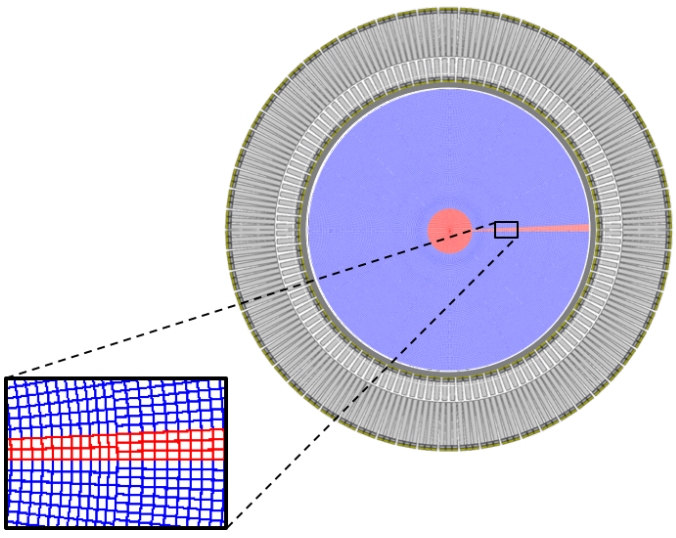

Figure 4.4: Transaxial view of the polar voxelization of the FOV overlaid on the crystal geometry of the insert. The inset shows the details of the polar voxelization. The portion of the voxelization in red represents the simulated and stored volume of the SRM.

The new polar voxelization reduces the number of stored SRM elements to $\sim 1.5 \times 10^{11}$ elements ($\sim$0.5 TB). SRMs contain in general highly sparse information. Thus, the matrix file size was significantly further reduced by storing only the non-zero elements of the SRM. This level of compression is dependent on the length of the SRM simulation and the energy threshold used to discard events stored in the SRM. With a 1600 s simulation time and 50 keV energy threshold, the size of the stored SRM for MADPET4 was reduced to 1.3 GB.

Final reconstructed images were converted from polar to cubic voxels by weighting the intensity value in each polar voxel. The weighting factor was calculated by random sampling of the overlapping volumes between the polar and cubic voxels. A voxel size of $0.375 \times 0.375 \times 0.375$ mm^3 was used for the reconstruction. Subsequently, the slice thickness was increased to 1.125 mm post-reconstruction to improve the noise properties in axial direction and all images were post-filtered using a Gaussian smoothing function with FWHM of 1 mm, unless otherwise stated. No attenuation, scatter, or random correction algorithms were applied on the data.

Since the value $C_{j,voxel}$ of a reconstructed image voxel of measurement j, corresponds to the total number of counts in the duration of acquisition $T_{\mathrm{aq},j}$, the reconstructed image voxel values were corrected for the radioactive decay according to equation 4.1 to represent the activity concentration at the start of imaging. In the equation, $T_{1/2}$ represents the half-life of the radionuclide in minutes, V_{voxel} is the voxel volume in cubic millimeter, and $A_{j,voxel}$ is the activity concentration at the start of imaging in kBq mL^{-1} unit.

$$A_{j,voxel} = \frac{V_{voxel} C_{j,voxel} \ln 2}{60 T_{1/2} (1 - \exp(\frac{-T_{\mathrm{aq},j}}{T_{1/2}} \ln 2))} \tag{4.1}$$

For sections of NEMA NU 4 performance evaluation measurements (NEMA, 2008) which required a filtered-back-projection (FBP) reconstruction algorithm, a 3D FBP algorithm based on the open source software for tomographic reconstruction (STIR) (Thielemans et al., 2012) was used. The STIR implementation of the 3D FBP uses single slice re-binning (SSRB) to reduce the number of sinograms. It also considers the arc-correction, which accounts for the varying distance for different radial bins. In the implementation of the algorithm that was used, a 0.2 cycles cut-off frequency was set for the Colsher filter. The number of bins was set to 601, with a bin width of 0.2 mm and 252 projection angles. Axially, a span of 1, a slice thickness of 1.31 mm, and 15 segments were used.

4.2.5 Normalization correction

To correct the emission data for detector sensitivity variations, individual detector efficiencies and geometrical factors are estimated from a normalization blank scan (Defrise et al., 1991). Since the geometrical factors are included in the MC simulated SRM, the sensitivity matrix has to be corrected only for the detector efficiencies. In statistical iterative based image reconstructions, the sensitivity matrix can be corrected by calculating the normalization factors from LOR efficiencies obtained from a blank scan (Torres Espallardo, 2009). The blank scan for MADPET4 was performed with a uniform cylinder (75 mm diameter, 30 mm height) of water and ^{18}F. The data were acquired for 60 min with 4.9 MBq of activity at the start of scan. Subsequently, LOR efficiency ε_i for each LOR i of the system was calculated from:

$$\varepsilon_i = \frac{{n_i}^{meas}/N^{meas}}{{n_i}^{sim}/N^{sim}} \tag{4.2}$$

where ${n_i}^{meas}$ and ${n_i}^{sim}$ are the number of coincidences for LOR i in the blank scan measurement and the MC simulation of SRM, respectively. Additionally, N^{meas} is the total number of coincidences in the blank scan measurement and N^{sim} is the total number of coincidences in the simulation. The LOR efficiencies were applied to the OS-EM algorithm by modifying the sensitivity matrix elements (Torres Espallardo, 2009):

$$s_k = \sum_{i \in I} a_{i,k} \varepsilon_i \tag{4.3}$$

in which s_k is the sensitivity matrix element for voxel k and $a_{i,k}$ is the SRM element calculated by MC simulations and defined by the probability that an annihilation in voxel k resulted in detection of LOR i.

4.2.6 NEMA NU 4 performance measurements

To characterize the performance of the PET insert for use in typical small animal imaging tasks, the measurements defined by the NEMA Standard Publication NU 4-2008 were performed (NEMA, 2008). The measurements included the spatial resolution, the scatter fraction, the count rate performance, the sensitivity, and the image quality tests. All measurements were performed with the insert outside the MRI scanner, at room temperature.

4.2.6.1 Spatial resolution

The spatial resolution of the PET insert was measured according to the NEMA NU 4 protocol (NEMA, 2008) to provide standardized values which are comparable to other scanners. A ^{22}Na point source (Eckert & Ziegler, Germany) containing 1.98 MBq of concentrated activity was used, in which the activity was confined to a 0.25 mm diameter sphere and was embedded in an acrylic cube of $10\times10\times10$ mm^3 size. The list-mode data were acquired by placing the point source at 0, 5, 10, 15, and 25 mm radial offsets from the center of the FOV, at the axial center of the FOV and at 5 mm distance from the axial center of the FOV. At each location, a 1-min acquisition was performed. The list-mode data were sorted for coincidences using an energy threshold of 350 keV and converted into sinograms. The spatial resolution was calculated radially, tangentially, and axially as the full-width at half-maximum (FWHM) and full-width at tenth-maximum (FWTM) of the point source response function from the 3D FBP reconstructed images.

4.2.6.2 Scatter fraction, count losses, and random coincidence measurements

The relative sensitivity of the scanner to scattered radiation and its count rate performance at different levels of source activity were evaluated with a mouse-like scatter phantom (Quality Assurance in Radiation and Medicine (QRM), Germany). The fillable section of the phantom was filled with 130 MBq of ^{18}F, covering the central 60 mm of the phantom. The first measurement was started 15 min after filling the phantom, with 118.6 MBq of activity and continued for 16.5 hours where the activity had decayed to 0.3 MBq. Additionally, a 30-min measurement of single event count rate was performed with the system without a radioactive source to measure the intrinsic count rate of the scanner due to intrinsic radioactivity of lutetium (^{176}Lu) present in Ce:LYSO scintillators. The list-mode data of all measurements were sorted for coincidences, using energy thresholds of 250 keV and 350 keV and subsequently converted into sinograms. Scatter fraction (SF), true event rate (R_t), random event rate (R_r), scattered event rate (R_s), noise equivalent count rate (R_{NEC}), and total event rate (R_{TOT}) of the system were calculated according to the NEMA NU 4 protocol (NEMA, 2008) for the two energy thresholds.

4.2.6.3 Sensitivity

The sensitivity of the insert to detect positron annihilation gamma rays was measured using the same ^{22}Na point source specified for the spatial resolution measurement. The source was placed on the animal bed and stepped axially through the scanner's axial FOV in steps of 1 mm. At each axial location a 1-min acquisition was performed. The sensitivity of the scanner was evaluated with two energy thresholds of 250 keV and 350 keV. The count rates were obtained at each location on the sinogram data and were corrected for the background rate and the branching ratio of ^{22}Na according to NEMA NU 4 protocol (NEMA, 2008).

4.2.6.4 Image quality

For image quality assessment, the three sections of the NEMA NU 4 image quality phantom were manufactured separately (QRM, Germany) and scanned sequentially due to the short axial FOV of the insert. The three phantoms consisted of the rods, the uniform, and the cold chambers sections of the NEMA NU 4 image quality phantom and were all filled with the same initial activity concentration of 368 kBq mL^{-1}. The scan duration for each phantom was defined according to the activity concentration at the start of imaging of the phantom, in order to have the total emissions for each phantom close to the total number of emissions in the original NEMA NU 4 image quality phantom.

Table 4.1: Measurement settings for imaging the three sections of NEMA NU 4 image quality phantom, compared to the original phantom. A_{cal} is the initial activity concentration measured in a well counter and A_j is the value of decayed activity at the start of imaging, T_j minutes after well counter measurement. Both activity concentrations are shown in kBq mL^{-1} unit and $T_{\mathrm{aq},j}$ is the duration of acquisition in minutes.

Phantom	A_{cal}	T_j	A_j	$T_{\mathrm{aq},j}$
Rods	368.0	60	251.9	15
Cold Chambers	368.0	89	209.8	20
Uniform	368	135	156.9	33
NEMA NU 4	162.4	0	162.4	20

Since the activity concentration at the start of imaging for each phantom was different, all images were corrected according to equation 4.4, to have a reference initial activity concentration of 163 kBq mL^{-1} in all phantoms, which corresponds to 129 min after

the initial activity measurement in a well counter .

$$A_{\mathrm{cal},voxel} = \frac{A_{j,voxel}}{\exp(\frac{129-T_j}{T_{1/2}} \ln 2)} \tag{4.4}$$

Subsequently, the recovery coefficients (RC) of the five rods, the uniformity, and the spill-over-ratio (SOR) for the water-filled and air-filled chambers were measured according to NEMA NU 4 definitions (NEMA, 2008).

4.2.7 Hot-rod high resolution phantom

To evaluate the spatial resolution performance of the scanner in conditions close to imaging conditions of a small animal, where small lesions have to be detected, a mouse-size hot-rod high resolution phantom (QRM, Germany) was used. The total length of the active part of the phantom was 32 mm and the central 12 mm of it contained the fillable hot-rod resolution sections with rod diameters of 0.6, 0.8, 1.0, 1.2, 1.5, and 2.0 mm. The center-to-center separation distance between adjacent rods in each section was twice their diameter. The ^{18}F activity in the complete phantom was 13.16 MBq at the start of scan and the phantom was scanned for 30 min. A 1.125 mm slice thickness was used for the reconstructed image, similar to the NEMA NU 4 measurements.

4.2.8 in vivo simultaneous PET/MR imaging of mouse

Two simultaneous PET/MRI scans with ^{18}F-fluorodeoxyglucose (^{18}F-FDG) were performed on two healthy mice for *in vivo* imaging performance evaluation of the insert. For both scans, the PET insert was placed inside the volume coil of a 7-T Agilent-Bruker BioSpec 70/30 MRI system and the volume coil was used as the RF-transmitter. The first scan was performed on the heart and the second one on the brain.

To show the physiological uptake of ^{18}F-FDG in the left ventricular myocardium, 11.5 MBq of activity was injected to a healthy female mouse and the mouse was scanned at 45 min post-injection for 5 min. The mouse was anesthetized with 2-3% isoflurane during the injection and scan. A two-channel flexible array proton RF receive surface coil (RAPID Biomedical, Germany) was used as RF-receiver for the MRI scan. A fast low angle shot (FLASH) sequence with a flip angle of 10° (with 2.75 ms echo time and 15 ms repetition time) was used for the MR image, providing a resolution of 0.3 mm in all 3 directions. Neither PET, nor MR scans were gated.

The brain PET/MRI scan was performed on a healthy male mouse using a two-channel array rigid-housing proton RF mouse brain receive surface coil (RAPID Biomedical, Germany). A FLASH sequence with a flip angle of 30° (with 4.49 ms echo time and 500 ms repetition time) was used for the MRI scan. The MR images had a 0.15 mm resolution in transverse slices and 1 mm slice thickness. The mouse was under anesthesia with 2-3% isoflurane while it was injected with 6.7 MBq of ^{18}F-FDG and also during the uptake time of 40 min and scan time of 20 min.

4.3 Results

4.3.1 Spatial resolution

The radial, tangential, and axial spatial resolutions (FWHM and FWTM) at the axial center of the FOV and at one-fourth of the axial FOV (5 mm) from the center of the axial FOV are shown in figure 4.5. The number of acquired prompt counts per spatial resolution measurement at each source position was at least 2.5 million. The radial resolution (FWHM) at 5 mm offset from the center at the axial center was 1.32 mm. Furthermore, the radial and tangential resolutions up to 15 mm distance from the center of the FOV varied from 1.29 mm to 1.44 mm (FWHM) at the axial center of the FOV and from 1.33 mm to 1.74 mm (FWHM) at one-fourth of the axial FOV from the center of it. At the axial center, the radial and tangential resolutions (FWHM) were uniform up to 15 mm radial distance from the center, with means and standard deviations (from the 4 offset positions) of 1.38 ± 0.06 mm and 1.39 ± 0.06 mm, respectively. At a radial offset of 25 mm, the radial and tangential resolutions (FWHM) in the axial center (2.02 mm and 1.50 mm respectively) were still below 2.02 mm. At one-fourth of the axial FOV, these values slightly increased to 2.29 mm and 1.63 mm, respectively. The axial resolution showed slightly worse results compared to the other two directions, ranging from 1.64 mm to 2.08 mm (FWHM), at both axial locations.

4.3.2 Scatter fraction, count losses, and random coincidence rate

The count rate performance of the insert as a function of average effective activity in the mouse-like scatter phantom is shown in figure 4.6a, with two energy thresholds of 250 keV and 350 keV. Furthermore, the peak count rate values obtained from the plots are summarized in table 4.2. Using an average effective activity 1.1 MBq, the single event count rate was 5 times the single event count rate of the intrinsic radioactivity

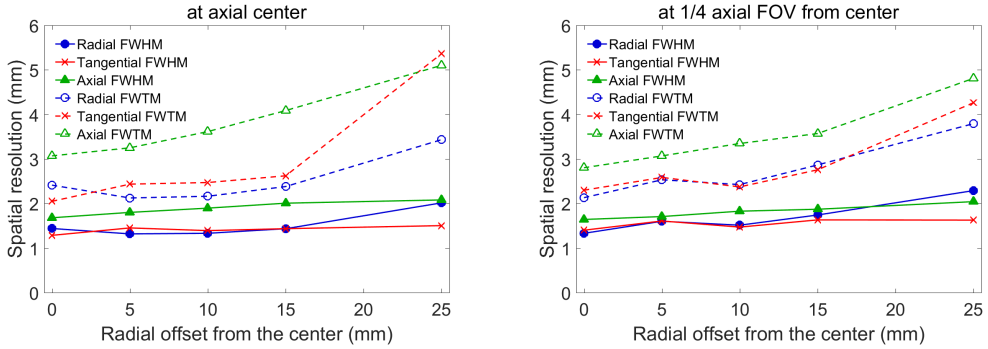

Figure 4.5: Spatial resolution (FWHM and FWTM) measured in three directions (a) at the axial center of the FOV and (b) at one-fourth of the axial FOV from the center of the axial FOV, at different radial offsets from the center. The values were obtained from 3D FBP reconstructed images, using SSRB. Image pixel size of 0.2 mm and slice thickness of 1.31 mm were used in the reconstruction.

of the scanner. The scatter fraction at this activity level was 7.3% and 18.7% with energy thresholds of 350 keV and 250 keV, respectively.

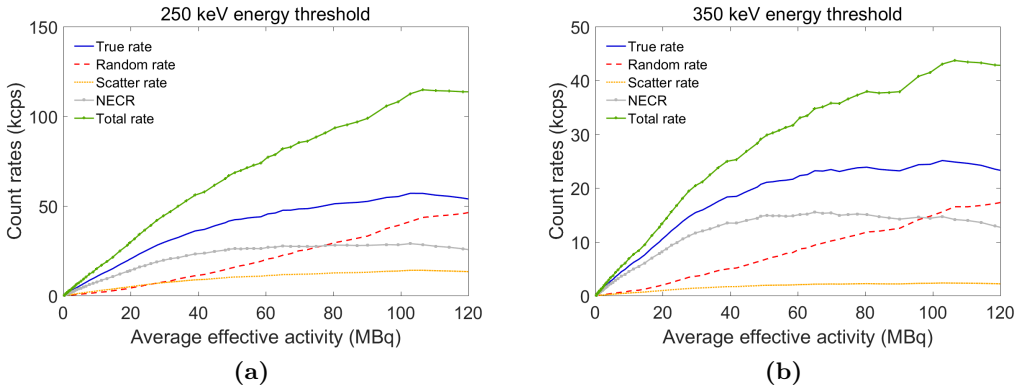

Figure 4.6: System count rate performance as a function of average effective activity in a mouse-like scatter phantom using energy thresholds of (a) 250 keV and (b) 350 keV.

4.3.3 Sensitivity

The axial absolute sensitivity profile of the insert is shown in figure4.7, using energy thresholds of 250 keV and 350 keV. The sensitivity measurement at the center of the scanner contained ~74,000 total counts, corrected for the background event rate. The peak sensitivity of the scanner was 0.72% and 0.49% at the center of the FOV, with energy thresholds of 250 keV and 350 keV, respectively. The asymmetries observed in the

Table 4.2: NEMA NU 4 report for the peak count rate values and the scatter fraction (SF) at 1.1 MBq average effective activity. The activities, $a_{t,peak}$ and $a_{NEC,peak}$, at which the peak true count rate ($R_{t,peak}$) and peak noise equivalent count rate ($R_{NEC,peak}$) are reached are shown respectively. Count rate values are in kilo counts per second (kcps), activities are in MBq, and the scatter fraction is in percentage.

Energy threshold	$R_{t,peak}$	$a_{t,peak}$	$R_{NEC,peak}$	$a_{NEC,peak}$	SF
250 keV	57.1	102.8	29.0	102.8	18.7
350 keV	25.1	102.8	15.5	65.1	7.3

sensitivity profile in the two axial directions were reproduced when the measurements were repeated for the second time.

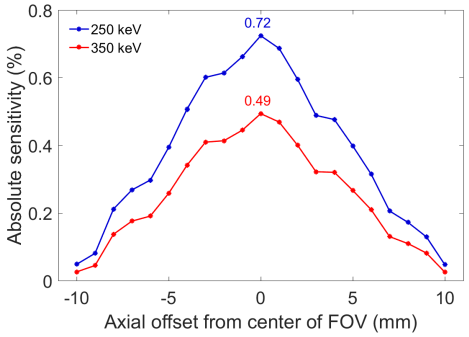

Figure 4.7: Axial absolute sensitivity profile of the insert using energy thresholds of 250 keV and 350 keV.

4.3.4 Image quality

The uniformity parameters of the uniform section of the NEMA NU 4 image quality phantom are compared for two energy thresholds of 250 keV and 350 keV in table 4.3. Using the 250 keV energy threshold results in better uniformity with a 8.3% standard deviation in the uniform region, which increases to 10.7% with the 350 keV energy threshold. However, the mean value of the uniform region with 350 keV energy threshold is 149.0 kBq mL^{-1}, which has a 8% negative bias to the reference 163 kBq mL^{-1} activity concentration in the phantom. This is increased to 284.3 kBq mL^{-1} with the 250 keV energy threshold, which shows a 74% positive bias in the image.

Figure 4.8 shows the recovery coefficients of the five rods for energy thresholds of 250 keV and 350 keV. The standard deviations of the recovery coefficients are shown in error bars. Using the 350 keV threshold, slightly higher recovery coefficients are obtained for the two smallest rods, at the cost of slightly higher standard deviation of the RC values.

Table 4.3: NEMA NU 4 report for the uniformity test, showing the average activity concentration (Mean), the maximum (Max) and minimum (Min) values, and the percentage standard deviation (%STD) in the volume of interest. The activity concentrations are shown in kBq mL^{-1} unit and were calculated using energy thresholds of 250 keV and 350 keV, with 3D OS-EM algorithm (3 iterations and 8 subsets).

Energy threshold	Mean	Max	Min	%STD
250 keV	284.3	375.1	203.9	8.3
350 keV	149.0	232.7	95.8	10.7

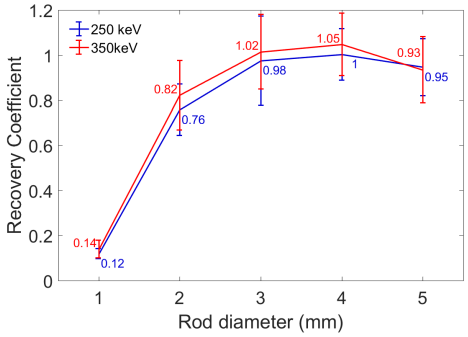

Figure 4.8: Recovery coefficients of the five rods using energy thresholds of 250 keV and 350 keV, calculated for images reconstructed with the 3D OS-EM algorithm (3 iterations and 8 subsets).

The spill-over ratios in the water-filled and air-filled chambers are shown in table 4.4 for the two studied energy thresholds. Using the 350 keV threshold, the spill-over ratios are 19.5% and 11.4% for the water-filled and air-filled chambers, respectively. As expected, these values are increased to 24.2% and 15.4% for the 250 keV threshold. The central transverse slice of the reconstructed images of the three sections of the NEMA NU 4 image quality phantom are shown in figure 4.9 for the two energy thresholds.

Table 4.4: NEMA NU 4 report for spill-over-ratio (SOR) values and their standard deviations in the water-filled and air-filled chambers. The SOR values are shown in percentage and were calculated using energy thresholds of 250 keV and 350 keV, with 3D OS-EM algorithm (3 iterations and 8 subsets).

Energy threshold	Water-filled		Air-filled	
	SOR	%STD	SOR	%STD
250 keV	24.2	0.1	15.4	0.1
350 keV	19.5	0.2	11.4	0.2

4.3.5 Hot-rod high resolution phantom

Figure 4.10 shows the central transverse slice of the reconstructed image of the hot-rod high resolution phantom using an energy threshold of 350 keV. The image was

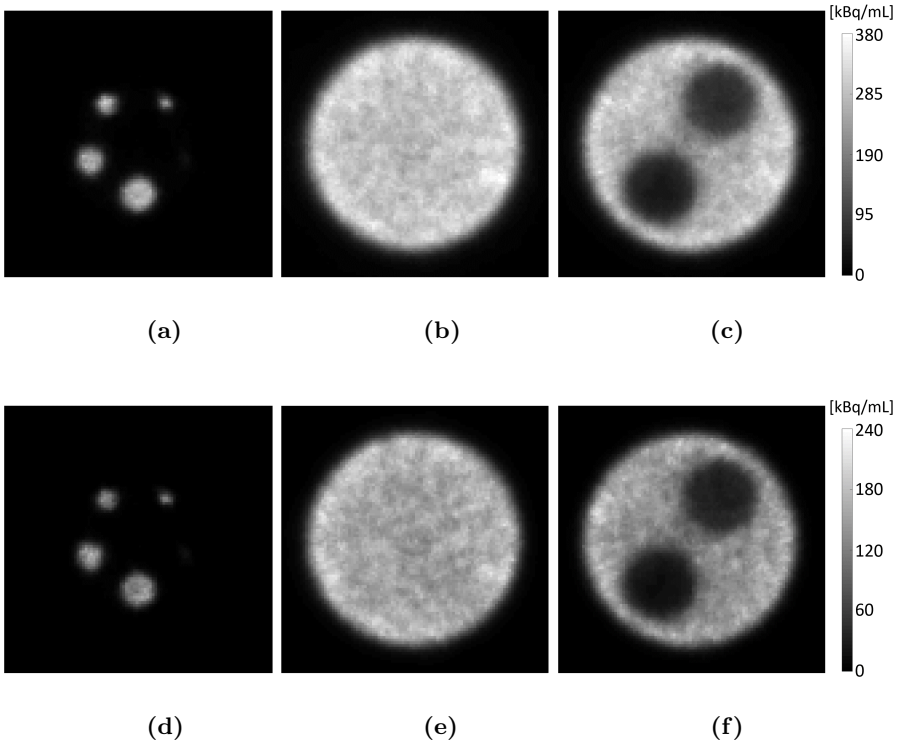

Figure 4.9: Reconstructed images of the central transverse slices of the three sections of the NEMA NU 4 image quality phantom, including ((a) and (d)) rods, ((b) and (e)) uniform, and ((c) and (f)) cold chambers regions. Images were reconstructed using energy thresholds of ((a)–(c)) 250 keV and ((d)–(f)) 350 keV and the OS-EM algorithm with 3 iterations and 8 subsets.

reconstructed with a total of approximately 17 million coincidences. Two line intensity profiles are drawn on the image, passing through th 1 mm, 1.2 mm, 1.5 mm and 2 mm resolution sections. Additionally, next to the reconstructed image, a sketch of the dimensions of the phantom is shown, in which the location of the two line intensity profiles is marked as a reference. As observed in the intensity profiles, all rods down to diameter of 1.2 mm are well-separated through the whole phantom. The first 1 mm rod located at a radial distance of ∼4 mm is also separated from the others.

4.3.6 in vivo simultaneous PET/MR imaging of mouse

The reconstructed image of the ^{18}F-FDG uptake in the heart of a healthy mouse, co-registered to the simultaneously acquired MR image of the mouse, is depicted in figure 4.11. Transverse, coronal, and sagittal slices are shown centered on the heart. Notably, the ^{18}F-FDG uptake in other organs is not visible in the PET image due to the short axial FOV of the insert. Figure 4.12 shows the simultaneous PET/MR image

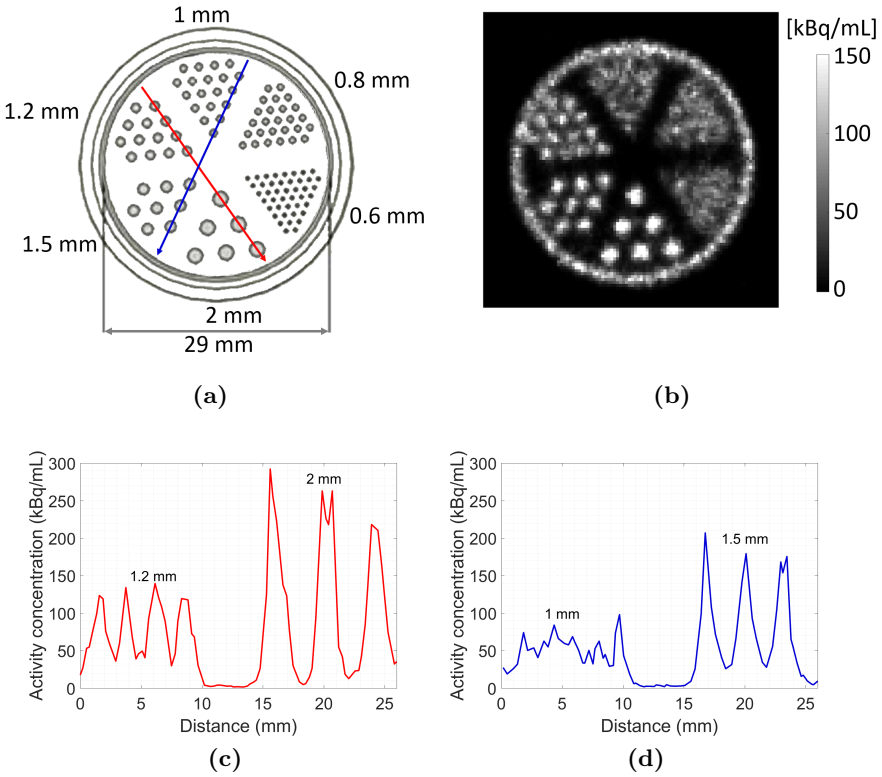

Figure 4.10: (a) The dimensions of the hot-rod high resolution phantom and the location of the intensity profile lines on the resolution sections, (b) the reconstructed image of the phantom, and ((c) and (d)) the two line intensity profiles are shown. The image was reconstructed using an energy threshold of 350 keV, with the 3D OS-EM algorithm (20 iterations and 8 subsets).

of the mouse brain. Three transverse slices are shown in reference to their location in a sagittal central slice. Very low level of activity is observed in the mouse brain. As expected, the highest uptake is observed in the Harderian glands, which were located very close to the edge of the PET axial FOV as shown in the first transverse slice in figure 4.12b. As well, a lower level of activity is observed in the cerebellum and the hippocampus region, which are shown in the other two transverse slices. For both PET images an energy threshold of 350 keV was used and no background filtering was applied on the images.

4.4 Discussion

One of the unique design features of MADPET4 is the individual read out of two radial layers of scintillation crystals. The one-to-one coupling scheme combined with the offsetting of layers allows for exploiting the maximum spatial resolution offered by the

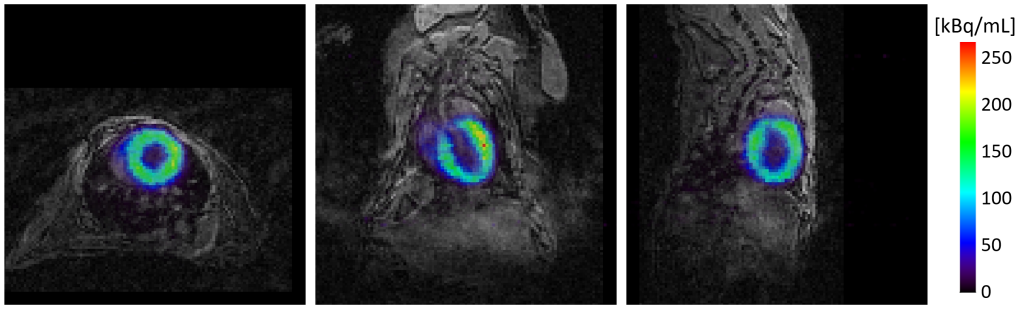

(a) (b) (c)

Figure 4.11: Simultaneous co-registered PET/MR images of the ^{18}F-FDG uptake in the heart of a healthy mouse, shown in (a) transverse, (b) coronal, and (c) sagittal slices. The PET image was reconstructed using an energy threshold 350 keV with the 3D OS-EM algorithm (3 iterations, 8 subsets, and slice thickness of 0.375 mm).

crystal size. This has been demonstrated by the obtained results for the NEMA NU 4 spatial resolution measurements and the hot-rod resolution phantom. The radial and tangential resolutions (FWHM) obtained from the FBP reconstruction are 1.44 mm and 1.29 mm, respectively, at the center of the FOV. Furthermore, as a result of the dual layer geometry of the crystals, a uniform resolution is achieved in a mouse-size FOV (30 mm diameter), in which the average radial and tangential resolutions (FWHM) are 1.38 mm and 1.39 mm, respectively. Comparing these results to other PET scanners, which have reported their resolution measured with a point source and reconstructed with FBP, shows that MADPET4 has a high spatial resolution performance compared to its crystal size. The transaxial resolution of MADPET4 at 5 mm radial offset from the center of the FOV is comparable to values obtained with two SiPM-based PET inserts, based on LYSO crystals with 1.2×1.2 mm^2 cross section size (Ko et al., 2016a, Goertzen et al., 2016). Among other scanners which use larger crystal cross sections, the PET insert from the Seoul National University (Yoon et al., 2012), the PETbox4 standalone system (Gu et al., 2013), and the RatCAP PET insert have reported spatial resolutions in the range of 1.0 mm to 1.3 mm at the center. PETbox4 geometry also offers a uniform spatial resolution over 40 mm diameter FOV. However, the geometry and the components of this scanner are not suitable for an MR-compatible PET insert.

The axial resolution of MADPET4 shows a degraded performance compared to its transaxial resolution. This is partly due to the use of SSRB in the FBP reconstruction and also the 1.1 mm gaps between the crystal rings, which are filled by the plastic

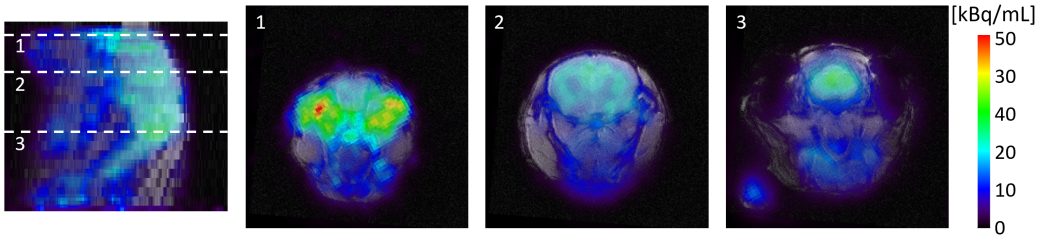

(a) (b) (c) (d)

Figure 4.12: Simultaneous co-registered PET/MR images of the ^{18}F-FDG uptake in the brain of a healthy mouse under anesthesia, shown in (a) one sagittal central slice and ((b)–(d)) three transverse. The location of the transverse slices is marked in the sagittal slice. The image was reconstructed using an energy threshold 350 keV with the 3D OS-EM algorithm (3 iterations, 8 subsets, and slice thickness of 0.375 mm) and post filtered with a Gaussian smoothing function with FWHM of 2 mm.

structure holding the crystals. Although the second layer of crystals partly compensates for the degradation due to these large gaps, a better axial resolution would be achieved by reducing the gap size. The limiting factor in increasing the packing fraction of the crystals in the current design was the SMD package size of the SiPMs. However, this problem could be resolved in future designs by using customized SiPM arrays. Additionally, increasing the axial FOV of the insert would also improve the axial resolution by better geometrical sampling, especially in the central slices, due to an increased number of oblique LORs.

The hot-rod phantom is often scanned and reconstructed with an iterative reconstruction algorithm to represent a more realistic measure of spatial resolution, similar to what is used for animal imaging. The image of the mouse-size hot-rod phantom obtained with MADPET4 showed an image spatial resolution below 1.2 mm over the 30 mm diameter of the phantom. Since the 1 mm rod at 4 mm distance from the center was resolved, a 1 mm resolution can be expected at the center of the FOV. Hot-rod resolution phantoms have been scanned by several groups, some of whom achieved high resolution images that show a good separation of rods with diameters of 1 mm (Mackewn et al., 2010, Wang et al., 2015a, Bergeron et al., 2014, Wong et al., 2012) or below 1 mm (España et al., 2014, Nagy et al., 2013, Schug et al., 2016). However, comparing the images from different scanners requires careful attention to the differences in crystal size, the system sensitivity (affected by the axial FOV), the measurement parameters (such as the amount of activity and acquisition time), reconstruction pa-

rameters (most importantly the slice thickness), and the corrections applied to the image. In several cases, the resolution phantom images were obtained using parameters which differ from the typical values used for animal imaging. Three ultra-high resolution PET scanners are compared here as an example, to demonstrate the effect of these different aspects. The DigiPET insert (España et al., 2014), which has a 32 mm axial FOV and uses 2 mm thick monolithic LYSO crystals together with digital SiPMs, has demonstrated an excellent resolution capability, with 0.7 mm rods being visible in the phantom image. However, the hot-rod phantom, containing 5.5 MBq of activity, was scanned for 8 hours due to the low sensitivity of the scanner. The total number of coincidences during the 8 hour scan was 15 million. This is close to the 17 million coincidences obtained with MADPET4 in the hot-rod phantom, scanned for 30 min with 13 MBq of activity. The NanoScan consecutive PET/MRI system (Nagy et al., 2013) also shows a good resolution capability with an image in which 0.8 mm rods are resolved. With a 94 mm axial FOV and $1.12\times1.12\times13$ mm^3 LYSO crystals, a 4-hour acquisition was performed with the hot-rod phantom containing 9.4 MBq of activity. Finally, with the Hyperion-II^D PET insert (Schug et al., 2016), which has a 97 mm axial FOV and uses $0.93\times0.93\times12$ mm^3 LYSO crystals with digital SiPMs, most of the 0.8 mm rods are visible in the hot-rod phantom image. Although the number of coincidences was in the order of $\sim$50 million due to its high sensitivity, a slice thickness of 2 cm was used to show the hot-rod phantom reconstructed image, to further increase the image statistics and concomitantly have a better separation of the small rods.

One of the main concerns in the design of MADPET4 was the effect of scattering and attenuation of the gamma-photons in the passive components of the scanner. These components include the SiPM-PCBs placed in front of the inner layer of crystals and the plastic structure holding the crystals. The measured SF values showed minimal contribution from these parts, since the SF was 7.3% with a 350 keV energy threshold. This value is lower than what has been reported by many other systems using the same energy threshold (Visser et al., 2009, Kemp et al., 2009, Bao et al., 2009, Wong et al., 2012, Wang et al., 2015a, Goertzen et al., 2012).

As the energy threshold decreases, there is an increased contribution from the optical photons which have reached the SiPMs from a light sharing incident with the neighbor components. In the current version of the system, there are two main sources of light sharing: first, the absence of walls and reflector material in the lower half of the outer-layer crystals, and second, insufficient optical isolation between the neighboring

SiPMs and use of optical grease that can spread to the neighbor SiPM pixels. These two sources of light sharing can be reduced in future designs to improve the accuracy of energy measurement.

The SiPM readout system from PETsys Electronics has shown a stable performance while scanning with up to 118 MBq of activity. Additionally, the one-to-one coupling of the SiPMs and crystals offers a high count rate capability with minimized system dead-time. However, currently the ToT ASIC is not optimized for the SiPMs with such a high gain and high charge. As a result, the threshold settings on the ToT ASIC are not suitable for discarding the low energy events with this type of SiPMs. This could lead to a count rate performance degradation at high activities. Furthermore, the operation of SiPMs at higher bias voltages, where there is an increased charge, is limited by nonlinearity of ToT and saturation of the ASIC. These effects in addition to the saturation of SiPMs and the contributions from light sharing have degraded the energy resolution of detectors and decreased the accuracy of energy characterization of the system. Using a linear ASIC that uses charge integration for energy measurement would improve the performance of the system in the future. This would allow for an accurate characterization of the detectors and thus operation of the SiPMs at their optimum bias voltage and threshold settings.

The NEMA NU 4 performance evaluation results presented in this work were obtained outside the MRI scanner. These results could be affected by simultaneous acquisition of PET and MRI sequences due to electromagnetic interferences or temperature variations resulting from rapidly changing gradients. However, since the breakdown voltage temperature coefficient of the used SiPMs is 15 mV K^{-1}, no significant effects due to temperature variations are expected on the PET performance up to 10 degrees of temperature increase.

The in-house developed OS-EM image reconstruction algorithm and the MC simulated SRM have shown a good capability in terms of image quality. Further improvements can be expected since there may be differences between the assumed system characteristics in the simulated SRM and the real one. The scatter and attenuation corrections will be implemented in the next steps. Including these corrections will improve the SOR values for the cold chambers. Moreover, the observed bias in the images is expected to decrease when using a matching SRM and applying these corrections. The uniformity results, on the other hand, are affected by the phantom attenuation.

The obtained standard deviation values are close to those obtained with LabPET 12 (Bergeron et al., 2014), NanoPET/CT (Szanda et al., 2011), Trans-PET BioCalibrum (Wang et al., 2015a), and ClearPET (Cañadas et al., 2011), in which no attenuation correction was applied.

For the *in vivo* scans, the 350 keV energy threshold is used due to the lower level of background and slightly better recovery coefficient for small lesions. However, including the aforementioned corrections will have a larger effect on the image quality and quantification with 250 keV threshold. Moreover, 250 keV threshold offers 47% more sensitivity and 22% less noise, which is a direct result of higher statistics in the image. The recovery coefficients for the three rods, with diameters of 3 to 5 mm, are close to 1 for both energy thresholds at the third OSEM iteration, where the standard deviation in the uniform region is still below 11%. The 2-mm rod has recovery coefficients of 76% and 82% using the 250 keV and 350 keV thresholds, respectively, which are among the highest values obtained for this rod among the known published NEMA NU 4 characterized scanners up to now (Kim et al., 2007, Visser et al., 2009, Kemp et al., 2009, Bao et al., 2009, Lage et al., 2009, Prasad et al., 2010, Szanda et al., 2011, Wong et al., 2012, Goertzen et al., 2012, Nagy et al., 2013, Gu et al., 2013, Bergeron et al., 2014, Spinks et al., 2014, Wang et al., 2015a, Sato et al., 2016).

Regarding the *in vivo* mouse brain scan, the observed low uptake is expected to be due to the used level of isoflurane for anesthetizing the animal. Nevertheless, some brain regions were still noticeable in the image. The images of the mouse heart scan showed the left ventricular cavity clearly delineated by the myocardium, due to low partial volume effects. These two *in vivo* simultaneous PET/MRI studies have shown that the image quality and resolution performance of the insert are suitable for preclinical multi-modal imaging research.

The short axial FOV of the current prototype of the insert and the gaps between the crystals have primarily affected the sensitivity and thus the noise properties of the images. The random count rate is also increased because most of the activity is outside the FOV. Increasing the axial length of the insert and the number of detectors is feasible in future designs without significant reduction of the transaxial FOV.

4.5 Conclusion

MADPET4 is the first small animal PET insert with dual layer individual detector read-out in combination with the SiPM technology. It was designed with a novel detector arrangement geometry, in which scintillation crystals are placed in a 3D-printed ring structure. All crystals in each ring face the center of FOV, which makes the system highly symmetric. The two layers of crystals also have a radial offset from each other to maximize the photon interaction probability. The one-to-one coupling of the crystals to SiPMs and the parallel read-out in the data acquisition system minimize the system dead time and thus result in a high spatial resolution and high count rate capability.

First performance evaluation results of MADPET4 were presented in this work. The NEMA NU 4 2008 measurements were followed by scanning a resolution phantom and two *in vivo* simultaneous PET/MRI scans. Considering the short axial FOV of the insert (less than 2 cm) and the low packing fraction of crystals in axial direction, the insert has demonstrated a good overall performance compared to other preclinical PET scanners and it can be used for small animal multi-modal research applications.

Chapter 5

MR-compatibility assessment of MADPET4: a study of interferences between an SiPM-based PET insert and a 7 T MRI system

This chapter has been published as "Omidvari N, Topping G, Cabello J, Paul S, Schwaiger M & Ziegler S 2017 'MR-compatibility assessment of MADPET4: a study of interferences between an SiPM-based PET insert and a 7 T MRI system' Physics in Medicine & Biology 63(9) 095002"[1]

5.1 Introduction

Integration of positron emission tomography (PET) and magnetic resonance imaging (MRI) systems was first introduced in 1990 (Hammer, 1990). The idea was explored further by development of several prototype MR-compatible PET scanners based on photomultiplier tubes (PMTs), combined with light guides and long optical fibers (Christensen et al., 1995, Shao et al., 1997, Raylman et al., 2006, Mackewn et al., 2010, Yamamoto et al., 2010). However, the performance of the PET scanner was significantly degraded, mainly due to the light loss during the transfer of the scintillation photons to outside the MRI.

Advances in solid state photodetectors, the interesting properties of avalanche photodiodes (APDs) as PET detectors, and their insensitivity to magnetic fields resulted in a great interest in combined PET/MR systems based on APDs. Early developments

[1] N. Omidvari and G. Topping contributed equally to this work. N. Omidvari conducted the research, authored the manuscript, designed the experiments, performed the data analysis, and carried out the measurements with the PET insert. G. Topping performed the measurements with the MRI scanner, implemented the codes for B_1 field mapping and RF noise scans, and prepared the CSI reconstructed images. The iterative image reconstruction and the coincidence sorting algorithms were developed based on primary source codes of J. Cabello.

were focused on small animal PET scanners for 7 T (Pichler et al., 2006, Judenhofer et al., 2007, Catana et al., 2008) and 9.4 T (Maramraju et al., 2011) MRI systems, and later expanded into development of the first PET insert for human brain imaging (Kolb et al., 2012, Weirich et al., 2012) and the first commercial whole-body simultaneous PET/MR system (Delso et al., 2011) with 3 T MRI. APD-based systems showed promising results in various simultaneous PET/MRI acquisition modes. However, in some cases, the performance of these systems was not fully evaluated with more demanding MRI sequences such as fast spin echo (FSE), echo planar imaging (EPI), and MR spectroscopy (MRS) (Delso et al., 2011, Vandenberghe and Marsden, 2015). In other cases, degradations in MR signal-to-noise ratio (SNR) and PET count rate were reported due to fast switching gradient fields and radio-frequency (RF) interferences (Catana et al., 2008, Judenhofer et al., 2008, Wehrl et al., 2011, Maramraju et al., 2011, Kolb et al., 2012, Yoon et al., 2012, Weirich et al., 2012).

More recent emergence of silicon photomultipliers (SiPM) and their significant advantages over conventional APDs especially in terms of gain, temporal resolution, operating voltage, and tile packing fraction made them promising candidates for photon detection in PET/MRI systems (Vandenberghe and Marsden, 2015). In addition to a commercial SiPM-based whole-body simultaneous PET/MRI system developed by GE Healthcare (Grant et al., 2016), several PET insert prototype designs have been proposed and characterized for small animal (Yamamoto et al., 2011, Kang et al., 2011, Hong et al., 2012, Weissler et al., 2014, Kang et al., 2015, Wehner et al., 2015, Thiessen et al., 2016, Ko et al., 2016b) and human brain imaging applications (Hong et al., 2013, Olcott et al., 2015).

In most PET insert designs, parts of the detector readout electronics (mostly preamplifiers, application-specific integrated circuits (ASICs), or in some cases additional customized circuitry) are placed in close proximity to the detector modules inside the MRI bore. This was an unavoidable condition in conventional systems based on APDs, since the signal amplification circuitry had to be placed directly after the detectors to avoid SNR loss due to the low gain of APDs. However, with the currently available SiPM technology, the amplification is performed passively in the SiPMs with a high gain, resulting in adequately high detector signal amplitudes on the order of hundreds of millivolts. This allows for electrical charge transfer of the signal, up to a few meters of distance from the detectors, without significant loss in the signal. Subsequently, the preamplifiers and other active electronic components from the readout circuitry can be

placed far from the PET/MRI field-of-view (FOV). This reduces the electromagnetic interferences caused by PET active electronic components, reduces the restrictions on shielding material and geometry, and minimizes the thickness of the PET ring, which allow for optimization and application-specific geometrical design of the insert. This approach has been investigated in a few scanner designs with different configurations (Yamamoto et al., 2011, Kang et al., 2011, Hong et al., 2013, Ko et al., 2016b).

In this work, the advantages of using high-gain SiPMs individually read out with the charge transfer approach are studied with a recently developed small animal PET insert for a 7 T MRI system (Omidvari et al., 2017a). The mutual interferences between the two imaging modalities are studied in detail for three RF coil configurations with no electromagnetic shielding material on PET components. The obtained results are compared to previous works to define the requirements for future PET insert designs, which will enable the use of simultaneous PET/MR imaging in a wide range of applications with no degradation compared to stand-alone systems.

5.2 Materials and methods

5.2.1 PET Insert

MADPET4 (Munich Avalanche Diode PET 4) is a small animal PET insert for a 7 T MRI scanner. The geometrical design, the components, and the PET performance of the insert were introduced in detail in a previous study (Omidvari et al., 2017a). A summary of the characteristics of the insert, which are specifically relevant for the MR-compatibility study are presented here.

The insert has an inner diameter (ID) of 88.0 mm, an outer diameter (OD) of 149.7 mm, and an axial FOV of 19.7 mm. With the given ID and OD dimensions of the insert, it can be used either with a large RF volume coil placed outside the insert, or a small RF volume coil placed inside it. It has 2640 cerium-doped lutetium-yttrium orthosilicate (Ce:LYSO) scintillation crystals (Hilger Crystals, UK), arranged in a dual layer configuration with 6 mm and 14 mm crystals in inner and outer layers, respectively. The crystals have a cross section area of 1.5×1.5 mm^2 and are individually read out by one-to-one coupling to SiPMs (KETEK GmbH, Germany), with an active area of 1.2×1.2 mm^2. The SiPMs are mounted on a 1.25 mm-thick 6-layer printed circuit board (PCB). No ground layer was defined in the PCBs. However, a small

surface containing several holes and vertical interconnect accesses (vias), on one of the PCB layers was assigned to the common bias voltage for the SiPMs.

The SiPMs and the crystals have been shown to be suitable as preclinical PET detector modules, especially regarding their energy resolution, time resolution, and temperature sensitivity (Omidvari et al., 2017b). With breakdown voltage temperature coefficient of 15 mV K^{-1} and gain of $\sim 7 \times 10^6$, they were chosen for use in the PET insert. The high gain of the SiPMs eliminated the need to place active electronic components such as preamplifiers in the PET insert. The SiPM signal charge was transferred to outside the MRI bore using bundles of 1.5 m-long ultra-fine (42 AWG) micro coaxial cables (Yeonhab, Japan). The cables were connected to the PCBs at both ends by 0.4 mm-pitch insulation displacement contact (IDC) connectors (USLS Series, KEL Corporation, Japan). In total, 132 bundles of coaxial cables were used for the readout of the PET insert, including 66 bundles of 20 cables for inner-layer SiPMs and 66 bundles of 30 cables for outer-layer SiPMs. No filters or cable traps were used for the cables. The cables in each bundle were covered by a 2.5 mm-diameter isolator tube (Versatile V4 5.0 model, Tyco Electronics Corporation, USA) and were guided to outside the MRI bore in parallel to the Z axis of the scanner, using a 3D-printed cylindrical structure.

The data acquisition system (PETsys Electronics, Portugal) of the insert is composed of 22 FEB/A (0808) boards, 3 FEB/D (v2) boards, 1 fan-out box, and 1 DAQ (v2) board. No electromagnetic interference (EMI) shielding components were used for the insert or any of the readout boards. The coaxial cables from MADPET4 detector modules were connected to the FEB/A boards using customized interface boards. Each FEB/A board is equipped with two TOFPET1 ASICs and reads out the signals from 120 MADPET4 detectors, using the time-over-threshold (ToT) method. The FEB/A boards were stacked in 3 groups and placed at a 20 cm-distance from the MRI bore entrance.

The FEB/D boards, the fan-out box, and the DAQ computer were placed outside the MRI room Faraday cage, in the MRI control room. Each FEB/D board was connected to eight FEB/A boards using 3 m-long 0.50 mm-pitch coaxial flexible cables (HQCD Series, Samtec, USA). The connection of the cables to the control room was via the feed-through holes in the MRI room Faraday cage, without any filters. The FEB/D boards were powered using a HMP4040 programmable four-channel power

supply (Rohde & Schwarz, USA), placed in the control room. The FEB/D boards, equipped with Kintex 7 field-programmable gate arrays (FPGAs), collected the data from the FEB/A boards. Furthermore, the power for the ASICs and the bias voltage for the SiPMs was provided by on-board 3W DC-DC converters on the FEB/D boards. A 2 m-long micro high-definition multimedia interface (HDMI) electrical serial link was used to transmit digital data frames from each FEB/D board to the fan-out box. The DAQ board was directly plugged to the data acquisition computer through a PCIe bus connection and it was connected to the fan-out box with a 1 m-long CXP copper cable (Molex, USA) and a 2 m-long HDMI cable.

5.2.2 MRI system

The MRI system is a preclinical 7 T Agilent/GE MR901 magnet, currently operating with Bruker AVANCE III HD electronics and running on Paravision software release 6.0.1. The system is equipped with Agilent Discovery HD gradient coil with an OD/ID of 305/210 mm, providing maximum gradient strength of 300 mT m^{-1}. Two RF volume coils were used in this study for RF transmission, suitable for different PET/MR imaging applications.

The first coil was a ^{1}H transmit/receive (Tx/Rx) large volume coil (RAPID Biomedical GmbH, Germany) with an OD/ID of 208/150 mm. This coil encloses the PET insert, has a resonator length of 190 mm and a maximum peak transmit power of 2 kW, and could be used for imaging rats. Since the received RF signal is attenuated by the presence of the PET insert, for imaging smaller objects such as mice or specific rat organs, a ^{1}H flexible two-channel surface receive array coil (RAPID Biomedical GmbH, Germany) was used for RF reception. The surface coil has a resonator length of 42.5 mm and the flexible part could completely enclose objects with an OD up to 24 mm. The housing of the flexible part has a 52.5×75 mm^2 area and 11 mm thickness.

The second volume coil was a ^{13}C/^{1}H Tx/Rx small volume coil (RAPID Biomedical GmbH, Germany). With an OD/ID of 87/31 mm, the coil was placed inside the PET insert, for mouse and rat head imaging at two resonance frequencies. The coil could provide a maximum peak transmit power of 1 kW and has a resonator length of 46 mm and 43 mm for ^{1}H and ^{13}C imaging, respectively. For EMI-shielding, the coil has a cylindrical layer of 9 μm-thick copper foil and 1 μm-thick FR4 around its components, with no front and rear shielded caps.

5.2.3 Effects of PET on MRI

5.2.3.1 Static magnetic field homogeneity

To study the effects of the PET insert on local static magnetic field variations, B_0 field maps were generated using the built-in FieldMap sequence of the MRI scanner with the two RF volume coils. The sequence was based on a 3D double gradient echo (GRE) acquisition. The B_0 field maps were generated by calculating the phase difference, followed by phase unwrapping, and subsequently conversion to a frequency map scaled in resonance frequency units. No signal-to-noise ratio (SNR) threshold was defined for generating the field maps. The field maps were obtained at coronal, sagittal, and transverse central slices in three configurations: without the PET insert, with the insert in place but inactive (with PET off), and with the insert on and acquiring (with PET on). For the latter configuration a syringe containing ∼40 MBq of ^{18}F was placed next to the PET insert to have adequate single count rate during the acquisition. For each configuration, two B_0 field maps were generated; first with setting all the shim parameters to zero and second with an automatic volume shimming up to 2nd order, using the MAPSHIM adjustments. The shim adjustments were optimized for a predefined volume at the center of the phantom. The acquisition parameters, summarized in table 5.1, were kept constant for all configurations for each coil.

Table 5.1: Acquisition parameters used for generating the B_0 field maps.

Scan parameter	Large volume coil	Small volume coil
Repetition time (ms)	50	50
First echo time (ms)	2.28	2.99
Echo spacing (ms)	3.81	3.81
Effective echo time (ms)	6.63	6.80
Number of averages	1	1
Flip angle	30°	30°
Matrix size	180×100×100	80×40×40
Pixel size (mm^2)	1×1	1×1
Slice thickness (mm)	1	1
Bandwidth (kHz)	400	100

To generate the B_0 field maps when the MRI scanner is used with the large volume coil, a cylindrical plastic bottle (77 mm diameter, 138 mm length) containing 550 ml aqueous solution of 0.5 mM Dotarem gadolinium-based contrast agent was placed at the iso-center of the MRI scanner. In order to exclude the effects of the phantom positioning on the field maps, one side of the phantom that was outside the PET

insert was fixed to the volume coil, using a holder made of high-density foam. The shim adjustments were optimized for a centered shim volume of 71.0×43.7×44.6 mm^3.

With the small volume coil, a 50 ml centrifuge tube (29 mm diameter, 115 mm length) containing the same aqueous solution of Dotarem was placed at the iso-center of the MRI scanner. Since the phantom was attached to the volume coil in this case, slight variations in relative position of the phantom to the gradient coil have to be considered in comparison of the field maps with and without the PET insert. A centered shim volume of 33.8×9.7×10.0 mm^3 was used for the shim adjustments.

5.2.3.2 B_1 field mapping

The effects of the PET insert on the RF field (B_1) homogeneity and consequently the flip angle distribution were studied by B_1 field mapping. This is especially important for quantitative MRI studies, as inhomogeneities in the B_1 field lead to varying signal intensities across the same tissue. The same phantoms described for the static magnetic field homogeneity tests were used with the two volume coils. The flip angle distribution maps were obtained for the three configurations of without the PET insert, with PET off, and with PET on. For all configurations, the acquisitions were performed after generating the B_0 field maps with shimming adjustments. B_1 mapping was performed for each configuration with a series of 2D RF-spoiled GRE sequences, varying in RF pulse amplitude. At each pixel, signal was phase-corrected, and the rate at which real signal varied with voltage was fit for an effective B_1 scaling factor, plotted in arbitrary units. The acquisition parameters for each coil are summarized in table 5.2 and they were kept constant for all configurations.

Table 5.2: Acquisition parameters used for B_1 field mapping.

Scan parameter	Large volume coil	Small volume coil
Repetition time (ms)	500	500
Echo time (ms)	3.27	2.80
Number of averages	1	1
Matrix size	180×100	80×40
Pixel size (mm^2)	1×1	1×1
Slice thickness (mm)	1	1
Tx Bandwidth (kHz)	3	3
Number of scans	25	31
RF pulse amplitude range (V)	1.0–165.0	0.1–60.0

5.2.3.3 RF noise scans

The RF noise introduced by the PET insert to MR images was measured by performing noise scans using the SinglePulse sequence of the MRI scanner. This sequence acquires a free induction decay (FID) signal after RF excitation and produces a non-localized frequency spectra from the Fourier transform of the acquired FID. To exclude the excitation pulse from the sequence and only have the contribution from the background noise, the RF transmit power and flip angle were set to zero. The receiver gain was set to 64 and a repetition time of 100 ms was used. In each acquisition, 256 repetitions were defined for 32768 frequency points in an acquisition bandwidth of 1 MHz. The acquisition parameters were kept constant and measurements were performed using a reference frequency of 300.22 MHz for ^{1}H with the two RF volume coils and the surface receive coil. All measurements were repeated three times for each of the configurations of without PET, with PET off, and with PET on. Additionally, with the small volume coil, the scans were repeated with ^{13}C operation mode using a reference frequency of 75.49 MHz.

The acquired signal in MRI can be represented as a vector with real and imaginary components. When no RF-pulse stimulation is present, the received MR signal should only include the background noise, in which the real and imaginary components are independently and identically Gaussian distributed with zero mean. This makes the absolute value of the complex number Rayleigh distributed with a scale parameter equal to the standard deviation (SD) of its Gaussian components. Therefore, after the acquisition of the frequency spectra in the noise scans, the Rayleigh scale parameter was calculated in MATLAB from the absolute values of the 256 acquisitions for each of the 32768 frequency points. The Rayleigh scale parameter was subsequently plotted as a measure of noise across the acquisition bandwidth.

5.2.3.4 Image quality

To study the effects of the PET insert on image quality of MRI scans, the two phantoms used for the field map measurements were placed at the iso-center of the scanner and scanned using different MR sequences. The 550 ml phantom was used with the large volume coil in Tx/Rx mode, to represent the rat-body imaging scenarios. The 50 ml phantom was used in two scan configurations to represent mouse and rat head imaging scenarios: first, with the large volume coil as transmitter and the flexible surface coil as receiver, and second, with the small volume coil in Tx/Rx mode. A $T1$-weighted

GRE, a $T2^*$-weighted GRE, a $T2$-weighted spin echo (SE) with one refocusing pulse, an SE-echo planar imaging (EPI), and an FID-EPI sequence were used for MRI scans.

Furthermore, a 2D phase-encoded chemical shift imaging (CSI) sequence was used with the small volume coil to obtain ^{13}C spectroscopic images. The sequence used 512 spectral acquisition points per phase encode and the chemical shift offset was set to 163.5 ppm. 15 Hz line broadening was applied before Fourier-transforming in the spectral dimension. ^{13}C images were reconstructed in MATLAB from the scanner's partially reconstructed FID output and 7 frequency bins around the peak frequency were summed to obtain the images for image quality analysis. A 50 ml centrifuge tube, containing 1.8 M ^{13}C Urea and 50 mM Dotarem contrast agent, was used as a uniform phantom.

The acquisition parameters for each sequence are summarized for imaging the 550 ml phantom and the 50 ml phantom in tables 5.3 and 5.4, respectively. All scans were repeated five times. For each measurement setup, the coil was tuned and matched, the reference power was adjusted, and an automatic linear volume shimming was performed. The pulse powers were automatically calculated, based on the reference power and the defined flip angle for each case. The receiver gain was adjusted for each scan and the final images were normalized to the receiver gain. SNR and image homogeneity were calculated for each MR image as measures of image quality. The SNR was defined as the ratio of the mean signal in a 20 mm-diameter circular region of interest (ROI) at the center of the large phantom and the SD in several ROIs containing the same total number of voxels in the background. The SNR values were scaled with a 0.655 factor, to correct for the Rician distribution of background noise in magnitude images. For the small phantom, a 10 mm-diameter circular ROI was used. The SNR was averaged for the five acquisitions for each sequence and compared for different configurations of without PET, with PET off, and with PET on. The image homogeneity was defined based on the maximum ($S_{\max}$) and minimum ($S_{\min}$) values in the ROI in the phantom by:

$$\textit{image homogeneity} = 100 \times (1 - \frac{S_{\max} - S_{\min}}{S_{\max} + S_{\min}}). \tag{5.1}$$

5.2.4 Effects of MRI on PET

The effects from the gradient fields switching and the RF pulses of the MRI scanner were studied as the two main potential sources of interference. PET total prompt

Table 5.3: Acquisition parameters used for MRI sequences with the large volume coil for image quality comparison of the 550 ml uniform phantom.

Scan parameter	$T1$-GRE	$T2^*$-GRE	$T2$-SE	FID-EPI	SE-EPI
Repetition time (ms)	40	500	1000	1000	1000
Echo time (ms)	4.2	20	12	18	45
Number of averages	10	1	1	1	1
Matrix size	200×200	200×200	200×200	50×50	50×50
Pixel size (mm^2)	0.5×0.5	0.5×0.5	0.5×0.5	2×2	2×2
Slice thickness (mm)	1	1	1	1	1
Nominal flip angle	40°	40°	90°/180°	90°	90°/180°
Receive BW (kHz)	100	100	100	100	100
Excitation BW (kHz)	12	12	2.1	2.1	2.0
Refocusing BW (kHz)	-	-	2.0	-	0.6

Table 5.4: Acquisition parameters used for MRI sequences with the small volume coil and the flexible surface coil for image quality comparison of the 50 ml uniform phantom.

Scan parameter	$T1$-GRE	$T2^*$-GRE	$T2$-SE	FID-EPI	SE-EPI	CSI
Repetition time (ms)	40	500	1000	1000	1000	1000
Echo time (ms)	5	20	12	25	60	-
Number of averages	10	1	1	1	1	1
Matrix size	200×200	200×200	200×200	100×100	100×100	16×16
Pixel size (mm^2)	0.5	0.5	0.5	1	1	2
Slice thickness (mm)	1	1	1	1	1	5
Nominal flip angle	40°	40°	90°/180°	90°	90°/180°	30°
Receive BW (kHz)	100	100	100	250	250	6
Excitation BW (kHz)	4.8	4.8	2.1	2.1	2.0	5
Refocusing BW (kHz)	-	-	0.6	-	0.6	-

coincidence counts were measured with a ^{22}Na point source placed inside the PET insert. Finally, the scattering and the attenuation effects from the components of the small volume coil inside the PET insert were studied by imaging a uniform phantom.

5.2.4.1 Radio-frequency interferences

The radio-frequency interferences introduced by the two volume coils on the PET insert were studied by testing different RF pulses used in GRE, SE, and SinglePulse sequences. The effect of SE sequence was only studied with the small volume coil, due to difficulty in generation of 180° pulses with the large volume coil because of high reference power. All the gradient powers were set to zero in the GRE and SE sequences to study the RF interferences exclusively. All sequences were performed at the ^{1}H frequency and the SinglePulse sequences were repeated at the ^{13}C frequency with the small volume coil. The RF pulse shapes were defined as calculated type, similar to how they are typically used in small animal MR imaging. The duration

of all MR sequences was 40 s. A 30 s PET acquisition was started immediately after starting the sequence with a 1.8 MBq ^{22}Na point source placed at the center of the PET insert and at the iso-center of the MR scanner. The point source was attached to the end-face of the 50 mL Dotarem phantom during all measurements. Each PET/MRI acquisition was compared to the immediately following 30 s PET acquisition without any MR sequence, to exclude temperature effects on PET data. Each measurement was repeated three times to account for statistical variations in PET data.

The GRE sequences used were composed of an excitation pulse, with a calculated shape and flip angles in the range of 1–90°, and a repetition time of 20 ms. To change the RF duty cycle, the scans were performed with pulse lengths of 1, 2, and 10 ms. The resulting excitation pulse powers used in each scan are listed in tables 5.5 and 5.6 for the large and small volume coils, respectively.

Table 5.5: Excitation pulse powers (W) of calculated RF pulses in GRE sequences, used to study the RF interferences of the large volume coil.

	Flip Angle						
Pulse length (ms)	90°	60°	45°	30°	10°	5°	1°
1	-	-	-	597.78*	296.35	73.97	2.96
2	-	-	-	-	74.09	18.49	0.74
10	289.38	115.18	62.54	27.13	2.96	0.74	0.03

*Maximum transmit power possible to provide a 14.2° flip angle.

Table 5.6: Excitation pulse powers (W) of the calculated RF pulses in the modified GRE sequences with the small volume coil, used to study the effect of RF pulses on PET.

	Flip Angle					
Pulse length (ms)	90°	60°	45°	30°	10°	1°
1	63.85	25.41	13.80	5.99	0.654	0.0065
2	15.96	6.35	3.45	1.50	0.163	0.0016
10	0.64	0.25	0.14	0.06	0.007	0.0001

The SE sequences consisted of a 90° excitation pulse followed by eight 180° refocusing pulses, with a repetition time of 2300 ms. The length of the excitation pulse and the refocusing pulses were varied from 0.5 ms to 2 ms together with changing the transmission bandwidth (BW), resulting in different pulse powers. All sequences also contained a Gaussian pulse for fat suppression with pulse length of 2.6 ms and pulse power of 0.16 W, which was not altered between different sequences. The pulse powers for the excitation and refocusing pulses used in each sequence are specified in table 5.7.

Table 5.7: Pulse powers of the 90° excitation pulse and the 180° refocusing pulses, and the transmission bandwidth, used in the modified SE sequence with the small volume coil, for studying the effect of RF pulses on PET.

Pulse length (ms)	Excitation pulse power (W)	Refocusing pulse power (W)	Transmission BW (Hz)
0.5	13.76	107.90	8400
1	3.44	26.97	4200
2	0.86	6.74	2100

The RF pulses in the SinglePulse sequence were 10 ms-long block pulses with a repetition time of 50 ms. The effect of these pulses on PET was studied at ^{1}H and ^{13}C frequencies, by changing the excitation pulse power from 0.1 W to 200 W. Since commonly used MR sequences often have longer durations, several minutes or longer, the effect of RF pulses on PET prompt counts and the energy spectra of SiPMs were studied in 30 min MR scans. PET data acquisition was performed with series of 30 s measurements starting from 5 min before the start of MR scan and continued until 5 min after the 30 min MR scan was ended. The aforementioned SinglePulse sequence containing RF block pulses was used for both volume coils with an excitation pulse power of 80 W.

5.2.4.2 Effects of the gradient fields switching

To study the effects of the gradient fields switching on PET acquisition exclusively, EPI sequences were modified by setting their RF excitation pulse power to zero. All measurements were performed while the small volume coil was placed inside the PET insert. The matrix size was varied to change the gradient duty cycles. Gradient readouts in all three directions were tested with four different gradient duty cycles and slew rates, as listed in table 5.8. Similar to the RF interference tests, MR sequences were 40 s, followed by a 30 s simultaneous PET acquisition, with the 1.8 MBq ^{22}Na point source, and compared to the subsequent 30 s PET acquisition with no MR sequence running. Each measurement was repeated three times with the same acquisition settings. Additionally, the temperature of one of the outer-layer SiPM PCBs was monitored during all measurements using an MR-compatible monitoring and gating system (SA Instruments Inc., USA).

Table 5.8: The gradient duty cycles and slew rates used in modified EPI sequences to study the effects of the gradient fields switching on PET.

Gradient duty cycle (%)	Gradient slew rate (T m^{-1} s^{-1})
90	575
60	611
48	699
27	734

5.2.4.3 Attenuation and scattering effects

The attenuation and scattering effects of the components of the small volume coil were evaluated by comparing the PET images of a 21 mm-diameter plastic syringe, filled with 4.6 MBq of ^{18}F in 6 ml water, which was scanned for 10 min with the small volume coil in the insert and for 15 min without the coil when the activity had decayed to 3.1 MBq. The PET images were reconstructed with an energy threshold of 350 keV using an ordered subset expectation maximization (OS-EM) algorithm with 8 subsets and 3 iterations (Omidvari et al., 2017a). No attenuation, scatter, or random correction was applied to the data.

5.3 Results

5.3.1 Static magnetic field homogeneity

The effect of the PET insert on the static magnetic field homogeneity is shown in figures 5.1 and 5.2, depicting the coronal B_0 field maps obtained with the large volume coil and the small volume coil, respectively. The maps were scaled in parts per million (ppm) unit relative to a reference frequency of 300.22 MHz for ^{1}H imaging. All B_0 maps are shown for the two cases of setting all the shim parameters to zero and after automatic MAPSHIM adjustments up to 2nd order. Contour lines up to ± 1 ppm were added to the B_0 maps as a visual reference for the standard acceptable range of changes in the static magnetic field.

To explain the inhomogeneities observed in the field maps, the location of the SiPM PCBs from one module of the PET insert is shown relative to one of the B_0 maps obtained with the PET insert in figure 5.1c. The schematics of the measurement setup with the large volume coil and the small volume coil are provided in figure A.1 and A.2 of the supplementary material, respectively. In these schematics, the location and

the components of the SiPM PCBs are shown in a larger scale next to the B_0 maps of figure 5.1f and 5.2f for the two coil configurations.

As observed in the obtained B_0 maps, the presence of the insert causes substantial changes in the static magnetic field homogeneity. However, most of these inhomogeneities were compensated and corrected in the imaging FOV by performing the automatic volume shimming up to 2nd order. Furthermore, turning on the PET acquisition did not have substantial effect on the B_0 maps. With the large volume coil after shimming, the B_0 field map variations in the imaging FOV ranged from -0.04 ppm to 0.09 ppm without the PET insert and from -0.09 ppm to 1.09 ppm with the PET insert. With the small volume coil, the variations in the imaging FOV after shimming ranged from 0.08 ppm to 0.27 ppm without PET, from -0.18 ppm to 0.05 ppm with PET off, and from -0.30 ppm to -0.06 ppm with PET on.

5.3.2 B_1 field mapping

Figure 5.3 and 5.4 show the flip angle distributions obtained by B_1 field mapping with the large volume coil and the small volume coil, respectively. The presence of the insert in the large volume coil had notable effects on the B_1 field strength. The normalized distribution of the B_1 field is only slightly degraded by the presence of the insert. However, an average reduction of 64% can be observed in the B_1 field, which results in a lower flip angle for a given excitation power. With the small volume coil, negligible differences appear in the normalized distribution and absolute values of the B_1 maps, and only small differences are observed at the corners of the field maps.

5.3.3 RF noise scans

Figure 5.5 shows the RF noise scans obtained with the large volume coil, the flexible surface receive coil, and the small volume coil operated at ^{1}H and ^{13}C frequencies. The plots were shown for a 400 kHz window centered on the reference frequency, for better visualization of the effects.

Among the noise scans obtained at the ^{1}H reference frequency (300.22 MHz), the largest RF noise is observed when the large volume coil is used as RF receiver. The noise level in proximity of the ^{1}H central frequency shows an increase up to $\sim$37%, just by placing the insert inside the coil. After powering the PET data acquisition components on, an increase of $\sim$145% is observed compared to the noise level without the insert. With the flexible surface receive coil, the increases in the noise level are

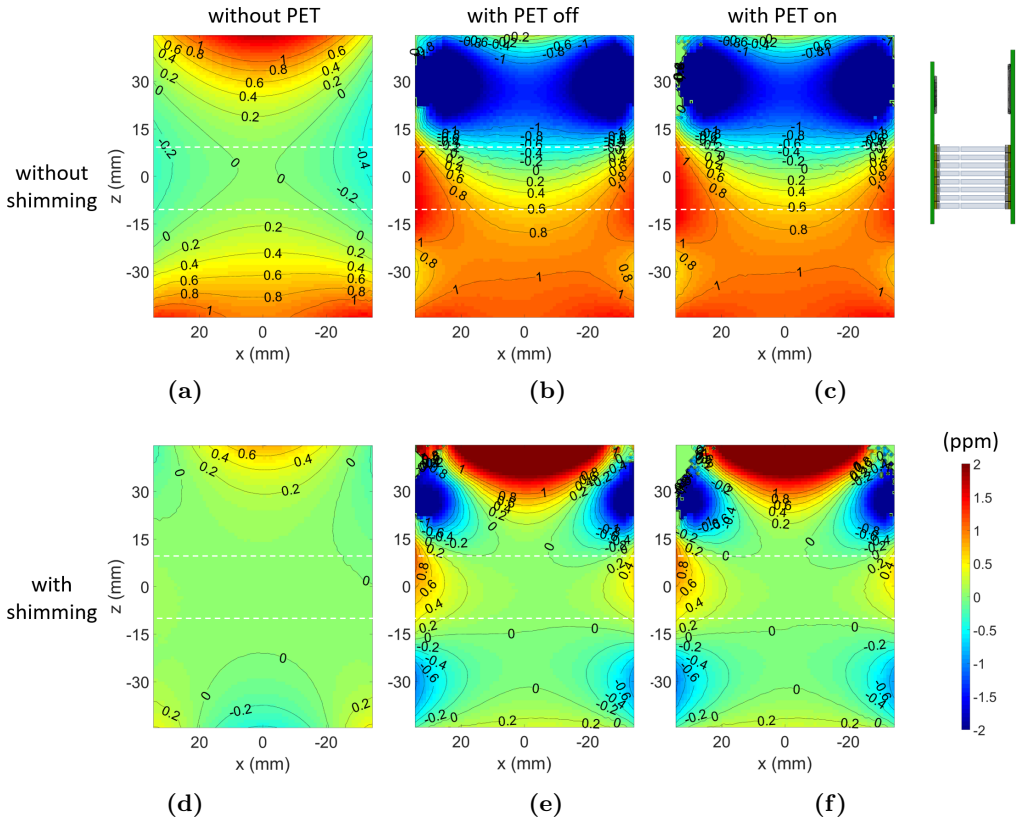

Figure 5.1: Coronal B_0 field maps with contour lines up to ±1 ppm, generated with the large volume coil ((a) and (d)) without the PET insert, ((b) and (e)) with the PET insert inside the MRI scanner and off, and ((c) and (f)) with the PET insert on and acquiring. The location of the PCBs of the PET detector modules are shown relative to one of the B_0 maps (c) obtained with the PET insert in place. All the field maps are shown with the same color scale. Top row shows the field maps with setting all the shim parameters to zero and bottom row after automatic MAPSHIM adjustments up to 2nd order. The imaging FOV of PET is marked with white dashed lines on the maps.

reduced to ∼14% and ∼66%, with the PET insert off and on, respectively. With the small volume coil, the presence of the PET insert has negligible effect on the noise level in MR. However, turning on the PET electronics, increases the noise level by ∼10%. Furthermore, in all three coil configuration, various narrow frequency spikes at fixed locations, with 31.5 kHz intervals, are observed in the noise spectra when the PET electronics is on and acquiring.

The RF noise scans performed with the small volume coil at ^{13}C central frequency (75.49 MHz), show patterns that are very distinctive from the noise scans around 300.22 MHz. Significant increase in the noise level is observed when the insert is

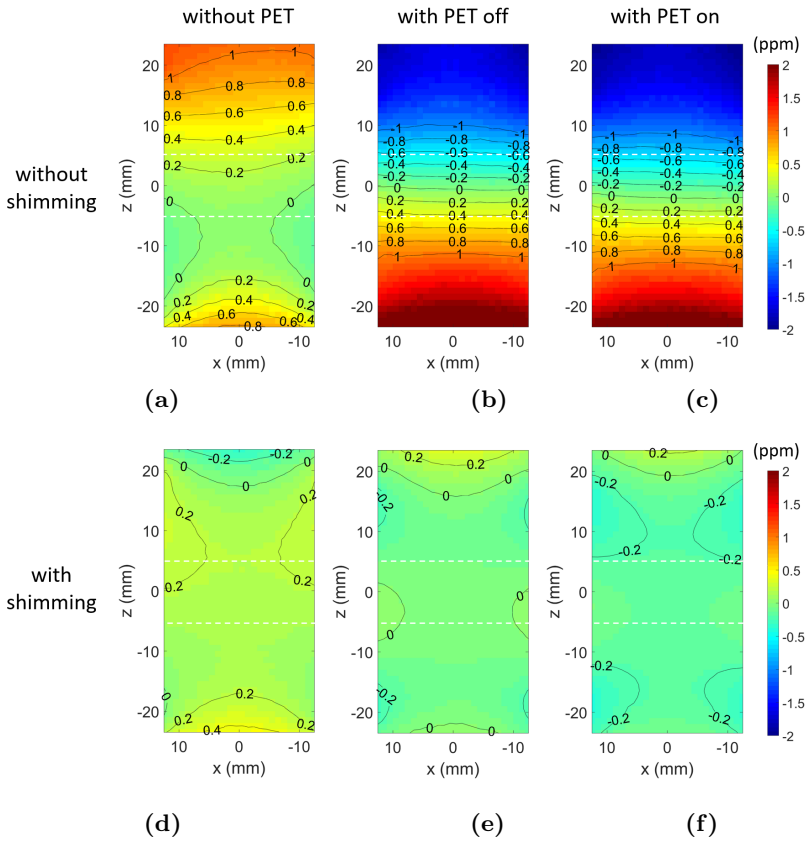

Figure 5.2: Coronal B_0 field maps with contour lines up to ± 1 ppm, generated with the small volume coil ((a) and (d)) without the PET insert, ((b) and (e)) with the PET insert inside the MRI scanner off, and ((c) and (f)) with the PET insert inside the MRI scanner on and acquiring. All the field maps are shown with the same color scale. Top row shows the field maps with setting all the shim parameters to zero and bottom row after automatic MAPSHIM adjustments up to 2nd order. The imaging FOV of PET is marked with white dashed lines on the maps.

present, and powering the data acquisition system shows negligible effect on the noise baseline. However, some high-amplitude wide peaks are added to the spectrum, which increase the noise in proximity of the central frequency.

5.3.4 Image quality

Figure 5.6 shows the MR images of the 550 ml uniform phantom, obtained by the GRE, SE, and EPI sequences, with the large volume coil used for RF transmission and reception. Due to the substantial effects of the insert on signal and noise, the images were not shown in the same intensity scale. The EPI images obtained in this case suffered from distortions and artifacts, including ghosting artifact and Gibbs

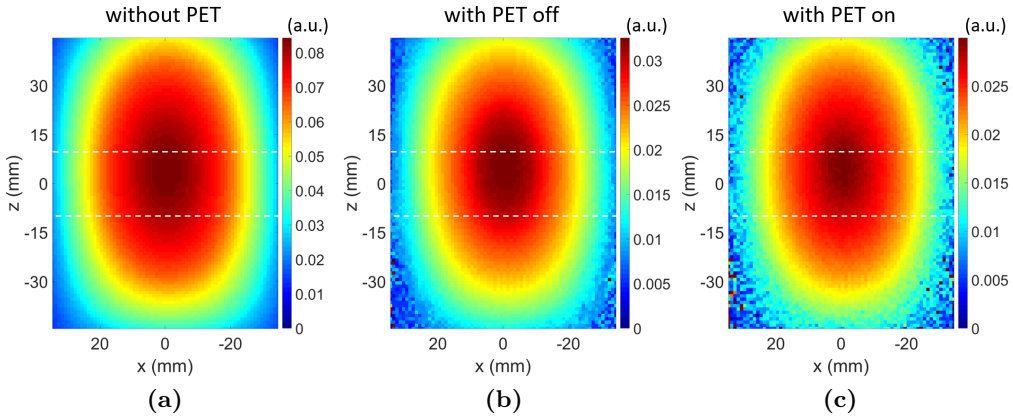

Figure 5.3: The flip angle distributions, resulted from B_1 mapping, with the large volume coil (a) without the PET insert, (b) with the PET insert inside the MRI scanner off, and (c) with the PET insert inside the MRI scanner on and acquiring. The flip angle distributions are shown in different color scales, to compare the normalized distribution in the three cases. The imaging FOV of PET is marked with white dashed lines on the coronal maps.

ringing. The presence of the PET insert intensified these artifacts, resulting in no meaningful images. Therefore, the EPI scans were not included for SNR evaluation. The T2* GRE and T2 SE sequences showed artifacts with and without the insert. In all the MR images obtained when the PET insert was acquiring, a low-intensity zipper artifact can be seen on the right side of the phantom. The SNR values and the image homogeneity of the images are compared in tables 5.9 and 5.10, respectively. SNR losses of 72–75% are observed in the three used sequences, just due to the presence of the insert. Furthermore, turning the PET electronics on has resulted in 87–88% SNR loss in the MR images compared to without PET. The image homogeneity is also 5–7% and 10–20% lower with PET off and on, respectively.

Table 5.9: SNR (mean±SD of five repetitions) of the images obtained with different sequences using the large volume coil.

	$T1$-GRE	$T2^*$-GRE	$T2$-SE
without PET	195.5±5.2	204.7±2.7	165.5±2.1
with PET off	55.2±0.9	50.9±0.5	45.0±0.4
with PET on	24.3±0.6	27.4±0.6	21.6±0.6

Table 5.10: Image homogeneity (%) mean±SD of five repetitions, obtained with different sequences using the large volume coil.

	$T1$-GRE	$T2^*$-GRE	$T2$-SE
without PET	89.2±0.1	70.9±0.2	62.4±1.1
with PET off	83.8±0.6	67.1±0.9	57.9±0.8
with PET on	80.0±0.6	64.0±1.4	49.8±2.2

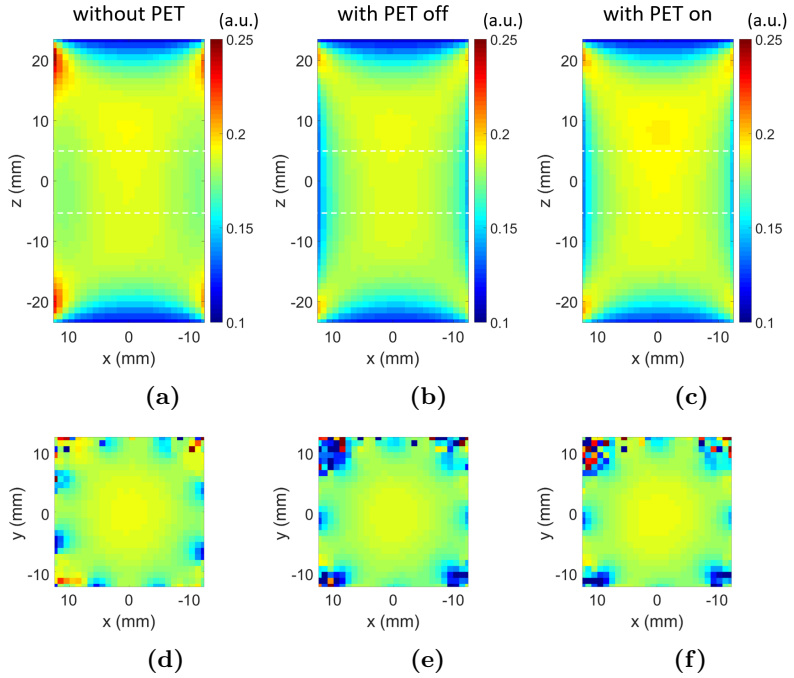

Figure 5.4: The flip angle distributions, resulted from coronal and axial B_1 mapping, with the small volume coil ((a) and (d)) without the PET insert, ((b) and (e)) with the PET insert inside the MRI scanner off, and ((c) and (f)) with the PET insert inside the MRI scanner on and acquiring. The imaging FOV of PET is marked with white dashed lines on the maps.

Figure 5.7 shows the MR images of the 50 ml uniform phantom, obtained using the large volume coil for RF transmission and the flexible surface coil for RF reception, with and without the insert. The signal intensity in all images is not uniform over the phantom area, since the flexible coil did not cover the full phantom and could not provide uniform receive sensitivity. Furthermore, using the surface coil has resulted in some distortions in the EPI images. The images are shown in the same intensity scale for each sequence and the effects from the insert are visually hard to notice. The SNR values listed in table 5.11 show 9–28% SNR loss with different sequences due to the presence of the insert and 45–59% SNR loss when the PET electronics is on. The image homogeneity results are compared in table 5.12. Negligible effects from the PET insert are observed on the image homogeneity of the first three sequences. However, the two EPI sequences had slightly more artifacts with the PET insert and 5–8% less image homogeneity.

The images of the 50 ml uniform phantom, obtained with the small volume coil using six MR sequences are shown in figure 5.8, in the three cases of without PET, with

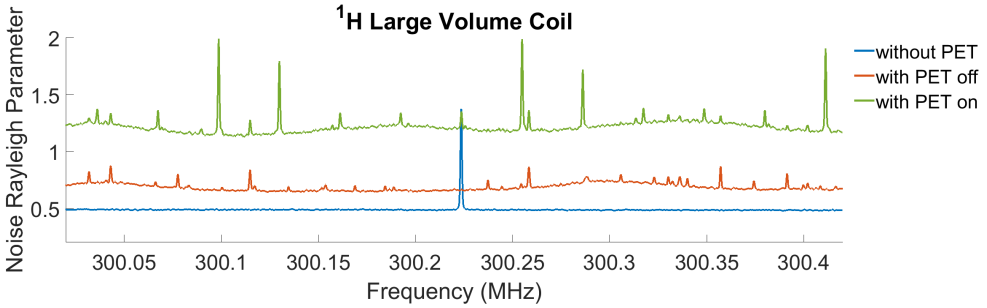

(a)

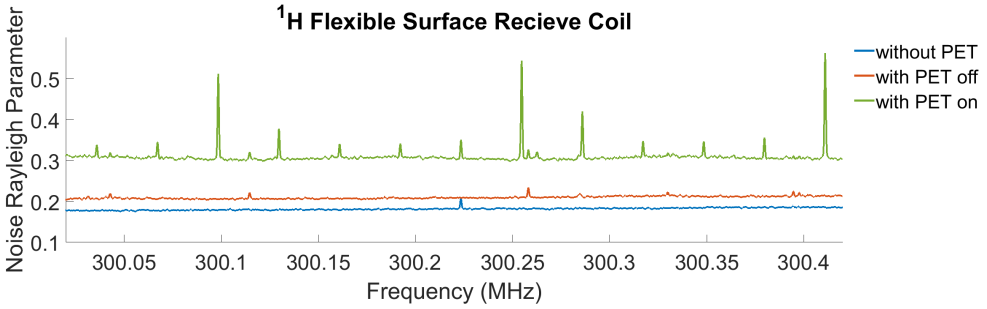

(b)

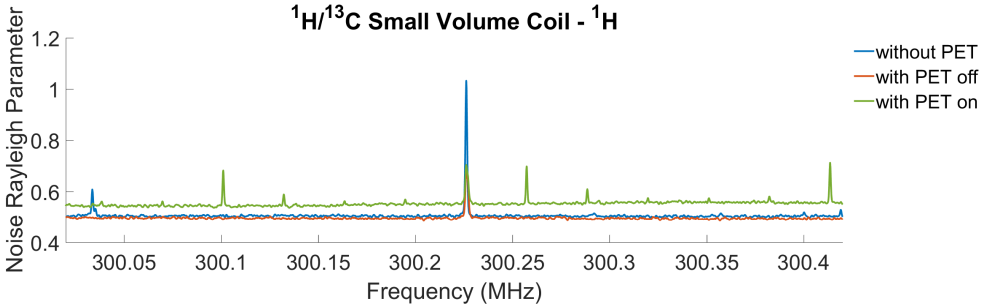

(c)

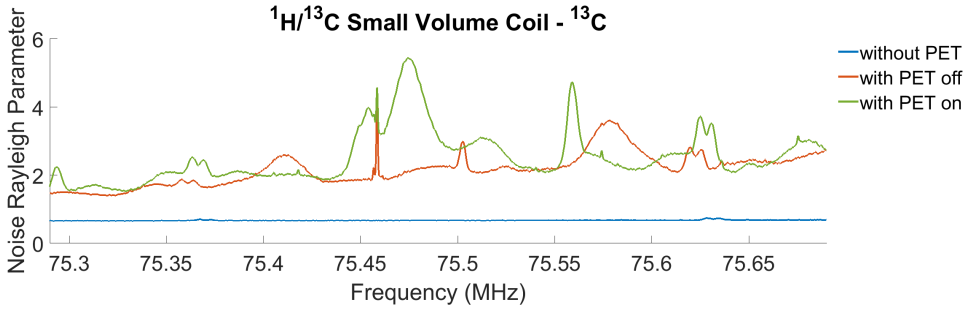

(d)

Figure 5.5: RF noise scans obtained with (a) the large volume coil, (b) the flexible surface receive coil, (c) the small volume coil operated at ^{1}H frequency, and (d) the small volume coil at ^{13}C frequency.

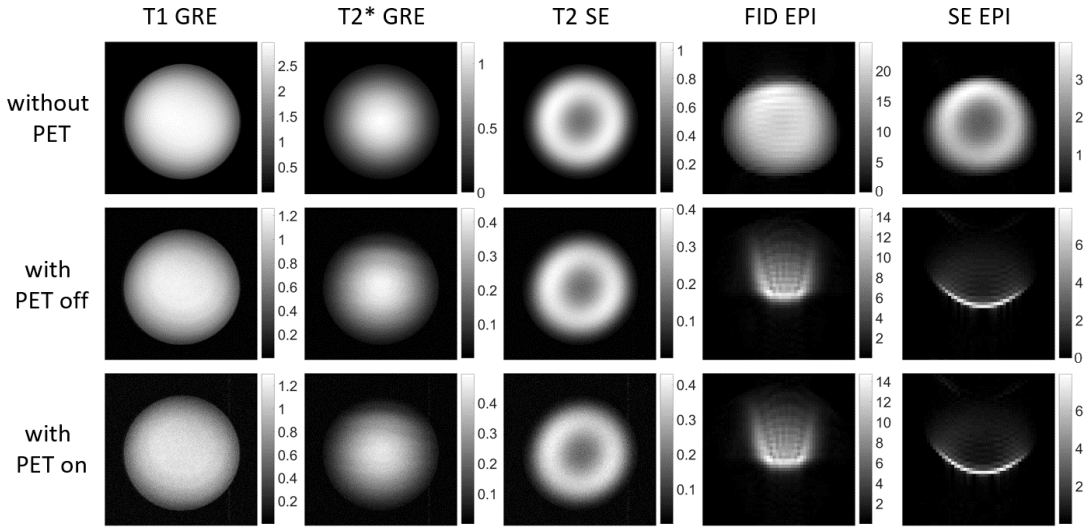

Figure 5.6: The MR images of the large uniform phantom, obtained with different sequences using the large volume coil for RF transmission and reception, without the PET insert (first row), with the PET insert inside the MRI scanner off (second row), and with the PET insert inside the MRI scanner, on and acquiring (third row). Due to the substantial effects of the insert on signal and noise, the images are shown in different intensity scales.

Table 5.11: SNR (mean±SD of five repetitions) of the images obtained with different sequences using the flexible surface coil.

	$T1$-GRE	$T2^*$-GRE	$T2$-SE	FID-EPI	SE-EPI
without PET	1104±19	547±11	239±5	1201±29	183±10
with PET off	948±24	391±4	194±6	912±46	146±7
with PET on	549±9	226±5	115±4	545±28	86±3

PET off, and with PET on. The images obtained with each sequence in the three configurations are shown in the same intensity scale. The effects due to the presence of the insert and operation of its readout electronics on image quality of the six used sequences are visually negligible. Therefore, the SNR and image homogeneity of the images are listed for comparison in tables 5.13 and 5.14, respectively. Presence of the PET insert has resulted in 4–15% and 23–30% decrease in the SNR of the ^{1}H imaging sequences with PET off and on, respectively. With CSI, the SNR is very similar regardless of the state of PET readout electronics and about 16% lower than the SNR obtained without PET. The PET insert shows negligible effect on the image homogeneity of the first three imaging sequences. Slightly more image artifacts are observed with the insert in the two tested EPI sequences, resulting in 6–14% decrease

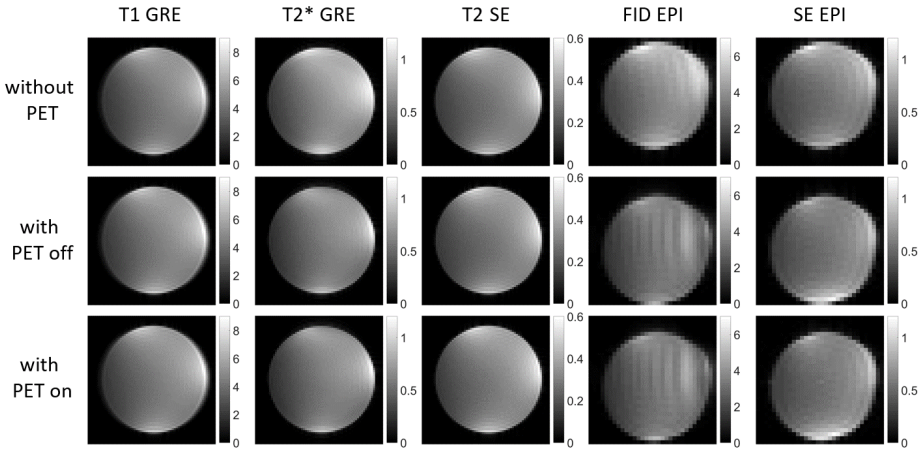

Figure 5.7: The MR images of the small uniform phantom, obtained with different sequences using the large volume coil for RF transmission and the flexible surface coil for reception, without the PET insert (first row), with the PET insert inside the MRI scanner and off (second row), and with the PET insert inside the MRI scanner, on and acquiring (third row). The three images for each sequence are shown in the same intensity scale. All images were cropped to a 32×32 mm^2 window for better visualization.

Table 5.12: Image homogeneity (%) mean±SD of five repetitions, obtained with different sequences using the flexible surface coil.

	$T1$-GRE	$T2^*$-GRE	$T2$-SE	FID-EPI	SE-EPI
without PET	54.3±0.4	50.3±0.1	56.9±0.2	54.8±0.1	59.1±0.2
with PET off	53.6±0.1	51.2±0.1	56.4±0.7	52.1±0.1	54.2±0.1
with PET on	53.9±0.1	51.2±0.2	55.9±0.8	51.6±0.1	58.9±0.4

in image homogeneity. The presence of the insert has also shown a small effect, 2–3% decrease, on image homogeneity with the CSI sequence.

Table 5.13: SNR of the images (mean±SD of five repetitions) obtained with different sequences using the small volume coil.

	$T1$-GRE	$T2^*$-GRE	$T2$-SE	FID-EPI	SE-EPI	CSI
without PET	872±22	429±5	191±10	1012±52	143±3	25±1
with PET off	835±6	385±10	163±5	933±14	136±7	21±2
with PET on	669±22	316±5	134±3	765±31	108±4	21±3

5.3.5 Radio-frequency interferences

Figure 5.9 shows the effect of different types of RF pulses on PET prompt count rate performance. The RF pulses from the large volume coil had a larger effect on the prompt counts, as expected. With the calculated pulses in GRE sequences, count losses up to 25% were observed when high-power RF pulses were used with 50% RF

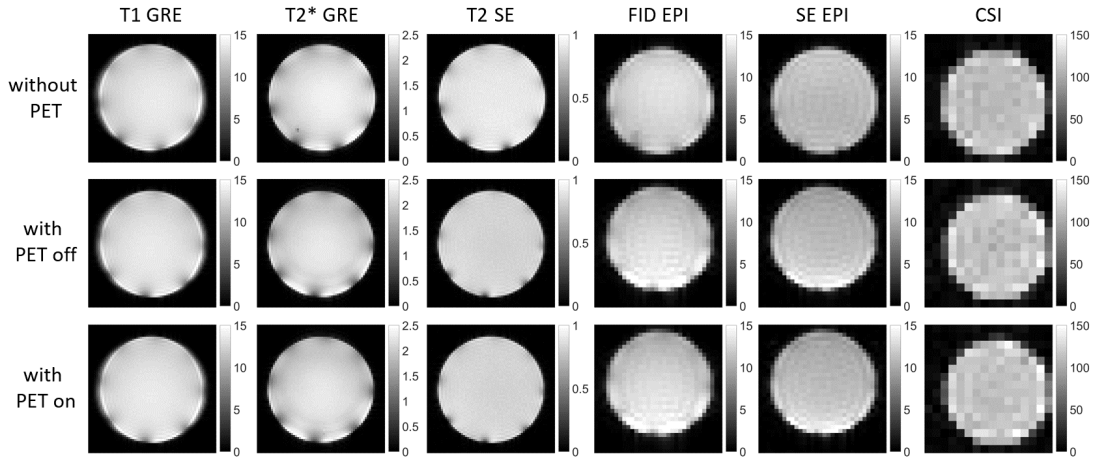

Figure 5.8: The MR images of the small uniform phantom, obtained with different sequences using the small volume coil, without the PET insert (first row), with the PET insert inside the MRI scanner off (second row), and with the PET insert inside the MRI scanner on and acquiring (third row). The three images for each sequence are shown in the same intensity scale. All images were cropped to a 32×32 mm^2 window for better visualization.

Table 5.14: Image homogeneity (%) mean±SD of five repetitions, obtained with different sequences using the small volume coil.

	$T1$-GRE	$T2^*$-GRE	$T2$-SE	FID-EPI	SE-EPI	CSI
without PET	89.4±0.6	83.8±0.2	91.0±0.5	88.6±0.1	91.4±0.2	90.6±1.1
with PET off	89.6±0.1	84.3±0.3	93.3±0.1	83.4±0.1	79.6±0.4	87.8±1.9
with PET on	89.6±0.1	84.1±0.3	92.8±0.4	83.0±0.1	79.0±0.3	88.9±1.3

duty cycle. With the block pulses, PET count loss was equal to the RF duty cycle for excitation pulse powers exceeding 100 W.

Use of GRE excitation RF pulses with the small volume coil, shown in figure 5.9c, had a small effect on PET count rate and the observed count losses did not show a notable dependency on pulse power and pulse length. Using a 50% RF duty cycle (pulse length of 10 ms) and a 90° flip angle resulted in an average count loss of 0.3% compared to running no MR sequence. The average and SD of observed count losses with all tested RF pulses and various duty cycles in this case was 0.2±0.7%, which is slightly higher than ±0.5% prompt count SD observed with PET insert in absence of any MR sequence. With the gradients-disabled SE sequences, which use eight refocusing pulses, the average PET count loss reached to 1.9% with 108 W refocusing pulses. Additionally, as shown in figure 5.9d, the block pulses showed a significantly larger effect on PET count rate. In this case, pulse powers greater than 100 W has resulted

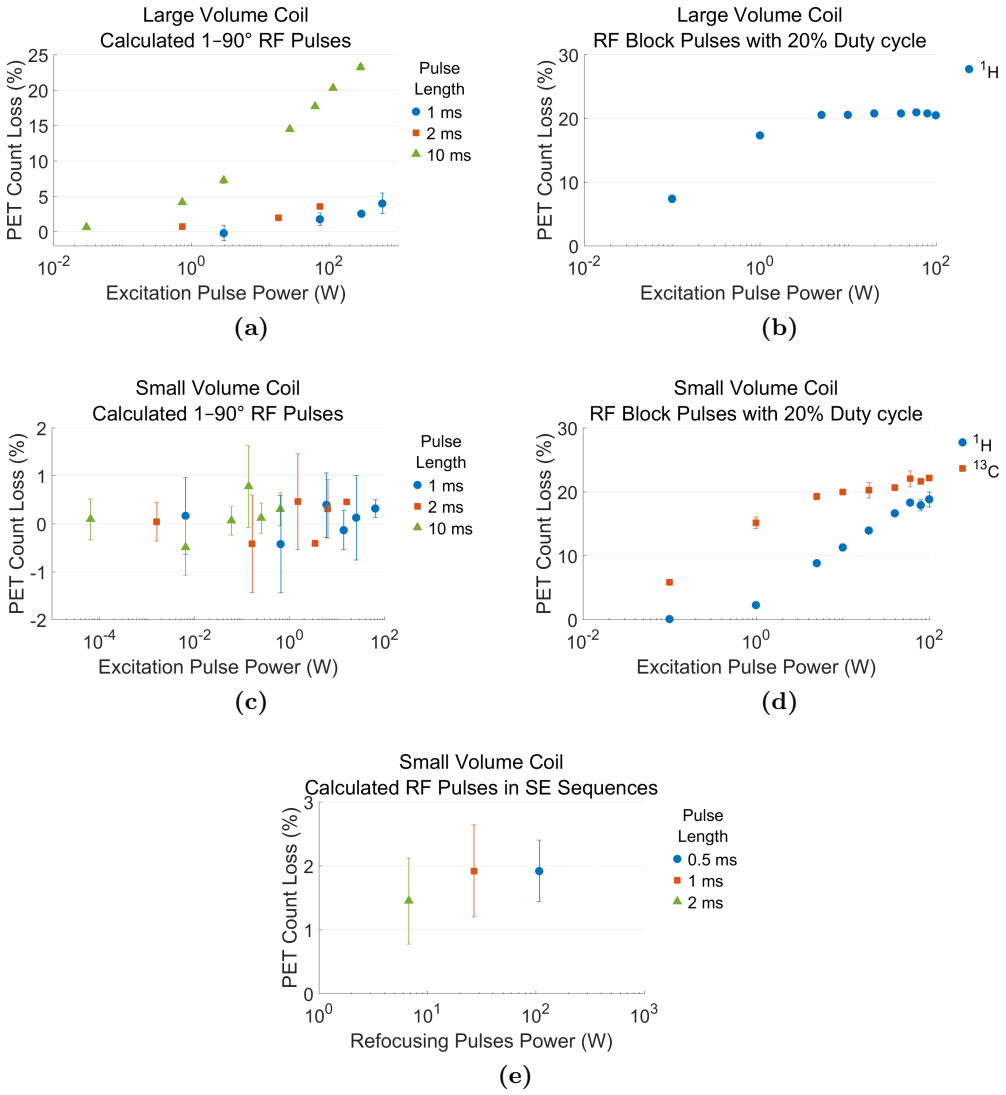

Figure 5.9: PET count losses due to ((a) and (c)) calculated excitation pulses at ^{1}H frequency in GRE sequences, ((b) and (d)) block pulses with 20% duty cycle, and (e) 90° excitation pulses and 180° refocusing pulses in SE sequences at ^{1}H frequency using the two RF volume coils. The X axis of the plots is shown in logarithmic scale. Error bars show the SD of three repeated measurements.

in count losses up to 20%, equal to the used RF duty cycle, while at lower powers, a power-dependent count loss is observed.

Using 80 W RF block pulses in the 30 min measurement with the large volume coil resulted in an additional loss of total prompt coincidences. Immediately after the start of the MR sequence, the total prompt counts started to decrease with a rate of 787 counts per min, which corresponds to 0.32% of the total prompt counts at the start of the MR sequence. The 511 keV photo-peak position (ToT pulse length) showed a reduction during this 30 min period, in both of the inner- and outer-layer SiPMs, indicating SiPM gain change with an increase in the temperature. With the small volume coil, the number of total prompt coincidences did not show a change in the first 5 min of the 30 min MR sequence with 80 W RF block pulses. However, after the first 5 min, it started to decrease with a rate of 463 count per min, corresponding to 0.31% of the total prompt counts at the start of the MR sequence. Furthermore, the 511 keV photo-peak position only changed in the inner-layer SiPMs, indicating an increase in the temperature. No change was observed in the photo-peak position of the outer-layer SiPMs in this configuration.

5.3.6 Effects of the gradient fields switching

The effect of using RF-disabled EPI sequences with intensive gradient fields switching on PET count rate is shown in figure 5.10a, for three directions of gradient readout. The observed count losses were small in all tested sequences and no notable dependency on gradient duty cycle or slew rate was observed. The largest count losses were observed with a gradient duty cycle of 60% and gradient readout in X direction, with an average of 1.1% compared to no MR sequence running. Additionally, the effect of gradient fields switching on the temperature of an SiPM PCB from the outer layer is shown in figure 5.10b. The largest temperature variations correspond to gradient readout in X direction, where a temperature increase of 0.3 K min^{-1} can be observed. In all three gradient readout directions, no temperature increase was observed with gradient duty cycles below 48%.

5.3.7 Attenuation and scattering effects

Comparing the PET images of the ^{18}F uniform phantom with and without the small volume coil inside the insert in figure 5.11 shows no image quality degradation or artifacts caused by the presence of the coil in the PET insert. A 9.1% drop in the

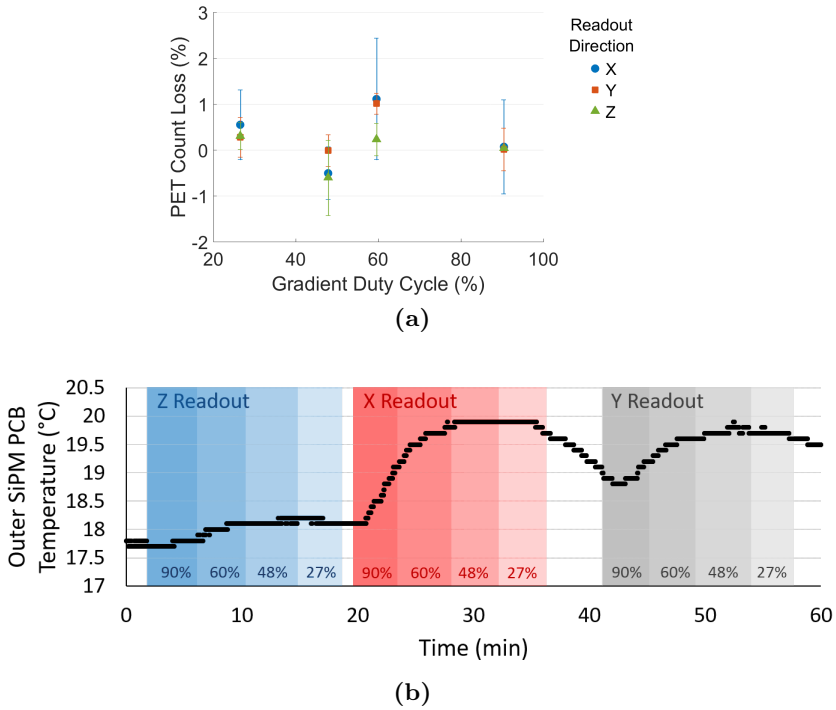

Figure 5.10: The effects of gradient fields switching in EPI sequences on (a) PET count rate and (b) temperature of the SiPM PCBs. The gradient duty cycles (%) are also shown along the time axis, for X, Y, and Z gradient readout directions. Error bars show the SD of three repeated measurements.

mean prompt counts is observed due to the attenuation effect, which is also discernible in the line profiles through the two images shown in figure 5.11. This can be corrected by including the attenuation map of the coil in the PET image reconstruction.

5.4 Discussion

5.4.1 Effects of PET on MRI

Size and tissue composition of the object that is placed inside the RF coil affect the impedance of the coil, and subsequently the amount of RF energy received by the imaged object and the amount of RF signal received by the coil from the object. In tunable RF coils, to achieve an optimal SNR in the image, every time the composition of the objects inside the coil changes, the coil has to be tuned and matched. This is usually performed by adjusting two sets of capacitors from the transmitter and receiver circuitry, so that the reflected RF power from the coil is minimized at the resonance frequency of the imaged nucleus. In this process, the matching capacitor is adjusted to match the impedance of the RF coil, with the objects inside it, to the impedance of

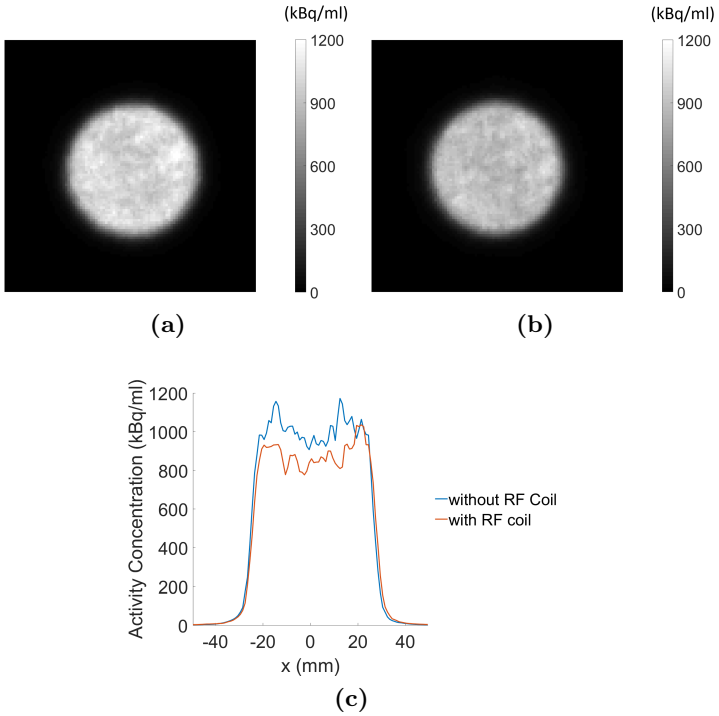

Figure 5.11: PET images obtained with the ^{18}F uniform phantom (a) without and (b) with the small volume coil inside the insert. (c) Horizontal line profiles passing through the centers of the two images are additionally compared. A slice thickness of 1.1 mm was used for the images. The data was decay corrected and images were smoothed with a Gaussian filter with FWHM of 1 mm and are shown in the same intensity scale.

the coil transmission lines. Improper impedance matching leads to reflection of the RF power to the transmission lines and reduced RF transmission to the imaging object. The tuning capacitor, on the other hand, has to be adjusted to tune the resonance frequency of the coil to maximize the coil transmission and reception sensitivity at that frequency.

One of the main issues when using the large volume coil with the PET insert was the coil tuning and matching. This could be due to the presence of the 1.5 m-long coaxial cables connected to the PET detectors and their proximity to the large volume coil circuitry and transmission lines, resulting in a capacitive coupling effect and significant change in the impedance of the coil. Therefore, the dynamic range of the tuning and matching capacitors of the coil was no longer sufficient to perform the tuning and matching properly. The output of the spectrometer used for monitoring the tuning and matching process is shown in figure 5.12. With the PET insert, the coil had to be

either tuned at the ^{1}H resonance frequency with ∼20% reflected power or matched for a different resonance frequency. The consequences of this effect can be observed in the results obtained with the large volume coil for B_1 mapping, the noise scans, and the image quality of the MR sequences. The current design with the coaxial cables can be improved by use of custom made cable traps to minimize the effects on coil tuning and coupling (Seeber et al., 2004).

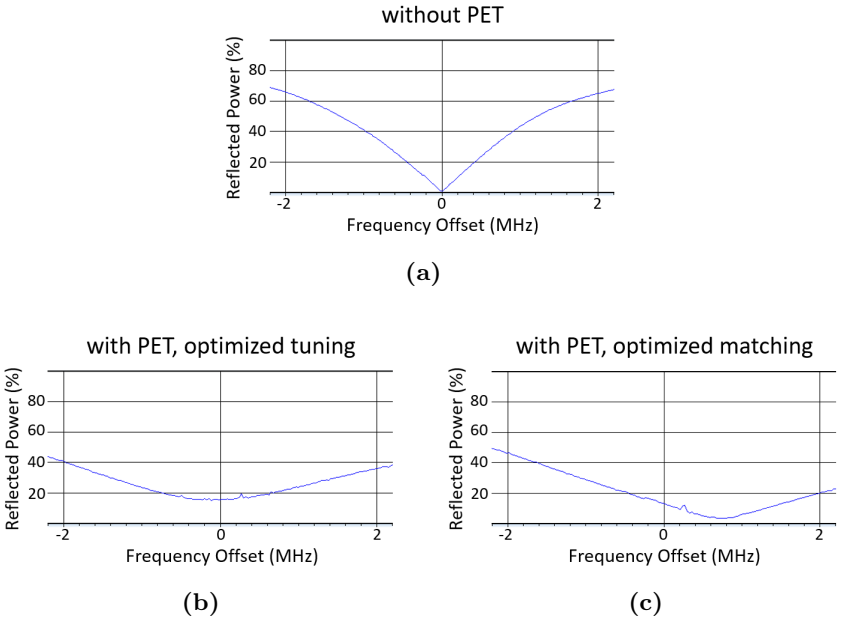

Figure 5.12: Frequency spectra obtained with the spectrometer connected to the large volume coil during the tuning and matching process (a) without the PET insert and ((b) and (c)) with the insert inside the coil optimized for tuning and matching, respectively.

The material and the position of the objects placed inside the coil also affect the amount of RF power required to produce a certain flip angle, due to RF attenuation. For imaging the 550 ml phantom with the large volume coil, the reference power required for a 1 ms block pulse to produce a 90 degree flip angle was 1.7 W without the PET insert and 12.5 W with the insert inside the coil. Similarly, for imaging the 50 ml phantom with the flexible surface coil, the reference power was 13.3 W without the insert and 83.6 W with the insert. This effect further limited the performance of the large volume coil with the insert, as 90° and 180° RF pulses required substantially larger powers or pulse durations when the insert was inside the coil.

Regarding the static field homogeneity, significant changes in the field homogeneity were observed due to the presence of the PET insert, with the large phantom volume and especially towards the edges of the phantom. The largest disturbance in

the field was observed at the top corners of the field maps, which correspond to the location of the cable connectors on the detector PCBs. This is due to the presence of a thin ferromagnetic metallic plate on these connectors, which protects the connections of the micro coaxial cables to the connector. Automatic volume shimming up to 2nd order compensated for most of the inhomogeneities in the defined shimming volume. However, the large field disturbance in proximity of the connectors was not fully compensated. Although the location of the field inhomogeneities caused by these connectors was outside the PET/MR imaging FOV, some field disturbance effects from it extended to the edges of the FOV, resulting in B_0 field variations larger than 1.09 ppm at radial distances larger than 35 mm from the center. This problem can be solved easily in future designs by replacing the ferromagnetic metallic plate on the connectors with a material with low magnetic susceptibility. In case of the small volume coil, due to the distance of the PET components from the imaging volume, the shimming was completely effective through the whole phantom volume and the changes in the static field were negligible and within ± 0.3 ppm in the imaging FOV. In conclusion, in both RF volume coil configurations used with the PET insert, B_0 field homogeneity after shimming was sufficient for most MR imaging sequences. Use of some advanced MR sequences, which are extremely sensitive to B_0 field changes, are limited in the current setup to a small volume close to the iso-center of the scanner. Additionally, it has been shown that the static field homogeneity can be further improved by optimized manual shimming and addition of solid shim plates on the PET gantry (Kolb et al., 2012).

The presence of the PET insert inside the large volume coil had a small effect on the normalized distribution of the B_1 field. However, the main effect was an overall 64% reduction in the B_1 field strength. To explain this reduction, additional B_1 field maps were acquired without the PET insert, while the coil was detuned and dematched in such a way that the reflected power spectra for both channels of the coil were similar to the case where the presence of the PET insert inside the coil caused detuning and dematching. The results showed that the B_1 field strength reduction was partly due to poor tuning and matching of the coil (less than 10%), but mainly due to RF attenuation by the insert components, which resulted in lower RF transmission to the phantom at the ^{1}H resonance frequency. Although no shielding components were used for the insert, the observed RF attenuation by the PET components could be due to the presence of PET coaxial cables, the high packing fraction of the SiPM PCBs (with $\sim$0.1 mm gaps between the PCBs), the 35 μm-thick copper surfaces defined on them

for the bias voltage, and the use of two sets of SiPM PCBs for individually reading the two layers of crystals. Slightly larger inhomogeneities, observed at the edges of the B_1 maps with the insert, could be due to the variations in the B_0 field in close proximity of the insert components. With the small volume coil, the largest differences observed in the B_1 field were observed at the corners of the maps. Comparing the maps obtained in axial slices shows that the these differences are due to a rotational offset in the placement of the small volume coil and are caused by the close proximity of the bird cage coil elements to the phantom. By excluding these areas from the maps, the differences at corresponding locations between the B_1 maps obtained without the insert and with it acquiring were small and within $\pm 5\%$.

Comparing the results of the RF noise scans between the different coil configurations also points to the problem of coil tuning and matching with the large volume coil, where the noise level is increased with the PET insert even when the readout electronics are off. Furthermore, the relative increase in the noise level, when the PET acquisition is on, is significantly lower with the small volume coil, which is due to the copper foils used on the outer layer of the coil for EMI-shielding. The lack of any shielding material in the insert and its readout electronics has a larger effect on the noise picked up by the large volume coil, since the insert is placed inside the coil where the RF receivers are sensitive and unshielded.

The frequency spikes observed on the noise spectra with the insert acquiring could result in zipper artifacts in the MR images, when the receive BW is large enough to include them. The contrast of the zipper artifact in the image depends on the height of the spikes and its ratio to the received signal. In the presented results, the zipper artifacts are only observed in the images with the large volume coil and the 550 ml phantom, where the received signal was low due to coil detuning and the first large spike located 31.5 kHz from the central frequency, which corresponds to a 31.5 mm distance from the center of the phantom. The spikes farther away from the central frequency could result in additional zipper artifacts in images, when larger receive BWs are used. These large receive BWs could be used with EPI sequences to avoid spatial distortions in the image, in sequences requiring short echo times or a fast repetition time, or in imaging scenarios where fat and water pixels in an image may be shifted in space relative to each other due to chemical shift artifacts.

Frequency spikes observed at the central frequency in figures 5.5a and 5.5c, were not expected, particularly in absence of the PET insert, since the RF transmit power was set to zero. However, by setting the transmit power to zero in the Paravision software, the RF amplifier was not turned off. Instead, an attenuation factor of -70 dB was introduced to the excitation pulse peak. Since the MR phantoms were still inside the scanner during these measurements, the peaks observed at the central frequency in figures 5.5a and 5.5c are expected to be the signal in response to the small remaining RF excitation pulse sent by the coil. With the large volume coil in the presence of the PET insert, the peak was absent due to coil detuning and RF attenuation by the PET insert. In the case of the small volume coil operated at ^{13}C frequency, absence of the peak is due to the fact that the noise scans were acquired while the Dotarem phantom was still inside the scanner and thus no signal was expected at ^{13}C frequency from this phantom.

The results of the B_0 and B_1 field maps, the RF noise scans, and the coil tuning explain the image quality observed with different coil configurations. To understand the effects of the PET insert on SNR of the MR images, the SNR values are plotted for different sequences tested with all the three coils used for RF reception in figure 5.13. Furthermore, the mean value of the signal, normalized to the receiver gain, is plotted for each coil and shown next to the corresponding SNR plot of the coil. With the small volume coil and the flexible surface coil, the presence of the insert and its acquisition mode had negligible effect on the received signal. The SNR loss observed with these two coils is solely due to the increased noise due to the presence of unshielded PET electronics. However, due to the proximity of the phantom to the RF coil, the received signal was strong and the SNR values were sufficiently high that the presence of the insert did not cause visually discernible image quality degradation in the images. The use of the insert in the current configuration with small animals could cause more notable effects in imaging areas with low SNR.

With the large volume coil used for RF reception, a ∼60% drop in the MR signal was observed due to coil detuning and RF attenuation by the PET insert components, which resulted in a larger SNR degradation compared to the other two coil configurations. As expected, operating the insert inside the MRI scanner did not show an effect on the received signal. The SD of the background ROIs, corrected for the receiver gain, is also plotted for the large volume coil as a measure of noise, where the significant SNR loss with this coil is explained by the ∼200% increase in the noise when the

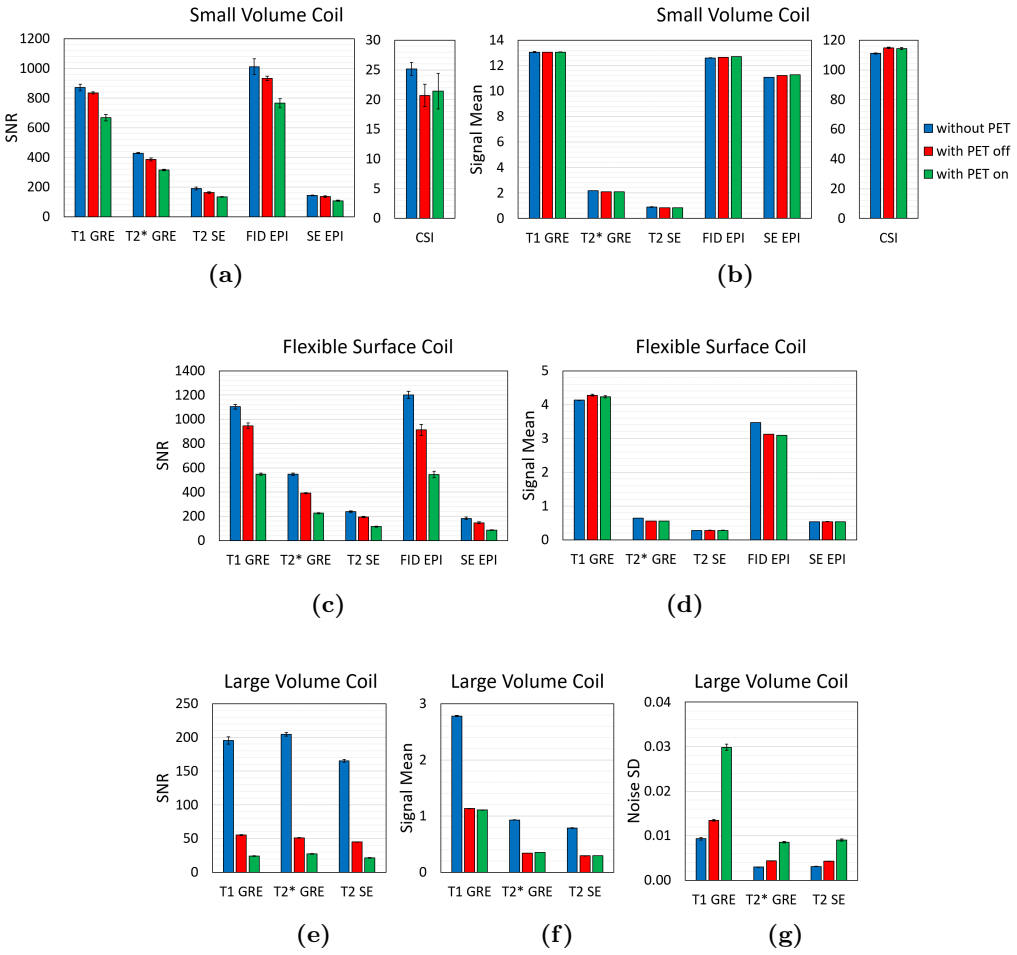

Figure 5.13: Effect of the PET insert on (a) SNR and (b) signal mean value obtained with the small volume coil, (c) SNR and (d) signal mean obtained with the flexible surface coil, and (e) SNR, (f) signal mean, and (g) noise SD obtained with the large volume coil for different sequences. Signal and noise values were normalized according to the receiver gain used for each scan.

PET insert is on. The presence of the insert did not introduce any distortions in the GRE and SE images and the patterns of intensity variations observed in the T2* GRE and T2 SE images were due to the B_1 field inhomogeneities present regardless of the presence of the insert.

The distortions and artifacts observed in EPI images obtained with the 550 ml phantom, in absence of the PET insert, could be partly associated with B_0 field inhomogeneities. At high field strengths such as 7 T and at larger distances from the iso-center, the field inhomogeneities are increased. The presence of the PET insert introduced large inhomogeneities in the B_0 field, which were not fully compensated by

shimming particularly close to the edges of the FOV. Additionally, even small eddy currents induced by rapidly switching gradient fields in the SiPM PCBs could have generated local magnetic field variations, which interfered with the gradient fields close to the PCBs. Since the phantom had a large diameter, B_0 field inhomogeneities and disturbed gradient fields in close proximity of the SiPM PCBs may have resulted in intensified artifacts in EPI images. Furthermore, automatic k-space trajectory adjustments require adequate SNR and may have failed in presence of the PET insert due to increased noise and decreased signal. This effect of SNR on trajectory adjustments could also explain the increased artifacts in EPI images in presence of the PET insert with the surface receive coil. SNR and trajectory adjustments would improve when using higher number of averages, resulting in longer acquisition times.

5.4.2 Effects of MRI on PET

The 9 μm-thick copper layer placed on the small volume coil provided sufficient RF attenuation for using standard GRE sequences at ^{1}H frequency with the PET insert. The shielding effectiveness was partly due the signal composition of calculated RF pulses, which have a shape similar to a truncated sinc function. The contribution of high-power RF waves in this type of excitation is low compared to block pulses, in which the transmitted RF pulses have a constant power during the whole transmission time. This effect can be clearly observed in comparing figures 5.9c and 5.9d, where significant PET count losses start to appear with 1 W block pulses at ^{1}H frequency, and the count losses become equal to the RF duty cycle at 100 W. Furthermore, since long RF pulses require lower peak pulse amplitude to achieve the same flip angle, the signal fluctuations caused by these long pulses on the PET detector signal had a very small amplitude. Because the SiPMs used in the PET insert had a high gain and the threshold used for the time stamps and event validation were high compared to the thresholds used for SiPMs with lower gains, the effects from the RF pulses were further reduced with GRE sequences. With SE sequences with multiple echos, as the number of echos per repetition time increase, the effective RF duty cycle becomes higher than the ratio of the pulse length to the repetition time. Therefore, an increase in PET count losses is observed with the SE sequences compared to GRE sequences. The same effect can be expected in multi-slice GRE sequences, in which the effective RF duty cycle is increased by the number of slices, if the repetition time is held constant.

The effect of the excitation pulse power of calculated RF pulses on count rate can be observed in figure 5.9a, where no EMI-shielding was present. Additionally, the count loss effects from the RF block pulses at ^{13}C frequency with the small volume coil, shown in figure 5.9d, are very similar to the RF block pulses at ^{1}H frequency with the large volume coil, shown in figure 5.9a, which demonstrates an insufficient EMI-shielding at 75.5 MHz frequency.

Using high-power high-duty cycle RF pulses with the large volume coil could introduce more prompt coincidence losses in long sequences, due to temperature increase introduced by these pulses in the absence of a cooling system. The temperature increase observed in both layers in this configuration is expected to be a direct result of power deposition in the SiPM PCBs, considering the short distance (5 mm) between the resonator elements of the coil from the outer surface of the PET insert and the absence of a shielding structure for the SiPM PCBs. With the small volume coil, because the coil was shielded inside the PET insert and the coil resonators were located at a larger distance (28 mm) from the inner surface of the PET insert, the 80 W RF block pulses were substantially attenuated at the location of the SiPMs. Therefore, the gain variation and temperature increase observed in the inner-layer SiPMs in this case could be also due to the heat produced in the copper shielding layer on the small volume coil. The total additional relative prompt count loss rate in this case could be explained by the relatively high detection probably of the 511 keV photons in the inner-layer crystals. Since most of the coincidences in the system are expected to include at least one inner-layer crystal, count losses in this layer would have larger effect on the total detected prompt counts. However, since the SiPMs used in the system had a breakdown voltage temperature coefficient of $\sim$15 mV K^{-1}, the gain variations in both coil configurations were relatively small and the observed relative prompt count loss per min was 0.3% of the initial prompt counts at the beginning of the MR sequence. Considering that the studied case was a demanding sequence using 80 W block pulses with 20% duty cycle, it can be expected that, in the case of commonly used MRI sequences that use calculated-shape RF pulses, the temperature variations would be substantially smaller and would not cause substantial count losses with both volume coils.

The PET count rate variations during the switching of the gradient fields, up to 90% gradient duty cycle, were only slightly higher than the variations without running any MR sequence. This was a direct result of avoiding complete power planes in the design of the SiPM PCB layers. The SiPM PCBs and the copper surface defined for the

common bias voltage are shown in figure A.3 of the supplementary material. The current design could be further optimized to reduce the eddy currents. Additionally, other shielding materials, such as carbon fiber composites, which offer lower eddy currents, could be investigated for replacing the copper layer used on the small volume coil. The most significant effect from the EPI sequences on PET was the introduced temperature variations in the MRI bore, which were larger for gradient readout in X direction and high gradient duty cycles. This leads to SiPM gain variations and subsequently count losses, which could limit the performance of the current system in long EPI acquisitions, with duty cycles higher that 48%, due to lack of a cooling system for the PET insert.

5.4.3 Comparison to other systems

The MR-compatibility studies on PET/MR systems have demonstrated that the magnetic susceptibility artifacts due the presence of the PET insert can be avoided by proper material choice, and compensated significantly by shimming. The two main sources of interference in PET/MR systems have been the RF interferences and the consequences of eddy currents caused by fast switching gradient fields. Several shielding enclosure designs have been tested for the PET inserts in different MRI field strengths. EMI-shielding design was a more challenging task for PET systems that contained active electronic components inside the MRI bore. Copper was the most commonly used material for EMI-shielding of PET/MR systems, and it was tested in form of solid sheets, segmented sheets, or sheets containing slits and vias (Catana et al., 2008, Judenhofer et al., 2008, Wehrl et al., 2011, Maramraju et al., 2011, Kolb et al., 2012, Yoon et al., 2012, Weirich et al., 2012, Hong et al., 2012, Weissler et al., 2014, Kang et al., 2015, Olcott et al., 2015, Grant et al., 2017). Although many of the copper shielded systems demonstrated good RF shielding and minimized the interference of MRI on PET, degradations were observed on MRI mainly attributed with eddy currents in the shield and the noise introduced by the power lines. The shielding efficiency was studied for APD-based PET scanners by changing the thickness, the placement, the number of layers, and making slots in the copper shielding (Peng et al., 2010) and also using carbon fiber composites (Peng et al., 2014), leading to significant improvements in reducing these errors. Carbon fiber composites have been shown to be promising shielding materials for PET/MRI systems, by particularly decreasing the eddy currents compared to copper shields (Gross-Weege et al., 2018). Carbon fiber shielding structures have been used successfully in a preclinical SiPM-based PET in-

sert for a 3 T MRI, in which the SNR degradation was reduced to 2–15% with different sequences, and ghosting artifacts caused by eddy currents were limited to demanding EPI sequences with gradient readout in axial direction (Wehner et al., 2015). However, under certain conditions, ∼7% PET sensitivity loss and degradation in energy resolution (10%) and time resolution (14%) were still observed with the system (Weissler et al., 2015, Wehner et al., 2015). Another SiPM-based small animal PET insert using carbon fibers with additional copper foil was successfully tested in a 7 T MRI system and showed excellent MR-compatibility, reporting 9% SNR degradation using an EPI sequence and negligible effects with other tested sequences (Thiessen et al., 2016).

Developing PET inserts that can be placed inside the RF volume coil of the MRI system is a more challenging task, since the RF field attenuation in the PET insert components and its shielding requires more RF transmit power and introducing gaps between PET detector modules to allow RF transmission is not optimal for PET sensitivity and image reconstruction. Three systems have been developed and characterized based on this approach for 3 T MRI scanners, in which gaps were made between shielded PET modules. Two of these systems used 31 mm and 54 mm-long optical fibers to transport the scintillation light to the SiPMs, in order to introduce large gaps between the shielded PET front-end modules (Hong et al., 2012, Kang et al., 2015). Using this configuration, the gap between the crystal blocks was minimized to not compromise the sensitivity. However, the thickness of the PET ring was substantially increased and the PET performance was degraded due to 40% light loss in the optical fibers. Both of these PET inserts used copper plates for shielding the PET electronic modules placed inside MRI scanner. The built-in MRI body coil was used for RF transmission and a surface receive coil was used for RF reception. Despite the presence of large gaps between the shielded modules, significant reduction in the B_1 field strength was reported. Although the interference between MADPET4 and MRI system was larger compared to these two systems due to lack of shielding, MADPET4 offered better PET performance and optimized PET ring thickness. However, in this configuration, use of all tested sequences was still possible and images obtained in this configuration with the surface receive coil had adequate SNR and image quality in presence of MADPET4. In addition to the presented phantom results, two successful *in vivo* simultaneous PET/MR acquisitions, performed on mouse heart and brain, were previously shown in this configuration (Omidvari et al., 2017a). The third scanner design used a novel approach to relay the SiPM signal out of MRI by electro-optical coupling (Olcott

et al., 2015). Copper plates with slits and vias were used for shielding the PET detector modules, electrically floating relative to MRI RF ground. Although the gaps between shielded modules were ∼1 mm, there were still compromises in terms of PET sensitivity since the gaps between crystal blocks were ∼11 mm. This PET insert was characterized inside the MRI scanner, using the built-in MRI body coil for RF transmission and reception. The electrically floating shielded modules allowed efficient RF transmission and uniform B_1 field maps were obtained. The first results showed SNR losses of 38% with GRE, 48% with SE, and 48% with EPI sequences (Olcott et al., 2015). Furthermore, ghosting artifacts were observed on EPI images obtained with the insert inside the coil (Olcott et al., 2015). In a more recent study from the same group, further developments in the system resulted in 19.5% contrast-to-noise (CNR) loss with GRE and 29.8% CNR loss with FSE sequences (Grant et al., 2017). However, ghosting artifacts and distortions were reported in the EPI studies performed with a resolution phantom, regardless of the presence of the PET insert. Comparing these results to the ones obtained with MADPET4 inside the large volume coil, used for RF transmission and reception, shows substantial B_1 field attenuation and signal loss with MADPET4, even though the detector modules were not shielded and no ground planes were used on the SiPM PCBs. However, while comparing MADPET4 to this system, it is important to also consider the difference in the B_0 field strength and the higher shielding effectiveness of the 35 μm-thick copper surface used in MADPET4 PCBs at 300 MHz frequency. Further studies are required to investigate the causes for the RF field attenuation in this configuration.

The previous PET inserts designed based on SiPM charge transfer approach included a small animal insert using 1.2 m micro coaxial cables tested in a 0.3 T magnet (Yamamoto et al., 2011), a small animal PET insert for a 7 T MRI (Kang et al., 2011) and a human brain PET insert for a 3 T MRI (Hong et al., 2013) both using 3 m flexible flat cables for charge transfer, and a small animal insert for a 3 T MRI scanner, in which the preamplifiers were placed 15 cm from the detector passive components (Ko et al., 2016b). In the first design, the low magnetic field strength, lack of EM shielding material in the PET ring, and the copper foil shielding of the RF coil resulted in significant RF interference in both modalities (Yamamoto et al., 2011). The MR-compatibility of the second design was not evaluated in detail with the 7 T MRI scanner (Kang et al., 2011). However, the same concept was used with a 3 T MRI with the human brain PET insert developed by the same group, in which 0.1 mm-thick

gold plated conductive fabric tape was used for EMI-shielding of the PET insert, and the flexible cables were shielded by 0.24 mm-thick aluminum mesh sheets (Hong et al., 2013). This system showed slight degradation in PET time resolution and significant SNR losses (53–80%) were observed in the MR images obtained with GRE and SE sequences. Furthermore, the system was not tested with more demanding imaging sequences. The last insert, from a more recently published work, showed very promising results in terms of performance and MR-compatibility with a 3 T MRI system (Ko et al., 2016b). A 1 mm-thick carbon fiber tube was used for shielding the PET insert, with a front cap coated by a 30 μm copper film and a 1 mm-thick rear cap from aluminum. The insert was tested with commonly used MR imaging sequences demonstrating up to 9% PET count loss and up to 10% SNR loss in MR images.

The 9 μm-thick copper shield used on the small volume coil in this study could provide approximately 70% RF attenuation for ^{13}C and 91% for ^{1}H frequency, because the skin depth of copper is 3.76 μm at 300 MHz frequency and 7.50 μm at 75.5 MHz. Although the PET insert and its electronics that were placed next to the MRI bore were not shielded, the SNR losses in all tested MR sequences were 23–30% with the small volume coil inside the PET insert. Proper EMI-shielding of the readout electronics, placed outside the MRI scanner, and improving the electrical connections to the MR control room through the MR Faraday cage could feasibly reduce the noise in MR images without any additional interference between the PET and MRI systems. Furthermore, two recently published studies on EMI-shielding designs for PET/MRI systems have shown very promising results by testing a phosphor bronze mesh in a 3 T system (Lee et al., 2018) and an optically transparent stainless steel wire mesh in a 7 T MRI system (Parl et al., 2017). Both shield materials have shown good RF attenuation and low eddy current performance, and seem to be very promising candidates for shielding the components that are placed inside the MRI bore. Incorporation of these shielding materials in the insert could resolve the remaining count rate issues with RF block pulses.

5.5 Conclusion

The MR-compatibility assessment of MADPET4 using three RF coil configurations demonstrated the advantages of using individually read-out high-gain SiPMs and SiPM charge transfer with coaxial cables. A direct advantage of this design is the optimized thickness of the PET ring and no compromise in PET sensitivity and image quality.

Although, in the charge transfer approach, the analog SiPM signal is more exposed to electromagnetic interference prior to digitization, the effect of interference can be significantly reduced by using high-gain SiPMs. By placing the active electronic components far from the imaging FOV, the material and thickness of the shielding for the PET insert can be optimized for the resonance frequency of the RF coil, while minimizing the eddy currents.

Although the PET insert prototype used in this study and its readout electronics were not shielded for electromagnetic interference, the 9 μm-thick copper shield used on the small volume coil provided sufficient shielding for retaining good image quality with all tested MR sequences, including a T1-weighted GRE, a T2*-weighted GRE, a T2-weighted SE, an SE-EPI, an FID-EPI, and a CSI sequence. The two tested EPI sequences did not show any discernible distortions due to the presence of the insert. Simultaneous use of the current prototype with long and demanding EPI sequences is limited due to large temperature variations inside the MRI bore and lack of cooling components for the PET insert. Additionally, the increased noise in MR images could limit the use of the insert with some low-SNR sequences. The effects of GRE, SE, and EPI sequences on PET count rate was sufficiently small that it did not influence the PET image quality. However, using the PET insert simultaneously with high-power block pulses in some MR spectroscopy sequences would degrade the PET image quality due to count losses. Using the PET insert enclosed by the large volume coil was limited due to the high reference power, coil detuning caused by the 1.5 m-long PET coaxial cables, RF attenuation by PET components, and the RF interference with PET detectors resulting in PET count losses due to lack of EMI-shielding. In this configuration, MR imaging was limited to T1-weighted anatomical reference imaging of rat-sized objects with significant SNR loss. However, SNR loss was mitigated when using a surface receive coil and all tested imaging sequences could be used for specific rat-organs or mouse imaging.

Proper EMI-shielding of the readout electronics, improving the electrical connections to the MR control room through the MR Faraday cage, and designing cables traps for the coaxial cables connected to the SiPMs are the future steps for the current prototype, which will improve the noise in the MR images with no subsequent impact on other aspects of both modalities. Furthermore, the effects of MRI on shielded FEB/A boards has to be investigated to reduce the length of coaxial cables used for SiPM charge transfer to avoid degradation of the system time resolution. Recently devel-

oped shielding structures based on carbon fiber, phosphor-bronze mesh, and stainless steel wire mesh seem to be promising candidates for the future designs to minimize the RF interferences on PET and eliminate the PET count losses during MR sequences using high-power RF pulses with high RF duty cycles.

Chapter 6

Conclusions and outlook

This dissertation has presented a comprehensive study on use of two offset layers of scintillation crystals, one-to-one coupled to high-gain SiPMs, in a small animal PET insert for a 7 T MRI system. Although the primary advantage of the one-to-one coupling approach is high count rate performance, it has been shown that this approach is also particularly effective for employing the spatial resolution potentials of the detectors for efficient photon detection. This is demonstrated by the 82% recovery coefficient obtained for the 2 mm-diameter hot rod of the NEMA NU 4 image quality phantom. Furthermore, clear delineation of the mouse myocardium in the *in vivo* ^{18}F-FDG scan confirms the high resolution performance of the scanner with low partial volume effects. This feature is especially beneficial for studying tumor heterogeneity in small animals, where partial volume effects make the studies more challenging near the resolution limits of the scanner. High resolution and high count rate performance of a PET insert could be employed together in simultaneous PET/MRI acquisitions to study tumor heterogeneity and subsequently tumor malignancy by measurements of tumor hypoxia and perfusion.

PET performance evaluation results of MADPET4 have demonstrated a good overall performance for the insert, especially when crystal size and scanner geometry are considered and compared to other preclinical systems. The effects of different design and operational parameters have been discussed throughout this dissertation and further improvements are expected in the PET performance of the system by optimization of these parameters in future. Among these parameters, the characteristics of the ASIC used for SiPM signal readout is particularly important, as it can lead to substantial future improvements in different performance aspects of the scanner. The timing performance, charge measurement linearity, power consumption per channel, maximum event rate, and maximum output data rate of the ASIC are important parameters

in characterizing the performance of an ASIC. Additionally, the generated charge by the specific PET detectors used in the scanner must match the dynamic range of the ASIC and its hardware settings. The SiPMs used in MADPET4 had an active area size of 1.2×1.2 mm^2 and were coupled to LYSO crystals with cross section area of 1.5×1.5 mm^2. High PDE and high gain of the SiPMs, in addition to the dimension and high light output of the crystals resulted in an increased signal charge at the output of the detectors compared to many conventional models used in other systems. Although this unusual high gain was beneficial in operating the PET insert in the MRI environment and allowed for transfer of the signal charge with coaxial cables without preamplification, this high signal charge was the source of some incompatibility issues with the ASIC used in the current system for detector signal readout. The dynamic range and the available hardware settings for adjusting the threshold used for event validation were limited in this ASIC, since the ASIC was originally developed for SiPMs with lower output charge. Therefore, the highest threshold level available on the ASIC for event validation was not sufficient for filtering the low energy events and noise with the detectors used in MADPET4. This caused an increased high data rate at the output of the data acquisition system, which limited the count rate performance of the system. However, it is worth to mention that still a good count rate performance was achieved with the insert, with a peak NECR at 65.1 MBq of average effective activity, using an energy threshold of 350 keV. Another consequence of the limited dynamic range of the ASIC was the increased nonlinearity of the ToT readout scheme at high signal charges. This resulted in degradation of the energy resolution of the detectors. Furthermore, the SiPMs could not be operated at their optimum bias voltage due to increased nonlinearity at high over-voltages. Replacing the ASIC with an alternative model, which could offer better linearity and larger dynamic range, could lead to significant improvements in performance of the PET insert in future.

The axial FOV of the PET insert is a primary consideration and challenge for future developments using the one-to-one coupling approach with dual-layer crystals, as the increased number of channels in a axially longer scanner would increase the cost and complexity of the system and its readout electronics. In addition to sensitivity loss and increased noise, the short axial FOV of MADPET4 limits the use of the insert in dynamic studies, where a single bed position is not sufficient for containing multiple organs of the animal. However, sensitivity of high resolution PET scanners using pixellated crystals can be substantially increased by including ICS data in the image

reconstruction. This is of particular interest for systems using the one-to-one coupling approach with dual layer crystals, as the uncertainties in the detector response are reduced by these two features. This could be an interesting future topic of research with the developed system to improve the sensitivity of the scanner, which could be investigated with an alternative ASIC model that is compatible with the MADPET4 detectors and offers better linearity.

The MR-compatibility study performed with MADPET4 in this dissertation demonstrated that using individually read-out high-gain SiPMs and SiPM charge transfer by coaxial cables could significantly reduce the shielding requirements for preclinical PET inserts operated in high-field MRI scanners. A 9 μm-thick cylinder of copper on the RF volume coil, fitting inside the PET insert, provided sufficient EMI shielding for simultaneous operation of the insert with standard MRI pulse sequences. The achieved performance allows using MADPET4 to investigate applications of simultaneous PET/MRI in future small animal studies. Further improvements in MR-compatibility could be also achieved by shielding the PET readout electronics, which are placed outside the MRI bore. Improving the shielding effectiveness for simultaneous use of long block pulses in MR spectroscopy, requires future studies on replacing the 3D-printed light-tight cover of the insert with materials such as carbon fiber composites.

In conclusion, even without the possible future improvements discussed in this chapter, the PET insert developed in this project is ready to be used in simultaneous small animal PET/MRI studies. These studies could include quantitative determination of blood flow and radio-tracer uptake in tumor models or combining PET with novel ^{13}C-hyper-polarized MR measurements.

Bibliography

Abbaszadeh, S., Gu, Y., Reynolds, P. D., and Levin, C. S. Characterization of a sub-assembly of 3D position sensitive cadmium zinc telluride detectors and electronics from a sub-millimeter resolution PET system. *Physics in Medicine & Biology*, 61 (18):6733, 2016. doi:10.1088/0031-9155/61/18/6733.

Ansorge, R. List mode 3D PET reconstruction using an exact system matrix and polar voxels. In *2007 IEEE Nuclear Science Symposium Conference Record*, volume 5, pages 3454–3457, Oct 2007. doi:10.1109/NSSMIC.2007.4436873.

Auffray, E., Frisch, B., Geraci, F., Ghezzi, A., Gundacker, S., Hillemanns, H., Jarron, P., Meyer, T., Paganoni, M., Pauwels, K., Pizzichemi, M., and Lecoq, P. A comprehensive & systematic study of coincidence time resolution and light yield using scintillators of different size and wrapping. *IEEE Transactions on Nuclear Science*, 60(5):3163–3171, Oct 2013. ISSN 0018-9499. doi:10.1109/TNS.2013.2270089.

Auffray, E., Hadj, F. B. M. B., Cortinovis, D., Doroud, K., Garutti, E., Lecoq, P., Liu, Z., Martinez, R., Paganoni, M., Pizzichemi, M., Silenzi, A., Xu, C., and Zvolský, M. Characterization studies of silicon photomultipliers and crystals matrices for a novel time of flight PET detector. *Journal of Instrumentation*, 10(06):P06009, 2015. doi:10.1088/1748-0221/10/06/P06009.

Bailey, D., Townsend, D., Valk, P., and Maisey, M. *Positron Emission Tomography: Basic Sciences*. Springer London, 2009. ISBN 978-1-84628-007-8. doi:10.1007/b136169.

Bao, Q., Newport, D., Chen, M., Stout, D. B., and Chatziioannou, A. F. Performance evaluation of the inveon dedicated PET preclinical tomograph based on the NEMA NU-4 standards. *Journal of Nuclear Medicine*, 50(3):401–408, 2009. doi:10.2967/jnumed.108.056374.

Beltrame, P., Bolle, E., Braem, A., Casella, C., Chesi, E., Clinthorne, N., Leo, R. D., Dissertori, G., Djambazov, L., Fanti, V., Heller, M., Joram, C., Kagan, H., Lustermann, W., Meddi, F., Nappi, E., Nessi-Tedaldi, F., Oliver, J., Pauss, F., Rafecas, M., Renker, D., Rudge, A., Schinzel, D., Schneider, T., Séguinot, J., Solevi, P., Stapnes, S., and Weilhammer, P. The AX-PET demonstrator—design, construction and characterization. *Nuclear Instruments and Methods in Physics Research Section A: Accelerators, Spectrometers, Detectors and Associated Equipment*, 654(1):546 – 559, 2011. ISSN 0168-9002. doi:10.1016/j.nima.2011.06.059.

Berg, E., Roncali, E., Kapusta, M., Du, J., and Cherry, S. R. A combined time-of-flight and depth-of-interaction detector for total-body positron emission tomography. *Medical Physics*, 43(2):939–950, 2016. ISSN 2473-4209. doi:10.1118/1.4940355.

Bergeron, M., Cadorette, J., Tétrault, M.-A., Beaudoin, J.-F., Leroux, J.-D., Fontaine, R., and Lecomte, R. Imaging performance of LabPET APD-based digital PET scanners for pre-clinical research. *Physics in Medicine & Biology*, 59(3):661, 2014. doi:10.1088/0031-9155/59/3/661.

Bieniosek, M. F., Cates, J. W., and Levin, C. S. A multiplexed TOF and DOI capable PET detector using a binary position sensitive network. *Physics in Medicine & Biology*, 61(21):7639, 2016. doi:10.1088/0031-9155/61/21/7639.

Blahuta, S., Bessière, A., Viana, B., Dorenbos, P., and Ouspenski, V. Evidence and consequences of Ce^{4+} in LYSO:Ce,Ca and LYSO:Ce,Mg single crystals for medical imaging applications. *IEEE Transactions on Nuclear Science*, 60(4):3134–3141, Aug 2013. ISSN 0018-9499. doi:10.1109/TNS.2013.2269700.

Brown, R. W., Cheng, Y.-C. N., Haacke, E. M., Thompson, M. R., and Venkatesan, R. *Magnetic Resonance Imaging: Physical Principles and Sequence Design*. Wiley, 2014. ISBN 9781118633953. doi:10.1002/9781118633953.ch1.

Brunner, S. E. and Schaart, D. R. BGO as a hybrid scintillator / Cherenkov radiator for cost-effective time-of-flight PET. *Physics in Medicine & Biology*, 62(11):4421, 2017. doi:10.1088/1361-6560/aa6a49.

Brzeziński, K., Oliver, J., Gillam, J., and Rafecas, M. Study of a high-resolution PET system using a silicon detector probe. *Physics in Medicine & Biology*, 59(20):6117, 2014. doi:10.1088/0031-9155/59/20/6117.

Cabello, J. and Rafecas, M. Comparison of basis functions for 3D PET reconstruction using a Monte Carlo system matrix. *Physics in Medicine & Biology*, 57(7):1759, 2012. doi:10.1088/0031-9155/57/7/1759.

Cabello, J., Oliver, J. F., Torres-Espallardo, I., and Rafecas, M. Polar voxelization schemes combined with a Monte-Carlo based system matrix for image reconstruction in high resolution PET. In *IEEE Nuclear Science Symposuim Medical Imaging Conference*, pages 3256–3261, Oct 2010. doi:10.1109/NSSMIC.2010.5874407.

Cañadas, M., Embid, M., Lage, E., Desco, M., Vaquero, J. J., and Perez, J. M. NEMA NU 4-2008 performance measurements of two commercial small-animal PET scanners: ClearPET and rPET-1. *IEEE Transactions on Nuclear Science*, 58(1):58–65, Feb 2011. ISSN 0018-9499. doi:10.1109/TNS.2010.2072935.

Catana, C., Procissi, D., Wu, Y., Judenhofer, M. S., Qi, J., Pichler, B. J., Jacobs, R. E., and Cherry, S. R. Simultaneous in vivo positron emission tomography and magnetic resonance imaging. *Proceedings of the National Academy of Sciences*, 105 (10):3705–3710, 2008. doi:10.1073/pnas.0711622105.

Cates, J. W. and Levin, C. S. Advances in coincidence time resolution for PET. *Physics in Medicine & Biology*, 61(6):2255, 2016. doi:doi.org/10.1088/0031-9155/61/6/2255.

Chang, C.-M., Cates, J. W., and Levin, C. S. Time-over-threshold for pulse shape discrimination in a time-of-flight phoswich PET detector. *Physics in Medicine & Biology*, 62(1):258, 2017. doi:10.1088/1361-6560/62/1/258.

Cherry, S. R. In vivo molecular and genomic imaging: new challenges for imaging physics. *Physics in Medicine & Biology*, 49(3):R13, 2004. doi:10.1088/0031-9155/49/3/R01.

Cherry, S. R. Multimodality imaging: Beyond PET/CT and SPECT/CT. *Seminars in Nuclear Medicine*, 39(5):348 – 353, 2009. ISSN 0001-2998. doi:10.1053/j.semnuclmed.2009.03.001. Hybrid Imaging Anniversary Issue (Part II).

Cherry, S. R. and Gambhir, S. S. Use of positron emission tomography in animal research. *ILAR Journal*, 42(3):219–232, 2001. doi:10.1093/ilar.42.3.219.

Cherry, S. R., Sorenson, J. A., and Phelps, M. E. *Physics in Nuclear Medicine*. W.B. Saunders, Philadelphia, 2012. ISBN 978-1-4160-5198-5. doi:10.1016/B978-1-4160-5198-5.00018-6.

Christensen, N. L., Hammer, B. E., Heil, B. G., and Fetterly, K. Positron emission tomography within a magnetic field using photomultiplier tubes and lightguides. *Physics in Medicine & Biology*, 40(4):691, 1995. doi:10.1088/0031-9155/40/4/014.

Corsi, F., Marzocca, C., Perrotta, A., Dragone, A., Foresta, M., Guerra, A. D., Marcatili, S., Llosa, G., Collazzuol, G., Betta, G. F. D., Dinu, N., Piemonte, C., Pignatel, G. U., and Levi, G. Electrical characterization of silicon photo-multiplier detectors for optimal front-end design. In *2006 IEEE Nuclear Science Symposium Conference Record*, volume 2, pages 1276–1280, Oct 2006. doi:10.1109/NSSMIC.2006.356076.

Corsi, F., Dragone, A., Marzocca, C., Guerra, A. D., Delizia, P., Dinu, N., Piemonte, C., Boscardin, M., and Betta, G. D. Modelling a silicon photomultiplier (SiPM) as a signal source for optimum front-end design. *Nuclear Instruments and Methods in Physics Research Section A: Accelerators, Spectrometers, Detectors and Associated Equipment*, 572(1):416 – 418, 2007. ISSN 0168-9002. doi:10.1016/j.nima.2006.10.219. Frontier Detectors for Frontier Physics.

Cova, S., Ghioni, M., Lacaita, A., Samori, C., and Zappa, F. Avalanche photodiodes and quenching circuits for single-photon detection. *Appl. Opt.*, 35(12):1956–1976, Apr 1996. doi:10.1364/AO.35.001956.

Dale, B. M., Brown, M. A., and Semelka, R. C. *MRI: Basic Principles and Applications*. Wiley-Blackwell, 2015. ISBN 9781119013051. doi:10.1002/9781119013051.ch1.

Defrise, M., Townsend, D. W., Bailey, D., Geissbuhler, A. M. C., and Jones, T. A normalization technique for 3D PET data. *Physics in Medicine & Biology*, 36(7): 939, 1991. doi:10.1088/0031-9155/36/7/003.

Delso, G., Fürst, S., Jakoby, B., Ladebeck, R., Ganter, C., Nekolla, S. G., Schwaiger, M., and Ziegler, S. I. Performance measurements of the Siemens mMR integrated whole-body PET/MR scanner. *Journal of Nuclear Medicine*, 52(12):1914–1922, 2011. doi:10.2967/jnumed.111.092726.

Drozdowski, W., Dorenbos, P., de Haas, J. T. M., Drozdowska, R., Owens, A., Kamada, K., Tsutsumi, K., Usuki, Y., Yanagida, T., and Yoshikawa, A. Scintillation properties of praseodymium activated $Lu_3Al_5O_{12}$ single crystals. *IEEE Transactions on Nuclear Science*, 55(4):2420–2424, Aug 2008. ISSN 0018-9499. doi:10.1109/TNS.2008.2000845.

Eckert, P., Schultz-Coulon, H.-C., Shen, W., Stamen, R., and Tadday, A. Characterisation studies of silicon photomultipliers. *Nuclear Instruments and Methods in Physics Research Section A: Accelerators, Spectrometers, Detectors and Associated Equipment*, 620(2):217 – 226, 2010. ISSN 0168-9002. doi:10.1016/j.nima.2010.03.169.

España, S., Marcinkowski, R., Keereman, V., Vandenberghe, S., and Holen, R. V. DigiPET: sub-millimeter spatial resolution small-animal PET imaging using thin monolithic scintillators. *Physics in Medicine & Biology*, 59(13):3405, 2014. doi:10.1088/0031-9155/59/13/3405.

Ferri, A., Gola, A., Serra, N., Tarolli, A., Zorzi, N., and Piemonte, C. Performance of FBK high-density SiPM technology coupled to Ce:LYSO and Ce:GAGG for TOF-PET. *Physics in Medicine & Biology*, 59(4):869, 2014. doi:10.1088/0031-9155/59/4/869.

Ferri, A., Acerbi, F., Gola, A., Paternoster, G., Piemonte, C., and Zorzi, N. Performance of FBK low-afterpulse NUV silicon photomultipliers for PET application. *Journal of Instrumentation*, 11(03):P03023, 2016. doi:10.1088/1748-0221/11/03/P03023.

Goertzen, A. L., Bao, Q., Bergeron, M., Blankemeyer, E., Blinder, S., Cañadas, M., Chatziioannou, A. F., Dinelle, K., Elhami, E., Jans, H.-S., Lage, E., Lecomte, R., Sossi, V., Surti, S., Tai, Y.-C., Vaquero, J. J., Vicente, E., Williams, D. A., and Laforest, R. NEMA NU 4-2008 comparison of preclinical PET imaging systems. *Journal of Nuclear Medicine*, 53(8):1300–1309, 2012. doi:10.2967/jnumed.111.099382.

Goertzen, A. L., Stortz, G., Thiessen, J. D., Bishop, D., Khan, M. S., Kozlowski, P., Retiére, F., Schellenberg, G., Shams, E., Sossi, V., and Thompson, C. J. First results from a high-resolution small animal SiPM PET insert for PET/MR imaging at 7T. *IEEE Transactions on Nuclear Science*, 63(5):2424–2433, Oct 2016. ISSN 0018-9499. doi:10.1109/TNS.2016.2576963.

González, A. J., Aguilar, A., Conde, P., Hernández, L., Moliner, L., Vidal, L. F., Sánchez, F., Sánchez, S., Correcher, C., Molinos, C., Barberá, J., Lankes, K., Junge, S., Bruckbauer, T., Bruyndonckx, P., and Benlloch, J. M. A PET design based on SiPM and monolithic LYSO crystals: Performance evaluation. *IEEE Transactions on Nuclear Science*, 63(5):2471–2477, Oct 2016. ISSN 0018-9499. doi:10.1109/TNS.2016.2522179.

Grant, A. M., Deller, T. W., Khalighi, M. M., Maramraju, S. H., Delso, G., and Levin, C. S. NEMA NU 2-2012 performance studies for the SiPM-based ToF-PET component of the GE SIGNA PET/MR system. *Medical Physics*, 43(5):2334–2343, 2016. ISSN 2473-4209. doi:10.1118/1.4945416.

Grant, A. M., Lee, B. J., Chang, C., and Levin, C. S. Simultaneous PET/MR imaging with a radio frequency-penetrable PET insert. *Medical Physics*, 44(1):112–120, 2017. ISSN 2473-4209. doi:10.1002/mp.12031.

Grodzicka, M., Moszyński, M., Szcześniak, T., Ferri, A., Piemonte, C., Szawłowski, M., Gola, A., Grodzicki, K., and Tarolli, A. Performance of FBK high-density SiPMs in scintillation spectrometry. *Journal of Instrumentation*, 9(08):P08004, 2014. doi:10.1088/1748-0221/9/08/P08004.

Gross-Weege, N., Dey, T., Gebhardt, P., Schug, D., Weissler, B., and Schulz, V. Characterization methods for comprehensive evaluations of shielding materials used in an MRI. *Medical Physics*, 2018. ISSN 2473-4209. doi:10.1002/mp.12762.

Gu, Z., Taschereau, R., Vu, N. T., Wang, H., Prout, D. L., Silverman, R. W., Bai, B., Stout, D. B., Phelps, M. E., and Chatziioannou, A. F. NEMA NU-4 performance evaluation of PETbox4, a high sensitivity dedicated PET preclinical tomograph. *Physics in Medicine & Biology*, 58(11):3791, 2013. doi:10.1088/0031-9155/58/11/3791.

Gundacker, S., Auffray, E., Frisch, B., Hillemanns, H., Jarron, P., Meyer, T., Pauwels, K., and Lecoq, P. A systematic study to optimize SiPM photo-detectors for highest time resolution in PET. *IEEE Transactions on Nuclear Science*, 59(5):1798–1804, Oct 2012. ISSN 0018-9499. doi:10.1109/TNS.2012.2202918.

Gundacker, S., Acerbi, F., Auffray, E., Ferri, A., Gola, A., Nemallapudi, M., Paternoster, G., Piemonte, C., and Lecoq, P. State of the art timing in TOF-PET detectors with LuAG, GAGG and L(Y)SO scintillators of various sizes coupled to FBK-SiPMs. *Journal of Instrumentation*, 11(08):P08008, 2016. doi:10.1088/1748-0221/11/08/P08008.

Haase, A., Frahm, J., Matthaei, D., Hanicke, W., and Merboldt, K.-D. FLASH imaging. rapid NMR imaging using low flip-angle pulses. *Journal of Magnetic Resonance (1969)*, 67(2):258 – 266, 1986. ISSN 0022-2364. doi:10.1016/0022-2364(86)90433-6.

Hammer, B. NMR-PET scanner apparatus, July 1990. URL `https://www.google.de/patents/US4939464`. US Patent 4,939,464.

Hennig, J., Nauerth, A., and Friedburg, H. RARE imaging: A fast imaging method for clinical MR. *Magnetic Resonance in Medicine*, 3(6):823–833, 1986. ISSN 1522-2594. doi:10.1002/mrm.1910030602.

Herraiz, J. L., España, S., Vaquero, J. J., Desco, M., and Udías, J. M. FIRST: Fast iterative reconstruction software for (PET) tomography. *Physics in Medicine & Biology*, 51(18):4547, 2006. doi:10.1088/0031-9155/51/18/007.

Hong, K. J., Choi, Y., Jung, J. H., Kang, J., Hu, W., Lim, H. K., Huh, Y., Kim, S., Jung, J. W., Kim, K. B., Song, M. S., and Park, H.-w. A prototype MR insertable brain PET using tileable GAPD arrays. *Medical Physics*, 40(4):042503, 2013. ISSN 2473-4209. doi:10.1118/1.4793754. 042503.

Hong, S. J., Kang, H. G., Ko, G. B., Song, I. C., Rhee, J., and Lee, J. S. SiPM-PET with a short optical fiber bundle for simultaneous PET-MR imaging. *Physics in Medicine & Biology*, 57(12):3869, 2012. doi:10.1088/0031-9155/57/12/3869.

Hsu, D. F., Freese, D. L., and Levin, C. S. Breast-dedicated radionuclide imaging systems. *Journal of Nuclear Medicine*, 57(Supplement 1):40S–45S, 2016. doi:10.2967/jnumed.115.157883.

Hudson, H. M. and Larkin, R. S. Accelerated image reconstruction using ordered subsets of projection data. *IEEE Transactions on Medical Imaging*, 13(4):601–609, Dec 1994. ISSN 0278-0062. doi:10.1109/42.363108.

Inadama, N., Hirano, Y., Nishikido, F., Murayama, H., and Yamaya, T. Development of a DOI PET detector having the structure of the X'tal cube extended in one direction. *IEEE Transactions on Nuclear Science*, 63(5):2509–2516, Oct 2016. ISSN 0018-9499. doi:10.1109/TNS.2016.2599117.

Iwanowska, J., Swiderski, L., Szczesniak, T., Sibczynski, P., Moszynski, M., Grodzicka, M., Kamada, K., Tsutsumi, K., Usuki, Y., Yanagida, T., and Yoshikawa, A. Performance of cerium-doped $Gd_3Al_2Ga_3O_{12}$ (GAGG:Ce) scintillator in gamma-ray spectrometry. *Nuclear Instruments and Methods in Physics Research Section A: Accelerators, Spectrometers, Detectors and Associated Equipment*, 712:34 – 40, 2013. ISSN 0168-9002. doi:10.1016/j.nima.2013.01.064.

Judenhofer, M. S. and Cherry, S. R. Applications for preclinical PET/MRI. *Seminars in Nuclear Medicine*, 43(1):19 – 29, 2013. ISSN 0001-2998. doi:10.1053/j.semnuclmed.2012.08.004. PET/MRI.

Judenhofer, M. S., Catana, C., Swann, B. K., Siegel, S. B., Jung, W., Nutt, R. E., Cherry, S. R., Claussen, C. D., and Pichler, B. J. PET/MR images acquired with a compact MR-compatible PET detector in a 7-T magnet. *Radiology*, 244(3):807–814, 2007. doi:10.1148/radiol.2443061756.

Judenhofer, M. S., Wehrl, H. F., Newport, D. F., Catana, C., Siegel, S. B., Becker, M., Thielscher, A., Kneilling, M., Lichy, M. P., Eichner, M., Klingel, K., Reischl, G., Widmaier, S., Rocken, M., Nutt, R. E., Machulla, H.-J., Uludag, K., Cherry, S. R., Claussen, C. D., and Pichler, B. J. Simultaneous PET-MRI: a new approach for functional and morphological imaging. *Nature Medicine*, 14:459 – 465, 2008. doi:10.1038/nm1700.

Kamada, K., Tsutsumi, K., Usuki, Y., Ogino, H., Yanagida, T., and Yoshikawa, A. Crystal growth and scintillation properties of 2-inch-diameter Pr:$Lu_3Al_5O_{12}$ (Pr:LuAG) single crystal. *IEEE Transactions on Nuclear Science*, 55(3):1488–1491, June 2008. ISSN 0018-9499. doi:10.1109/TNS.2008.924072.

Kamada, K., Yanagida, T., Endo, T., Tsutumi, K., Usuki, Y., Nikl, M., Fujimoto, Y., Fukabori, A., and Yoshikawa, A. 2 inch diameter single crystal growth and scintillation properties of Ce:$Gd_3Al_2Ga_3O_{12}$. *Journal of Crystal Growth*, 352(1):88 – 90, 2012. ISSN 0022-0248. doi:10.1016/j.jcrysgro.2011.11.085. The Proceedings of the 18th American Conference on Crystal Growth and Epitaxy.

Kamada, K., Kurosawa, S., Prusa, P., Nikl, M., Kochurikhin, V. V., Endo, T., Tsutumi, K., Sato, H., Yokota, Y., Sugiyama, K., and Yoshikawa, A. Cz grown 2-in. size Ce:$Gd_3(Al,Ga)_5O_{12}$ single crystal; relationship between Al, Ga site occupancy and scintillation properties. *Optical Materials*, 36(12):1942 – 1945, 2014. ISSN 0925-3467. doi:10.1016/j.optmat.2014.04.001. Selected papers from the 6th International Symposium on Laser, Scintillator and Non Linear Optical Materials (ISLNOM-6). Oct. 20-23, 2013; Galaxy Hotel Shanghai, Shanghai, China.

Kang, H., Hong, S., Ko, G., Yoon, H., Song, I., Rhee, J., and Lee, J. Assessment of MR-compatibility of SiPM PET insert using short optical fiber bundles for small animal research. *Journal of Instrumentation*, 10(12):P12008, 2015. doi:10.1088/1748-0221/10/12/P12008.

Kang, J., Choi, Y., Hong, K. J., Hu, W., Jung, J. H., Huh, Y., and Kim, B.-T. A small animal PET based on GAPDs and charge signal transmission approach for hybrid PET-MR imaging. *Journal of Instrumentation*, 6(08):P08012, 2011. doi:10.1088/1748-0221/6/08/P08012.

Kemp, B. J., Hruska, C. B., McFarland, A. R., Lenox, M. W., and Lowe, V. J. NEMA NU 2-2007 performance measurements of the siemens inveon™ preclinical small animal PET system. *Physics in Medicine & Biology*, 54(8):2359, 2009. doi:10.1088/0031-9155/54/8/007.

Khalil, M. M. *Basic Sciences of Nuclear Medicine*. Springer-Verlag Berlin Heidelberg, 2011. ISBN 978-3-540-85962-8. doi:10.1007/978-3-540-85962-8.

Kim, J. S., Lee, J. S., Im, K. C., Kim, S. J., Kim, S.-Y., Lee, D. S., and Moon, D. H. Performance measurement of the microPET Focus 120 scanner. *Journal of Nuclear Medicine*, 48(9):1527–1535, 2007. doi:10.2967/jnumed.107.040550.

Kimble, T., Chou, M., and Chai, B. H. T. Scintillation properties of LYSO crystals. In *2002 IEEE Nuclear Science Symposium Conference Record*, volume 3, pages 1434–1437 vol.3, Nov 2002. doi:10.1109/NSSMIC.2002.1239590.

Kipnis, I., Collins, T., DeWitt, J., Dow, S., Frey, A., Grillo, A., Johnson, R., Kroeger, W., Leona, A., Luo, L., Mandelli, E., Manfredi, P. F., Melani, M., Momayezi, M., Morsani, F., Nyman, M., Pedrali-Noy, M., Poplevin, P., Spencer, E., Re, V., and Roe, N. A time-over-threshold machine: the readout integrated circuit for the BABAR silicon vertex tracker. *IEEE Transactions on Nuclear Science*, 44(3): 289–297, Jun 1997. ISSN 0018-9499. doi:10.1109/23.603658.

Knoll, G. F. *Radiation detection and measurement*. Wiley, New York, NY, 2010. ISBN 9780470131480.

Ko, G. B., Kim, K. Y., Yoon, H. S., Lee, M. S., Son, J.-W., Im, H.-J., and Lee, J. S. Evaluation of a silicon photomultiplier PET insert for simultaneous PET and MR imaging. *Medical Physics*, 43(1):72–83, 2016a. ISSN 2473-4209. doi:10.1118/1.4937784.

Ko, G. B., Yoon, H. S., Kim, K. Y., Lee, M. S., Yang, B. Y., Jeong, J. M., Lee, D. S., Song, I. C., Kim, S., Kim, D., and Lee, J. S. Simultaneous multiparametric PET/MRI with silicon photomultiplier PET and ultra-high-field MRI for small-animal imaging. *Journal of Nuclear Medicine*, 57(8):1309–1315, 2016b. doi:10.2967/jnumed.115.170019.

Kolb, A., Wehrl, H. F., Hofmann, M., Judenhofer, M. S., Eriksson, L., Ladebeck, R., Lichy, M. P., Byars, L., Michel, C., Schlemmer, H.-P., Schmand, M., Claussen, C. D., Sossi, V., and Pichler, B. J. Technical performance evaluation of a human brain PET/MRI system. *European Radiology*, 22(8):1776–1788, Aug 2012. ISSN 1432-1084. doi:10.1007/s00330-012-2415-4.

Kolb, A., Parl, C., Mantlik, F., Liu, C. C., Lorenz, E., Renker, D., and Pichler, B. J. Development of a novel depth of interaction PET detector using highly multiplexed G-APD cross-strip encoding. *Medical Physics*, 41(8Part1):081916–n/a, 2014. ISSN 2473-4209. doi:10.1118/1.4890609. 081916.

Kuramoto, M., Nakamori, T., Kimura, S., Gunji, S., Takakura, M., and Kataoka, J. Development of TOF-PET using Compton scattering by plastic scintillators. *Nuclear Instruments and Methods in Physics Research Section A: Accelerators, Spectrometers, Detectors and Associated Equipment*, 845:668 – 672, 2017. ISSN 0168-9002. doi:10.1016/j.nima.2016.06.100. Proceedings of the Vienna Conference on Instrumentation 2016.

Kurosawa, S., Shoji, Y., Yokota, Y., Kamada, K., Chani, V. I., and Yoshikawa, A. Czochralski growth of $Gd_3(Al_{5-x}Ga_x)O_{12}$ (GAGG) single crystals and their scintillation properties. *Journal of Crystal Growth*, 393:134 – 137, 2014. ISSN 0022-0248. doi:10.1016/j.jcrysgro.2013.10.059. The 19th American Conference on Crystal Growth and Epitaxy in conjunction with The 16th US Biennial Workshop on Organometallic Vapor Phase Epitaxy.

Kwon, S. I., Gola, A., Ferri, A., Piemonte, C., and Cherry, S. R. Bismuth germanate coupled to near ultraviolet silicon photomultipliers for time-of-flight PET. *Physics in Medicine & Biology*, 61(18):L38, 2016. doi:10.1088/0031-9155/61/18/L38.

Lage, E., Vaquero, J. J., Sisniega, A., España, S., Tapias, G., Abella, M., Rodríguez-Ruano, A., Ortuño, J. E., Udías, A., and Desco, M. Design and performance evaluation of a coplanar multimodality scanner for rodent imaging. *Physics in Medicine & Biology*, 54(18):5427, 2009. doi:10.1088/0031-9155/54/18/005.

Lange, K. and Carson, R. EM reconstruction algorithms for emission and transmission tomography. *J Comput Assist Tomogr.*, 8(2):306–16, 1984.

Lee, B. J., Watkins, R. D., Chang, C., and Levin, C. S. Low eddy current RF shielding enclosure designs for 3T MR applications. *Magnetic Resonance in Medicine*, 79(3): 1745–1752, 2018. ISSN 1522-2594. doi:10.1002/mrm.26766.

Lenox, M. W., Gremillion, T., Miller, S., and Young, J. W. Coincidence time alignment for planar pixellated positron emission tomography detector arrays. In *2001 IEEE Nuclear Science Symposium Conference Record (NSS/MIC)*, volume 4, pages 1952–1954, 2001. doi:10.1109/NSSMIC.2001.1009206.

Levin, C. S. and Hoffman, E. J. Calculation of positron range and its effect on the fundamental limit of positron emission tomography system spatial resolution. *Physics in Medicine & Biology*, 44(3):781, 1999. doi:10.1088/0031-9155/44/3/019.

Liu, Z., Pizzichemi, M., Auffray, E., Lecoq, P., and Paganoni, M. Performance study of Philips digital silicon photomultiplier coupled to scintillating crystals. *Journal of Instrumentation*, 11(01):P01017, 2016. doi:10.1088/1748-0221/11/01/P01017.

Mackewn, J. E., Halsted, P., Charles Edwards, G., Page, R., Totman, J. J., Sunassee, K., Strul, D., Hallett, W. A., Jauregui Osoro, M., Liepins, P., Williams, S. C. R., Schaeffter, T., Keevil, S. F., and Marsden, P. K. Performance evaluation of an MRI-compatible pre-clinical PET system using long optical fibers. *IEEE Transactions on Nuclear Science*, 57(3):1052–1062, June 2010. ISSN 0018-9499. doi:10.1109/TNS.2010.2044891.

Mackewn, J. E., Lerche, C. W., Weissler, B., Sunassee, K., de Rosales, R. T. M., Phinikaridou, A., Salomon, A., Ayres, R., Tsoumpas, C., Soultanidis, G. M., Gebhardt, P., Schaeffter, T., Marsden, P. K., and Schulz, V. PET perfor-

mance evaluation of a pre-clinical SiPM-based MR-compatible PET scanner. *IEEE Transactions on Nuclear Science*, 62(3):784–790, June 2015. ISSN 0018-9499. doi:10.1109/TNS.2015.2392560.

Mann, A. B., Paul, S., Tapfer, A., Spanoudaki, V. C., and Ziegler, S. I. A computing efficient PET time calibration method based on pseudoinverse matrices. In *2009 IEEE Nuclear Science Symposium Conference Record (NSS/MIC)*, pages 3889–3892, Oct 2009. doi:10.1109/NSSMIC.2009.5401925.

Mansfield, P. Multi-planar image formation using NMR spin echoes. *Journal of Physics C: Solid State Physics*, 10(3):L55, 1977. doi:10.1088/0022-3719/10/3/004.

Maramraju, S. H., Smith, S. D., Junnarkar, S. S., Schulz, D., Stoll, S., Ravindranath, B., Purschke, M. L., Rescia, S., Southekal, S., Pratte, J.-F., Vaska, P., Woody, C. L., and Schlyer, D. J. Small animal simultaneous PET/MRI: initial experiences in a 9.4 T microMRI. *Physics in Medicine & Biology*, 56(8):2459, 2011. doi:10.1088/0031-9155/56/8/009.

Marcinkowski, R., Mollet, P., Holen, R. V., and Vandenberghe, S. Sub-millimetre DOI detector based on monolithic LYSO and digital SiPM for a dedicated small-animal PET system. *Physics in Medicine & Biology*, 61(5):2196, 2016. doi:10.1088/0031-9155/61/5/2196.

Mathews, A. J., Komarov, S., Wu, H., O'Sullivan, J. A., and Tai, Y.-C. Improving PET imaging for breast cancer using virtual pinhole PET half-ring insert. *Physics in Medicine & Biology*, 58(18):6407, 2013. doi:10.1088/0031-9155/58/18/6407.

Mora, C. and Rafecas, M. Polar pixels for high resolution small animal PET. In *2006 IEEE Nuclear Science Symposium Conference Record*, volume 5, pages 2812–2817, Oct 2006. doi:10.1109/NSSMIC.2006.356463.

Moskal, P., Rundel, O., Alfs, D., Bednarski, T., Białas, P., Czerwiński, E., Gajos, A., Giergiel, K., Gorgol, M., Jasińska, B., Kamińska, D., Kapłon, L., Korcyl, G., Kowalski, P., Kozik, T., Krzemień, W., Kubicz, E., Niedźwiecki, S., Pałka, M., Raczyński, L., Rudy, Z., Sharma, N. G., Słomski, A., Silarski, M., Strzelecki, A., Wieczorek, A., Wiślicki, W., Witkowski, P., Zieliński, M., and Zoń, N. Time resolution of the plastic scintillator strips with matrix photomultiplier readout for J-PET tomograph. *Physics in Medicine & Biology*, 61(5):2025, 2016. doi:10.1088/0031-9155/61/5/2025.

Nagy, K., Tóth, M., Major, P., Patay, G., Egri, G., Häggkvist, J., Varrone, A., Farde, L., Halldin, C., and Gulyás, B. Performance evaluation of the small-animal nanoScan PET/MRI system. *Journal of Nuclear Medicine*, 54(10):1825–1832, 2013. doi:10.2967/jnumed.112.119065.

NEMA. NEMA standard publication NU 4-2008: Performance measurements of small animal positron emission tomographs, 2008.

Nemallapudi, M. V., Gundacker, S., Lecoq, P., Auffray, E., Ferri, A., Gola, A., and Piemonte, C. Sub-100 ps coincidence time resolution for positron emission tomography with LSO:Ce codoped with Ca. *Physics in Medicine & Biology*, 60(12):4635, 2015. doi:10.1088/0031-9155/60/12/4635.

Nishikido, F., Tachibana, A., Inadama, T. O. N., Yoshida, E., Suga, M., Murayama, H., and Yamaya, T. Development of 1.45-mm resolution four-layer DOI–PET detector

for simultaneous measurement in 3T MRI. *Radiological Physics and Technology*, 8 (1):111–119, 2015. ISSN 1865-0341. doi:10.1007/s12194-014-0298-6.

Nutt, R. The history of positron emission tomography. *Molecular Imaging & Biology*, 4(1):11 – 26, 2002. ISSN 1536-1632. doi:10.1016/S1095-0397(00)00051-0.

Olcott, P., Kim, E., Hong, K., Lee, B. J., Grant, A. M., Chang, C., Glover, G., and Levin, C. S. Prototype positron emission tomography insert with electro-optical signal transmission for simultaneous operation with MRI. *Physics in Medicine & Biology*, 60(9):3459, 2015. doi:10.1088/0031-9155/60/9/3459.

Omidvari, N., Cabello, J., Topping, G., Schneider, F. R., Paul, S., Schwaiger, M., and Ziegler, S. I. PET performance evaluation of MADPET4: a small animal PET insert for a 7 T MRI scanner. *Physics in Medicine & Biology*, 62(22):8671, 2017a. doi:10.1088/1361-6560/aa910d.

Omidvari, N., Sharma, R., Ganka, T., Schneider, F., Paul, S., and Ziegler, S. Characterization of 1.2×1.2 mm^2 silicon photomultipliers with Ce:LYSO , Ce:GAGG, and Pr:LuAG scintillation crystals as detector modules for positron emission tomography. *Journal of Instrumentation*, 12(04):P04012, 2017b. doi:10.1088/1748-0221/12/04/P04012.

Parl, C., Kolb, A., Schmid, A. M., Wehrl, H. F., Disselhorst, J. A., Soubiran, P. D., Stricker Shaver, D., and Pichler, B. J. A novel optically transparent RF shielding for fully integrated PET/MRI systems. *Physics in Medicine & Biology*, 62(18):7357, 2017. doi:10.1088/1361-6560/aa8384.

Peng, B. J., Walton, J. H., Cherry, S. R., and Willig Onwuachi, J. Studies of the interactions of an MRI system with the shielding in a combined PET/MRI scanner. *Physics in Medicine & Biology*, 55(1):265, 2010. doi:10.1088/0031-9155/55/1/016.

Peng, B. J., Wu, Y., Cherry, S. R., and Walton, J. H. New shielding configurations for a simultaneous PET/MRI scanner at 7T. *Journal of Magnetic Resonance*, 239 (Supplement C):50 – 56, 2014. ISSN 1090-7807. doi:10.1016/j.jmr.2013.10.027.

Pepin, C. M., Berard, P., Perrot, A. L., Pepin, C., Houde, D., Lecomte, R., Melcher, C. L., and Dautet, H. Properties of LYSO and recent LSO scintillators for phoswich PET detectors. *IEEE Transactions on Nuclear Science*, 51(3):789–795, June 2004. ISSN 0018-9499. doi:10.1109/TNS.2004.829781.

Pepin, C. M., St-Pierre, C., Forgues, J. C., Kurata, Y., Shimura, N., Usui, T., Takeyama, T., Ishibashi, H., and Lecomte, R. Physical characterization of the LabPET^{TM} LGSO and LYSO scintillators. In *2007 IEEE Nuclear Science Symposium Conference Record*, volume 3, pages 2292–2295, Oct 2007. doi:10.1109/NSSMIC.2007.4436603.

Phelps, M. E. *PET: Molecular Imaging and Its Biological Applications*. Springer New York, NY, 2004. ISBN 978-0-387-22529-6. doi:10.1007/978-0-387-22529-6.

Phelps, M. E., Hoffman, E. J., Mullani, N. A., and Ter-Pogossian, M. M. Application of annihilation coincidence detection to transaxial reconstruction tomography. *Journal of Nuclear Medicine*, 16(3):210–224, 1975. URL `http://jnm.snmjournals.org/content/16/3/210.short`.

Pichler, B. J., Judenhofer, M. S., Catana, C., Walton, J. H., Kneilling, M., Nutt, R. E., Siegel, S. B., Claussen, C. D., and Cherry, S. R. Performance test of an LSO-APD detector in a 7-T MRI scanner for simultaneous PET/MRI. *Journal of Nuclear Medicine*, 47(4):639–647, 2006. URL `http://jnm.snmjournals.org/content/47/4/639.abstract`.

Piemonte, C., Battiston, R., Boscardin, M., Betta, G. F. D., Guerra, A. D., Dinu, N., Pozza, A., and Zorzi, N. Characterization of the first prototypes of silicon photomultiplier fabricated at ITC-irst. *IEEE Transactions on Nuclear Science*, 54 (1):236–244, Feb 2007. ISSN 0018-9499. doi:10.1109/TNS.2006.887115.

Piemonte, C., Ferri, A., Gola, A., Pro, T., Serra, N., Tarolli, A., and Zorzi, N. Characterization of the first FBK high-density cell silicon photomultiplier technology. *IEEE Transactions on Electron Devices*, 60(8):2567–2573, Aug 2013. ISSN 0018-9383. doi:10.1109/TED.2013.2266797.

Pizzichemi, M., Stringhini, G., Niknejad, T., Liu, Z., Lecoq, P., Tavernier, S., Varela, J., Paganoni, M., and Auffray, E. A new method for depth of interaction determination in PET detectors. *Physics in Medicine & Biology*, 61(12):4679, 2016. doi:10.1088/0031-9155/61/12/4679.

Prasad, R., Ratib, O., and Zaidi, H. Performance evaluation of the FLEX triumph X-PET scanner using the national electrical manufacturers association NU-4 standards. *Journal of Nuclear Medicine*, 51(10):1608–1615, 2010. doi:10.2967/jnumed.110.076125.

Qi, J. and Leahy, R. M. Iterative reconstruction techniques in emission computed tomography. *Physics in Medicine & Biology*, 51(15):R541, 2006. doi:10.1088/0031-9155/51/15/R01.

Qi, J., Leahy, R. M., Cherry, S. R., Chatziioannou, A., and Farquhar, T. H. High-resolution 3D bayesian image reconstruction using the microPET small-animal scanner. *Physics in Medicine & Biology*, 43(4):1001, 1998. doi:10.1088/0031-9155/43/4/027.

Qi, J., Yang, Y., Zhou, J., Wu, Y., and Cherry, S. R. Experimental assessment of resolution improvement of a zoom-in PET. *Physics in Medicine & Biology*, 56(17): N165, 2011. doi:10.1088/0031-9155/56/17/N01.

Rafecas, M., B oning, G., Pichler, B. J., Lorenz, E., Schwaiger, M., and Ziegler, S. I. Inter-crystal scatter in a dual layer, high resolution LSO-APD positron emission tomograph. *Physics in Medicine & Biology*, 48(7):821, 2003. doi:10.1088/0031-9155/48/7/302.

Rafecas, M., Mosler, B., Dietz, M., Pogl, M., Stamatakis, A., McElroy, D. P., and Ziegler, S. I. Use of a Monte Carlo-based probability matrix for 3-D iterative reconstruction of MADPET-II data. *IEEE Transactions on Nuclear Science*, 51(5): 2597–2605, Oct 2004. ISSN 0018-9499. doi:10.1109/TNS.2004.834827.

Rahmim, A. and Zaidi, H. PET versus SPECT: strengths, limitations and challenges. *Nuclear Medicine Communications*, 29:193 – 207, 2008. doi:10.1097/MNM.0b013e3282f3a515.

Raylman, R. R., Majewski, S., Lemieux, S. K., Velan, S. S., Kross, B., Popov, V., Smith, M. F., Weisenberger, A. G., Zorn, C., and Marano, G. D. Simultaneous MRI and PET imaging of a rat brain. *Physics in Medicine & Biology*, 51(24):6371, 2006. doi:10.1088/0031-9155/51/24/006.

Renker, D. New developments on photosensors for particle physics. *Nuclear Instruments and Methods in Physics Research Section A: Accelerators, Spectrometers, Detectors and Associated Equipment*, 598(1):207 – 212, 2009. ISSN 0168-9002. doi:10.1016/j.nima.2008.08.023. Instrumentation for Collding Beam Physics.

Renker, D. and Lorenz, E. Advances in solid state photon detectors. *Journal of Instrumentation*, 4(04):P04004, 2009. doi:10.1088/1748-0221/4/04/P04004.

Rolo, M. D., Bugalho, R., Gonçalves, F., Mazza, G., Rivetti, A., Silva, J. C., Silva, R., and Varela, J. TOFPET ASIC for PET applications. *Journal of Instrumentation*, 8(02):C02050, 2013. doi:10.1088/1748-0221/8/02/C02050.

Rowland, D. J. and Cherry, S. R. Small-animal preclinical nuclear medicine instrumentation and methodology. *Seminars in Nuclear Medicine*, 38(3):209 – 222, 2008. ISSN 0001-2998. doi:10.1053/j.semnuclmed.2008.01.004. Developments in Instrumentation.

Sánchez-Crespo, A. and Larsson, S. A. The influence of photon depth of interaction and non-collinear spread of annihilation photons on PET image spatial resolution. *European Journal of Nuclear Medicine and Molecular Imaging*, 33(8):940–947, Aug 2006. ISSN 1619-7089. doi:10.1007/s00259-005-0024-z.

Sato, K., Shidahara, M., Watabe, H., Watanuki, S., Ishikawa, Y., Arakawa, Y., Nai, Y., Furumoto, S., Tashiro, M., Shoji, T., Yanai, K., and Gonda, K. Performance evaluation of the small-animal PET scanner ClairvivoPET using NEMA NU 4-2008 standards. *Physics in Medicine & Biology*, 61(2):696, 2016. doi:10.1088/0031-9155/61/2/696.

Schaart, D. R., van Dam, H. T., Seifert, S., Vinke, R., Dendooven, P., Lohner, H., and Beekman, F. J. A novel, SiPM-array-based, monolithic scintillator detector for PET. *Physics in Medicine & Biology*, 54(11):3501, 2009. doi:10.1088/0031-9155/54/11/015.

Schaart, D. R., Seifert, S., Vinke, R., van Dam, H. T., Dendooven, P., Lohner, H., and Beekman, F. J. $LaBr_3$:Ce and SiPMs for time-of-flight PET: achieving 100 ps coincidence resolving time. *Physics in Medicine & Biology*, 55(7):N179, 2010. doi:10.1088/0031-9155/55/7/N02.

Scheins, J. J., Herzog, H., and Shah, N. J. Fully-3D PET image reconstruction using scanner-independent, adaptive projection data and highly rotation-symmetric voxel assemblies. *IEEE Transactions on Medical Imaging*, 30(3):879–892, March 2011. ISSN 0278-0062. doi:10.1109/TMI.2011.2109732.

Schneider, F. R., Ganka, T. R., Şeker, G., Engelmann, E., Renker, D., Paul, S., Hansch, W., and Ziegler, S. I. Characterization of blue sensitive 3×3 mm^2 SiPMs and their use in PET. *Journal of Instrumentation*, 9(07):P07027, 2014. doi:10.1088/1748-0221/9/07/P07027.

Schug, D., Wehner, J., Dueppenbecker, P. M., Weissler, B., Gebhardt, P., Goldschmidt, B., Salomon, A., Kiessling, F., and Schulz, V. PET performance and MRI compatibility evaluation of a digital, ToF-capable PET/MRI insert equipped with clinical scintillators. *Physics in Medicine & Biology*, 60(18):7045, 2015. doi:10.1088/0031-9155/60/18/7045.

Schug, D., Lerche, C., Weissler, B., Gebhardt, P., Goldschmidt, B., Wehner, J., Dueppenbecker, P. M., Salomon, A., Hallen, P., Kiessling, F., and Schulz, V. Initial PET performance evaluation of a preclinical insert for PET/MRI with digital SiPM technology. *Physics in Medicine & Biology*, 61(7):2851, 2016. doi:10.1088/0031-9155/61/7/2851.

Seeber, D., Jevtic, J., and Menon, A. Floating shield current suppression trap. *Concepts in Magnetic Resonance Part B: Magnetic Resonance Engineering*, 21B(1): 26–31, 2004. ISSN 1552-504X. doi:10.1002/cmr.b.20008.

Seifert, S., van Dam, H. T., Huizenga, J., Vinke, R., Dendooven, P., Lohner, H., and Schaart, D. R. Simulation of silicon photomultiplier signals. *IEEE Transactions on Nuclear Science*, 56(6):3726–3733, Dec 2009. ISSN 0018-9499. doi:10.1109/TNS.2009.2030728.

Seifert, S., van Dam, H. T., Vinke, R., Dendooven, P., Lohner, H., Beekman, F. J., and Schaart, D. R. A comprehensive model to predict the timing resolution of SiPM-based scintillation detectors: Theory and experimental validation. *IEEE Transactions on Nuclear Science*, 59(1):190–204, Feb 2012. ISSN 0018-9499. doi:10.1109/TNS.2011.2179314.

Shao, Y., Cherry, S. R., Farahani, K., Meadors, K., Siegel, S., Silverman, R. W., and Marsden, P. K. Simultaneous PET and MR imaging. *Physics in Medicine & Biology*, 42(10):1965, 1997. doi:10.1088/0031-9155/42/10/010.

Shimazoe, K., Takahashi, H., Fujiwara, T., Furumiya, T., Ooi, J., and Kumazawa, Y. A new dynamic time over threshold method. In *2009 IEEE Nuclear Science Symposium Conference Record (NSS/MIC)*, pages 1916–1918, Oct 2009. doi:10.1109/NSSMIC.2009.5402168.

Somlai-Schweiger, I. and Ziegler, S. I. CHERENCUBE: Concept definition and implementation challenges of a Cherenkov-based detector block for PET. *Medical Physics*, 42(4):1825–1835, 2015. ISSN 2473-4209. doi:10.1118/1.4914857.

Spinks, T. J., Karia, D., Leach, M. O., and Flux, G. Quantitative PET and SPECT performance characteristics of the Albira Trimodal pre-clinical tomograph. *Physics in Medicine & Biology*, 59(3):715, 2014. doi:10.1088/0031-9155/59/3/715.

Stewart, A. G., Seitz, B., O'Neill, K., Wall, L., and Jackson, J. C. Energy resolution of Ce:GAGG and Pr:LuAG scintillators coupled to 3 mm × 3 mm silicon photomultipliers. *IEEE Transactions on Nuclear Science*, 63(5):2496–2501, Oct 2016. ISSN 0018-9499. doi:10.1109/TNS.2016.2574773.

Swiderski, L., Moszynski, M., Nassalski, A., Syntfeld-Kazuch, A., Szczesniak, T., Kamada, K., Tsutsumi, K., Usuki, Y., Yanagida, T., and Yoshikawa, A. Light yield non-proportionality and energy resolution of praseodymium doped LuAG scintil-

lator. *IEEE Transactions on Nuclear Science*, 56(3):934–938, June 2009. ISSN 0018-9499. doi:10.1109/TNS.2009.2015590.

Szanda, I., Mackewn, J., Patay, G., Major, P., Sunassee, K., Mullen, G. E., Nemeth, G., Haemisch, Y., Blower, P. J., and Marsden, P. K. National electrical manufacturers association NU-4 performance evaluation of the PET component of the NanoPET/CT preclinical PET/CT scanner. *Journal of Nuclear Medicine*, 52(11): 1741–1747, 2011. doi:10.2967/jnumed.111.088260.

Sze, S. and Ng, K. K. *Physics of Semiconductor Devices*. John Wiley & Sons, Inc., 2006. ISBN 9780470068328. doi:10.1002/9780470068328.ch13.

Tashima, H. and Yamaya, T. Proposed helmet PET geometries with add-on detectors for high sensitivity brain imaging. *Physics in Medicine & Biology*, 61(19):7205, 2016. doi:10.1088/0031-9155/61/19/7205.

ter Weele, D. N., Schaart, D. R., and Dorenbos, P. Comparative study of co-doped and non co-doped LSO:Ce and LYSO:Ce scintillators for TOF-PET. *IEEE Transactions on Nuclear Science*, 62(3):727–731, June 2015. ISSN 0018-9499. doi:10.1109/TNS.2015.2431295.

Thielemans, K., Tsoumpas, C., Mustafovic, S., Beisel, T., Aguiar, P., Dikaios, N., and Jacobson, M. W. STIR: software for tomographic image reconstruction release 2. *Physics in Medicine & Biology*, 57(4):867, 2012. doi:10.1088/0031-9155/57/4/867.

Thiessen, J. D., Shams, E., Stortz, G., Schellenberg, G., Bishop, D., Khan, M. S., Kozlowski, P., Retiére, F., Sossi, V., Thompson, C. J., and Goertzen, A. L. MR-compatibility of a high-resolution small animal PET insert operating inside a 7 T MRI. *Physics in Medicine & Biology*, 61(22):7934, 2016. doi:10.1088/0031-9155/61/22/7934.

Thompson, C. J., Goertzen, A. L., Berg, E. J., Retiere, F., Kozlowski, P., Ryner, L., Stortz, G., and Sossi, V. Evaluation of high density pixellated crystal blocks with SiPM readout as candidates for PET/MR detectors in a small animal PET insert. *IEEE Transactions on Nuclear Science*, 59(5):1791–1797, Oct 2012. ISSN 0018-9499. doi:10.1109/TNS.2012.2201958.

Torres Espallardo, I. *Image reconstruction and correction methods for MADPET-II based on Monte Carlo techniques*. PhD thesis, Universitat de València - CSIC, 2009. URL `digital.csic.es/bitstream/10261/32422/1/Irene%20Torres-Tesis.pdf`.

Vacheret, A., Barker, G., Dziewiecki, M., Guzowski, P., Haigh, M., Hartfiel, B., Izmaylov, A., Johnston, W., Khabibullin, M., Khotjantsev, A., Kudenko, Y., Kurjata, R., Kutter, T., Lindner, T., Masliah, P., Marzec, J., Mineev, O., Musienko, Y., Oser, S., Retière, F., Salih, R., Shaikhiev, A., Thompson, L., Ward, M., Wilson, R., Yershov, N., Zaremba, K., and Ziembicki, M. Characterization and simulation of the response of multi-pixel photon counters to low light levels. *Nuclear Instruments and Methods in Physics Research Section A: Accelerators, Spectrometers, Detectors and Associated Equipment*, 656(1):69 – 83, 2011. ISSN 0168-9002. doi:10.1016/j.nima.2011.07.022.

van Dam, H. T., Seifert, S., Vinke, R., Dendooven, P., Lohner, H., Beekman, F. J., and Schaart, D. R. A comprehensive model of the response of silicon photomultipliers.

IEEE Transactions on Nuclear Science, 57(4):2254–2266, Aug 2010. ISSN 0018-9499. doi:10.1109/TNS.2010.2053048.

van Dam, H. T., Borghi, G., Seifert, S., and Schaart, D. R. Sub-200 ps crt in monolithic scintillator PET detectors using digital SiPM arrays and maximum likelihood interaction time estimation. *Physics in Medicine & Biology*, 58(10):3243, 2013. doi:10.1088/0031-9155/58/10/3243.

Vandamme, T. Use of rodents as models of human diseases. *Journal of Pharmacy And Bioallied Sciences*, 6(1):2–9, 2014. doi:10.4103/0975-7406.124301.

Vandenberghe, S. and Marsden, P. K. PET-MRI: a review of challenges and solutions in the development of integrated multimodality imaging. *Physics in Medicine & Biology*, 60(4):R115, 2015. doi:10.1088/0031-9155/60/4/R115.

Virdee, K., Cumming, P., Caprioli, D., Jupp, B., Rominger, A., Aigbirhio, F. I., Fryer, T. D., Riss, P. J., and Dalley, J. W. Applications of positron emission tomography in animal models of neurological and neuropsychiatric disorders. *Neuroscience and Biobehavioral Reviews*, 36(4):1188 – 1216, 2012. ISSN 0149-7634. doi:10.1016/j.neubiorev.2012.01.009.

Visser, E. P., Disselhorst, J. A., Brom, M., Laverman, P., Gotthardt, M., Oyen, W. J., and Boerman, O. C. Spatial resolution and sensitivity of the inveon small-animal PET scanner. *Journal of Nuclear Medicine*, 50(1):139–147, 2009. doi:10.2967/jnumed.108.055152.

Wang, L., Zhu, J., Liang, X., Niu, M., Wu, X., Kao, C.-M., Kim, H., and Xie, Q. Performance evaluation of the Trans-PET® BioCaliburn® LH system: a large FOV small-animal PET system. *Physics in Medicine & Biology*, 60(1):137, 2015a. doi:10.1088/0031-9155/60/1/137.

Wang, Q., Wen, J., Ravindranath, B., O'Sullivan, A. W., Catherall, D., Li, K., Wei, S., Komarov, S., and Tai, Y.-C. A compact high resolution flat panel PET detector based on the new 4-side buttable MPPC for biomedical applications. *Nuclear Instruments and Methods in Physics Research Section A: Accelerators, Spectrometers, Detectors and Associated Equipment*, 794:151 – 159, 2015b. ISSN 0168-9002. doi:https://doi.org/10.1016/j.nima.2015.04.071.

Wehner, J., Weissler, B., Dueppenbecker, P. M., Gebhardt, P., Goldschmidt, B., Schug, D., Kiessling, F., and Schulz, V. MR-compatibility assessment of the first preclinical PET-MRI insert equipped with digital silicon photomultipliers. *Physics in Medicine & Biology*, 60(6):2231, 2015. doi:10.1088/0031-9155/60/6/2231.

Wehrl, H. F., Judenhofer, M. S., Thielscher, A., Martirosian, P., Schick, F., and Pichler, B. J. Assessment of MR compatibility of a PET insert developed for simultaneous multiparametric PET/MR imaging on an animal system operating at 7 T. *Magnetic Resonance in Medicine*, 65(1):269–279, 2011. ISSN 1522-2594. doi:10.1002/mrm.22591.

Wehrl, H. F., Hossain, M., Lankes, K., Liu, C.-C., Bezrukov, I., Martirosian, P., Schick, F., Reischl, G., and Pichler, B. J. Simultaneous PET-MRI reveals brain function in activated and resting state on metabolic, hemodynamic and multiple temporal scales. *Nature Medicine*, 19:1184 – 1189, 2013. doi:10.1038/nm.3290.

Weirich, C., Brenner, D., Scheins, J., Besancon, E., Tellmann, L., Herzog, H., and Shah, N. J. Analysis and correction of count rate reduction during simultaneous MR-PET measurements with the BrainPET scanner. *IEEE Transactions on Medical Imaging*, 31(7):1372–1380, July 2012. ISSN 0278-0062. doi:10.1109/TMI.2012.2188903.

Weissler, B., Gebhardt, P., Lerche, C., Wehner, J., Solf, T., Goldschmidt, B., Mackewn, J., Marsden, P., Kiessling, F., Perkuhn, M., Heberling, D., and Schulz, V. MR compatibility aspects of a silicon photomultiplier-based PET/RF insert with integrated digitisation. *Physics in Medicine & Biology*, 59(17):5119, 2014. doi:10.1088/0031-9155/59/17/5119.

Weissler, B., Gebhardt, P., Dueppenbecker, P. M., Wehner, J., Schug, D., Lerche, C. W., Goldschmidt, B., Salomon, A., Verel, I., Heijman, E., Perkuhn, M., Heberling, D., Botnar, R. M., Kiessling, F., and Schulz, V. A digital preclinical PET/MRI insert and initial results. *IEEE Transactions on Medical Imaging*, 34(11):2258–2270, Nov 2015. ISSN 0278-0062. doi:10.1109/TMI.2015.2427993.

Wiener, R. I., Surti, S., and Karp, J. S. DOI determination by rise time discrimination in single-ended readout for TOF PET imaging. *IEEE Transactions on Nuclear Science*, 60(3):1478–1486, June 2013. ISSN 0018-9499. doi:10.1109/TNS.2013.2243166.

Wong, W.-H., Li, H., Baghaei, H., Zhang, Y., Ramirez, R. A., Liu, S., Wang, C., and An, S. Engineering and performance (NEMA and animal) of a lower-cost higher-resolution animal PET/CT scanner using photomultiplier-quadrant-sharing detectors. *Journal of Nuclear Medicine*, 53(11):1786–1793, 2012. doi:10.2967/jnumed.112.103507.

Wu, Y., Catana, C., Farrell, R., Dokhale, P. A., Shah, K. S., Qi, J., and Cherry, S. R. PET performance evaluation of an MR-compatible PET insert. *IEEE Transactions on Nuclear Science*, 56(3):574–580, June 2009. ISSN 0018-9499. doi:10.1109/TNS.2009.2015448.

Yamamoto, S., Hatazawa, J., Imaizumi, M., Shimosegawa, E., Aoki, M., Sugiyama, E., Kawakami, M., Takamatsu, S., Minato, K., Matsumoto, K., and Senda, M. A multi-slice dual layer MR-compatible animal PET system. *IEEE Transactions on Nuclear Science*, 56(5):2706–2713, Oct 2009. ISSN 0018-9499. doi:10.1109/TNS.2009.2030192.

Yamamoto, S., Imaizumi, M., Kanai, Y., Tatsumi, M., Aoki, M., Sugiyama, E., Kawakami, M., Shimosegawa, E., and Hatazawa, J. Design and performance from an integrated PET/MRI system for small animals. *Annals of Nuclear Medicine*, 24 (2):89–98, Feb 2010. ISSN 1864-6433. doi:10.1007/s12149-009-0333-6.

Yamamoto, S., Imaizumi, M., Watabe, T., Watabe, H., Kanai, Y., Shimosegawa, E., and Hatazawa, J. Development of a Si-PM-based high-resolution PET system for small animals. *Physics in Medicine & Biology*, 55(19):5817, 2010b. doi:10.1088/0031-9155/55/19/013.

Yamamoto, S., Watabe, H., Kanai, Y., Aoki, M., Sugiyama, E., Watabe, T., Imaizumi, M., Shimosegawa, E., and Hatazawa, J. Interference between PET and MRI subsystems in a silicon-photomultiplier-based PET/MRI system. *Physics in Medicine & Biology*, 56(13):4147, 2011. doi:10.1088/0031-9155/56/13/026.

Yamamoto, S., Watabe, H., Kanai, Y., Watabe, T., Aoki, M., Sugiyama, E., Kato, K., and Hatazawa, J. Development of a flexible optical fiber based high resolution integrated PET/MRI system. *Medical Physics*, 39(11):6660–6671, 2012. ISSN 2473-4209. doi:10.1118/1.4757911.

Yamamoto, S., Watabe, H., Watabe, T., Ikeda, H., Kanai, Y., Ogata, Y., Kato, K., and Hatazawa, J. Development of ultrahigh resolution Si-PM-based PET system using 0.32 mm pixel scintillators. *Nuclear Instruments and Methods in Physics Research Section A: Accelerators, Spectrometers, Detectors and Associated Equipment*, 836:7 – 12, 2016. ISSN 0168-9002. doi:10.1016/j.nima.2016.08.045.

Yeom, J. Y., Yamamoto, S., Derenzo, S. E., Spanoudaki, V. C., Kamada, K., Endo, T., and Levin, C. S. First performance results of Ce:GAGG scintillation crystals with silicon photomultipliers. *IEEE Transactions on Nuclear Science*, 60(2):988–992, April 2013. ISSN 0018-9499. doi:10.1109/TNS.2012.2233497.

Yoon, H. S., Ko, G. B., Kwon, S. I., Lee, C. M., Ito, M., Chan Song, I., Lee, D. S., Hong, S. J., and Lee, J. S. Initial results of simultaneous PET/MRI experiments with an MRI-compatible silicon photomultiplier PET scanner. *Journal of Nuclear Medicine*, 53(4):608–614, 2012. doi:10.2967/jnumed.111.097501.

Zhang, L., Staelens, S., Van Holen, R., De Beenhouwer, J., Verhaeghe, J., Kawrakow, I., and Vandenberghe, S. Fast and memory-efficient Monte Carlo-based image reconstruction for whole-body PET. *Medical Physics*, 37(7Part1):3667–3676, 2010. ISSN 2473-4209. doi:10.1118/1.3455287.

Appendix A
Supplementary Material

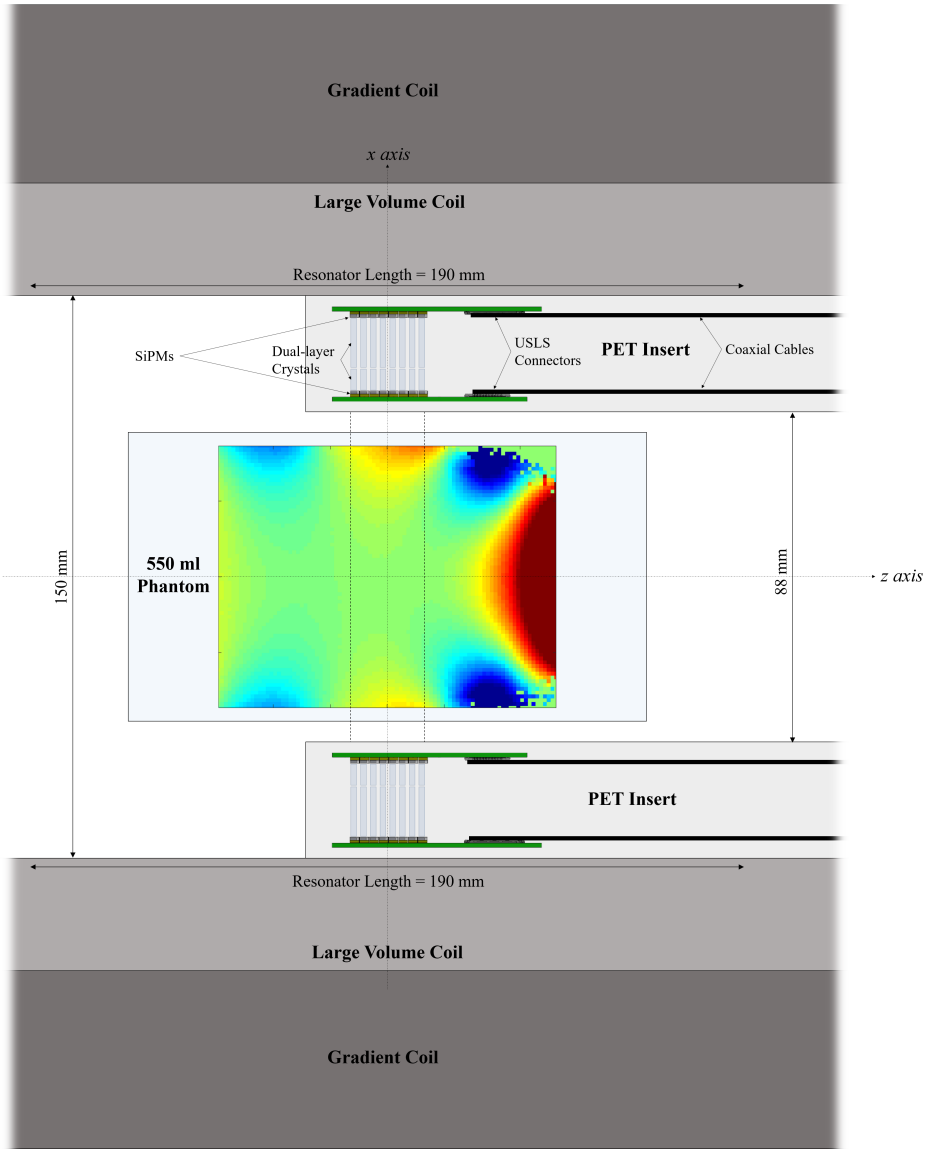

Figure A.1: A schematic of the measurement setup with the large volume coil and the 550 ml phantom, shown with the B0 map obtained after shimming with the PET insert present and acquiring. The FOV of PET is marked with dashed lines.

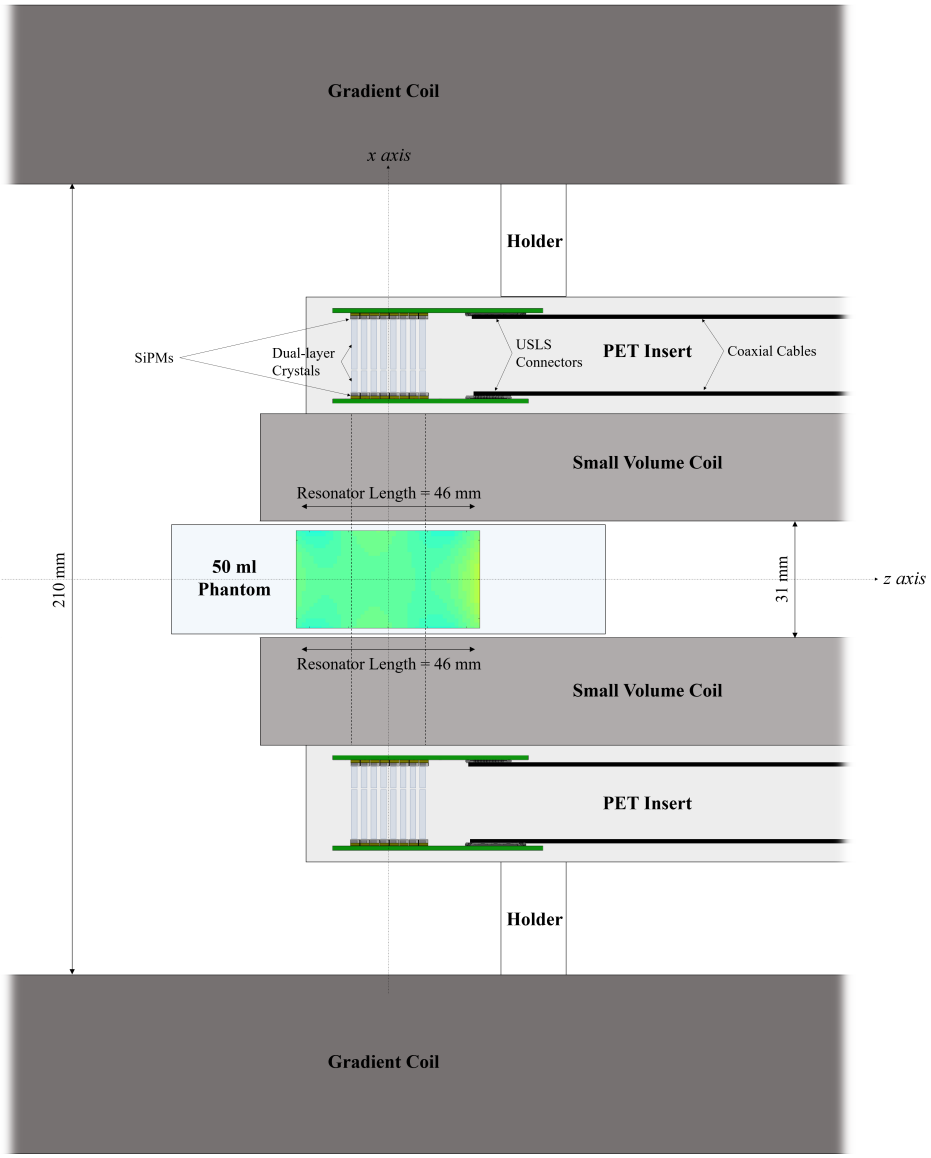

Figure A.2: A schematic of the measurement setup with the small volume coil and the 50 ml phantom, shown with the B0 map obtained after shimming with the PET insert present and acquiring. The FOV of PET is marked with dashed lines.

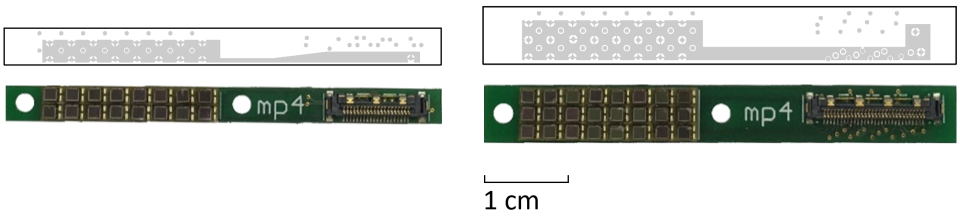

(a) (b)

Figure A.3: The SiPM PCBs for coupling to (a) the inner-layer and (b) the outer-layer crystals. Each inner-layer PCB contains 16 SiPMs and a 20-pin USLS connector, and each outer-layer PCB has 24 SiPMs and a 30-pin USLS connector. The surface defined on one of the PCB layers for the common bias voltage is shown in gray color for each PCB design above the photo of the PCB.

Appendix B
List of publications

B.1 Journal publications

1. **Omidvari, N.**, Topping, G., Cabello, J., Paul, S., Schwaiger, M., and Ziegler, S. I. MR-compatibility Assessment of MADPET4: a study of interferences between an SiPM-based PET insert and a 7 T MRI system. *Physics in Medicine & Biology*, 63(9):095002, 2018. doi:10.1088/1361-6560/aab9d1

2. **Omidvari, N.**, Cabello, J., Topping, G., Schneider, F. R., Paul, S., Schwaiger, M., and Ziegler, S. I. PET performance evaluation of MADPET4: a small animal PET insert for a 7 T MRI scanner. *Physics in Medicine & Biology*, 62(22):8671, 2017. doi:10.1088/1361-6560/aa910d.

3. **Omidvari, N.**, Sharma, R., Ganka, T., Schneider, F., Paul, S., and Ziegler, S. Characterization of 1.2×1.2 mm^2 silicon photomultipliers with Ce:LYSO , Ce:GAGG, and Pr:LuAG scintillation crystals as detector modules for positron emission tomography. *Journal of Instrumentation*, 12(04):P04012, 2017. doi:10.1088/1748-0221/12/04/P04012.

4. **Omidvari, N.** and Schulz, V. Characterization of sensitivity encoded silicon photomultiplier (SeSP) with 1-dimensional and 2-dimensional encoding for high resolution PET/MR. *IEEE Transactions on Nuclear Science*, 62(3):679, 2015. doi:10.1109/TNS.2015.2422374.

5. Schulz, V., Berker, Y., Berneking, A., **Omidvari, N.**, Kiessling, F., Gola, A., and Piemonte, C. Sensitivity encoded silicon photomultiplier – a new sensor for high-resolution PET-MRI. *Physics in Medicine & Biology*, 58(14):4733, 2013. doi:10.1109/TNS.2015.2422374.

B.2 Conference proceedings

1. Schulz, V., Berker, Y., Berneking, A., **Omidvari, N.**, Kiessling, F., Gola, A., and Piemonte, C. A 2D sensitivity encoded silicon photomultiplier (SeSP) for simultaneous high resolution PET/MR scanners. In *2012 IEEE Nuclear Science Symposium and Medical Imaging Conference Record (NSS/MIC)*, pages 3743-3745, Oct 2012. doi:10.1109/NSSMIC.2012.6551859

B.3 Conference presentations

1. **Omidvari, N.** 2018 MR-Compatibility Assessment of MADPET4: A Small Animal PET Insert for a 7 T MRI Scanner, oral presentation at *7th PET-MRI and SPECT-MRI (PSMR) Conference*, Elba, Italy, 21–23 May.
2. **Omidvari, N.** 2017 Performance evaluation and MR-compatibility of MADPET4: a small animal PET insert for 7 T MRI, oral presentation at *2017 IEEE Nuclear Science Symposium and Medical Imaging Conference (NSS/MIC)*, Atlanta, GA, USA, 21–28 October.
3. **Omidvari, N.** 2017 Performance evaluation of MADPET4: a high resolution preclinical PET insert for 7 T MRI, oral presentation at *Jahrestagung der Biomedizinischen Technik und Dreiländertagung der Medizinischen Physik (DGMP & DGBMT) 2017*, Dresden, Germany, 10–13 September.
4. **Omidvari, N.** 2017 First performance evaluation of MADPET4: a small animal PET insert for 7 T MRI, oral presentation at *6th PET-MRI and SPECT-MRI (PSMR) Conference*, Lisbon, Portugal, 29–31 May.
5. **Omidvari, N.** 2017 First PET performance evaluation of MADPET4: a preclinical MR compatible PET insert based on SiPMs, oral presentation at *NuklearMedizin 2017*, Dresden, Germany, 26–29 April.
6. **Omidvari, N.** 2017 First PET performance evaluation of MADPET4: a preclinical MR compatible PET insert based on SiPMs, oral presentation at *12th European Molecular Imaging Meeting (EMIM)*, Cologne, Germany, 5–7 April.
7. **Omidvari, N.** 2016 Including inter crystal scattering data in PET image reconstruction: a Monte Carlo study for MADPET4, poster presentation at *2016 IEEE Nuclear Science Symposium and Medical Imaging Conference (NSS/MIC)*, Strasbourg, France, 29 October–6 November.
8. **Omidvari, N.** 2016 A Monte Carlo study of scattering in the system components and impacts of it on image quality of MADPET4 – a dual layer small animal PET insert, oral presentation at *47th DGMP and 19th German Section of ISMRM*, Würzburg, Germany, 7–10 September.
9. **Omidvari, N.** 2015 A Monte Carlo study of inter-crystal scattering and coincidence sorting for MADPET4, oral presentation at *2015 IEEE Nuclear Science Symposium and Medical Imaging Conference (NSS/MIC)*, San Diego, CA, USA, 31 October–7 November.
10. **Omidvari, N.** 2015 A Monte Carlo study of inter-crystal scattering and random coincidences for MADPET4, poster presentation at *4th PET-MRI and SPECT-MRI (PSMR) Conference*, Elba, Italy, 17–21 May.
11. **Omidvari, N.** 2015 Experimental characterization of different crystals and SiPMs as detector modules for MADPET4, poster presentation at *10th European Molecular Imaging Meeting (EMIM)*, Tübingen, Germany, 18–20 March.
12. **Omidvari, N.** 2014 Characterization of sensitivity encoded silicon photomultiplier (SeSP) with 1-dimensional and 2-dimensional encoding for high resolution

PET/MR, poster presentation at *3rd PET-MRI and SPECT-MRI (PSMR) Conference*, Kos, Greece, 19–21 May.